ABSTRACT

Title of dissertation: AEROELASTIC STABILITY ANALYSIS OF A WING WITH A VARIABLE CANT ANGLE WINGLET

Jose Mauricio Mondragon Gomez
Doctor of Philosophy, 2020

Dissertation directed by: Professor James E. Hubbard Jr.
Department of Aerospace Engineering

Currently, multiple air vehicles employ wing shape change to enhance their performance and achieve mission adaptability in different environments inside the Earth's atmosphere. This concept has been around since the dawn of aviation. In 1903, the Wright brothers implemented wing warping to control their aircraft during flight. Subsequently, a variety of techniques and devices have used to achieve wing shape change and make the vehicles more versatile. For example, they include variable wing sweep, folding wing tips, and variable camber. However, aeroleasticity has played in important role in these developments. Thus, this work focuses on the aeroelastic analysis and understanding of the fundamental physics of the flutter mechanism of a wing equipped with a variable cant angle winglet. Two methods are applied to model the wingletted wing system. The Rayleigh Ritz method is the first technique used to model the system. This method involves the implementation of a shape function to represent the entire structure. The second method used in the analysis is the Finite Element Analysis. In this formulation, the wing structure is

divided into elements and elemental functions are used for local interpolation. Strip theory is used to model the spanwise aerodynamic loading. In addition, steady, quasi-steady, and unsteady aerodynamics model are used, each with different levels of complexity. Both the structural and aerodynamic models were coupled to generate four dynamic aeroelastic equations that represent the continuous system. Those equations were used to model the system and perform a dynamic aeroelastic analysis. The results indicate that having a vehicle equipped with a variable cant angle winglet can be favorable. It can increase flutter speed and expand its flight envelope. Moreover, when the winglet length is greater than 50% the length of the wing section and the cant angle greater than 50^{o}, the second torsional mode of vibration becomes unstable. Whereas, the first mode remains marginally stable. Thus, the second mode has become the critical mode that leads to structural failure. In this case, that phenomenon is referred as mode switching.

AEROELASTIC STABILITY ANALYSIS OF A WING WITH A VARIABLE CANT ANGLE WINGLET

by

Jose Mauricio Mondragon Gomez

Dissertation submitted to the Faculty of the Graduate School of the
University of Maryland, College Park in partial fulfillment
of the requirements for the degree of
Doctor of Philosophy
2020

Advisory Committee:
Professor James E. Hubbard Jr., Chair/Advisor
Professor Amr Baz
Professor Alison Flatau
Professor Allen Winkelmann
Professor James Baeder

Dedication

This work is dedicated to my dear family and specially to my wife – Guiting (Angela) – and dog – Luna Nova – who have showed unconditional support throughout this journey.

Acknowledgments

I owe a great deal of gratitude to all the people who have been part of this endeavor. They have seen different aspects of my work and helped me in multiple ways. This is something that I will cherish forever.

First and foremost I would like to thank my advisor, Professor James E. Hubbard Jr. for giving me the honor to work under his mentorship and allow me to challenge myself inside and outside the laboratory over the past years. I appreciate the fact that he has always made himself available for help and advice even when he transferred to another institution. It has been a pleasure to work with and learn from such a great individual.

I want to also thank my faculty committee members. Their support and guidance was extremely important in order to complete this work. First, I want to thank Dr. Flatau who has guided me since I was an undergraduate student. I am thankful to Dr. Winkelmann for teaching me fundamental principles in experimentation. In addition, I am grateful to Dr. Baz who has given me endless support. Finally, I want to thank Dr. Baeder for all his advice and sharing his knowledge.

Additionally, I want to express my gratitude to my mother and father, Ana Mondragon and Jose Mondragon. They have been pivotal support since the beginning of this journey. Moreover, I want to thank my wife - Guiting Ng-Mondragon -for her patience and unconditional support. They believed in me when I did not believe in myself and gave me courage to look ahead and keep moving forward.

I would also like to thank Gen III from the Morpheus laboratory who have

enriched my graduate life with their help, advise, and valuable friendship. I am grateful to have had the chance to work with this incredible group. Special thanks to Michael Cunningham, Rose Weinstein, Zohaib Hasnain, Joaquim Dias, and Nick Rymer for their support, and teaching me something new every day.

Also, I would like to acknowledge the help and encouragement provided by some staff members from the National Institute of Aerospace (NIA). Rita Aguillard's help on setting up the long distance learning classroom at NIA is highly appreciated. Also, I want to thank Keith Jones and Suzanne Zaremski for teaching me how to use laboratory equipment and their cooperation to ensure student safety.

Lastly, thank you everyone who was involved in this journey!

Table of Contents

List of Tables

List of Figures

Chapter 1: Introduction

1.1 Overview of the Field of Aeroelasticity

From the dawn of aviation, aeroelasticity has influenced the course of aircraft design. This is due to the fact that aircraft structures are not perfectly rigid. Instead, they are relatively flexible because thinner structures and lighter materials that are more commonly employed. Professor Collar indicated that the nature of the aeroelastic phenomenon can be depicted in the form of a *Triangle of Forces* where the aerodynamic, elastic, and inertial forces mutually interact (See Figure 1.1) [1]. From this, three major disciplines can be identified, namely aerodynamics, elasticity, and dynamics [2]. In addition, the combination of these disciplines leads to multiple engineering fields. For instance, the combination of elastic and inertial forces constitute the field of structural dynamics. Flight dynamics is the result of the interaction of inertial and aerodynamic forces. When the elastic and aerodynamic forces combine, they lead to the field of static aeroelasticity. Finally, the reciprocal relationship among all three forces leads to the study of dynamic aeroelasticity [3].

Static aeroelasticity becomes relevant when the aerodynamic forces and moments cause the aircraft structure to deform. Such deformation increases the magnitude of the aerodynamic forces and moments and further deforms the structure,

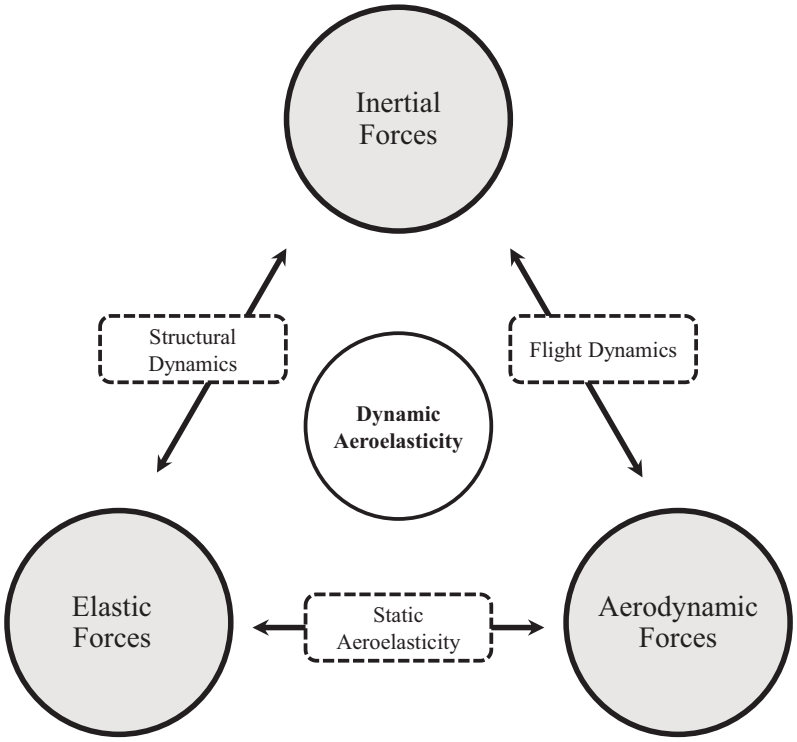

Fig. 1.1: Representation of the force triangle describing the interaction between elastic, inertial, and aerodynamic forces that constitute dynamic aeroelasticity.

consequently leading to a phenomenon known as *divergence*. In other words, this is the situation when the restoring elastic forces of the structure can no longer counteract the aerodynamic forces and moments [4, 5].

Flutter is the result of dynamic aeroelasticity. Flutter is a self-excited oscillation that occurs during flight where energy is absorbed by the structure from the airstream [6]. At any given flight speed, the inertial and elastic forces interact with the aerodynamic loading and produce a coupled structural wing motion that results in two modes of vibration, pitch (φ) and heave (h). Typically, the oscillations are

well damped at lower speeds. However, there is a critical speed above which the structure will exhibit large amplitude oscillations that may lead to structural failure. That critical speed is referred to as the wing *flutter speed* [4]. Since the determination of this critical speed is crucial to defining the flight envelope, it is important to understand the fundamental physics of the flutter mechanism of a wing.

1.1.1 Aeroelastic Analysis of Planar and Wingletted Wings

1.1.1.1 Planar Wings

Before analyzing wingletted wings, it is necessary to study and understand planar wings. The first flutter incidents occurred due to the introduction of thinner, lighter wing structures, control surfaces, and the pursuit of higher flight speeds. In 1916, F.W. Lanchester, a British engineer, took on the task investigating the reason behind the violent tail and fuselage oscillations of the Handley Page O/400, depicted in Figure 1.2 [7, 8]. From his investigation, he made an important statement. He concluded that resonance was not the cause for the large amplitude vibration of the structure; instead, it was *self-excited*. From that point in time, flutter became a problem of great importance within the aeroelasticity field. This is a problem that must be eliminated or prevented from occurring on aircraft during flight [6].

Formal procedures to test dynamic aeroelastic instability did not exist during that period of time. Different techniques were designed to study this phenomenon and understand what triggered it. In some cases, the vehicle was flown to its maximum flight speed to observe its structural response and determine if the vehicle was

Fig. 1.2: Handley Page O400 - British biplane bomber used during WWI.

safe [8]. Another technique required the pilot to fly the aircraft to a given flight condition and then provide an input to excite the airframe and take note of the response. In addition, the aircraft designers would carry out ground test to obtain information about the frequency response of the airframe. However, most of the test techniques were deemed unsafe or inadequate in a significant number of cases because they caused severe structural damage or complete loss of the aircraft [9].

Even though the techniques were rudimentary, they provided a great amount of important information on the understanding of dynamic aeroelasticity. Using the results from the experiments and analyses, R. A. Frazer and W. J. Duncan drafted a detailed document describing their results and prevention procedures for the flutter instability problem [10]. Their annotations laid out the foundation for the imple-

mentation of flutter prediction analysis. Another topic of great importance was the application of potential flow and the Kutta condition with unsteady aerodynamics. The application of these analytical models improved the analysis and facilitated the understanding of this dynamic phenomenon [11]. It allowed engineers to represent the aerodynamic forces on an oscillating wing structure in multiple degrees of freedom. In 1945, Martin Goland carried out a study where he analyzed a planar wing configuration [12]. He discussed the procedure to approximate the speed at which the system became unstable. In addition, the results from his analysis agree with the exact solution of the problem. His analysis has been widely used as a benchmark for verification and validation in various studies, including complex configurations, such as the one presented in this work.

1.1.1.2 Non-planar Wings

Over the past few years, aircraft design has evolved at a fast pace. Current aircraft designs allow the vehicles to change their wing configuration or shape during flight, in order to enhance their aerodynamic performance. A vehicle can change its wing shape to adapt to multiple mission profiles and meet higher requirements. This is not a new concept. It has been around since the beginning of aviation. The Wright Brothers used wing-warping as a way to provide lateral control to their vehicle during flight in 1903 [13]. Subsequently, a variety of devices such as flaps, ailerons, and slats were created. They have been used to change an aircraft's wing geometry and enhance its aerodynamic characteristics.

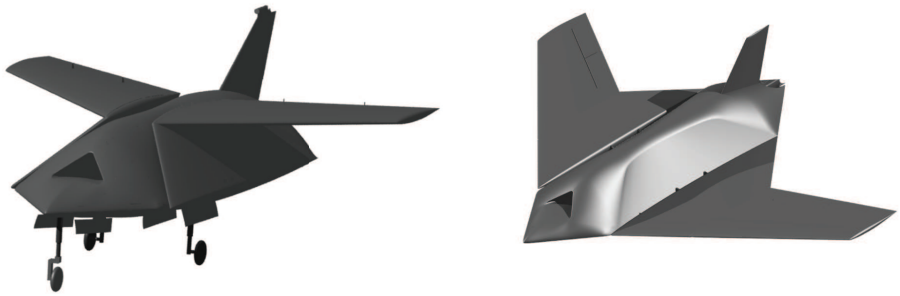

Fig. 1.3: Lockheed Martin Z-wing Morphing Flight Demonstrator (MFD). Concept exhibits its folded and extended wing configurations.

More recently, different approaches have been taken to achieve radical wing shape changes [14, 15]. Some wing shape change methods include wing folding, variable sweep, and changing camber. One of these examples is the Morphing Flight Demonstrator (MFD) presented by Lockheed Martin in 2007. The vehicle was designed to showcase the company's new morphing technology. The MFD concept illustrated in Figure 1.3 is a result from the Morphing Adaptive Structures (MAS) program created by the Defense Advanced Research Project Agency (DARPA) [16]. The MFD can morph its wings into a "Z" shape configuration by folding its inner wing section against the fuselage and keeping the outer wing section horizontal. This allows the aircraft to drastically reduce or increase its effective lifting surface and achieve a higher or lower flight speed, respectively.

Moreover, other aircraft designs have featured folding wing tips or winglets. It has been shown that the implementation of this mechanism can augment directional and lateral control of a vehicle during flight. In 2018, Aera-I showcased this capability with its Prototype-Technology Evaluation Research Aircraft (PTERA),

presented in Figure 1.4 [17]. PTERA served as a platform to test the implementation of a shape-memory-alloy based actuation system for the winglet or wing tip folding mechanism. Their folding wing tip concept is similar to the one implemented on the XB-70 Valkyre presented in Figure 1.5. The vehicle was developed in the late 1950s, and it featured folding wing tips to improve directional stability during cruise at high lift to drag (L/D) ratio [18].

Fig. 1.4: AREA I's Prototype-Technology Evaluation Research Aircraft (PTERA). Vehicle exhibits the application of articulated outer wing sections to provide lateral stability and control.

Due to the multiple variables involved, the design of a winglet requires substantial analysis in order to validate its performance. Most studies have concentrated their efforts on a Multi-Disciplinary Optimization (MDO) analysis for a given wing geometry with the objective of enhancing a few or multiple performance aspects of the vehicle. For instance, the structure and shape of the wing has been optimized to minimize bending stress at the wing root, weight of the structure, and total

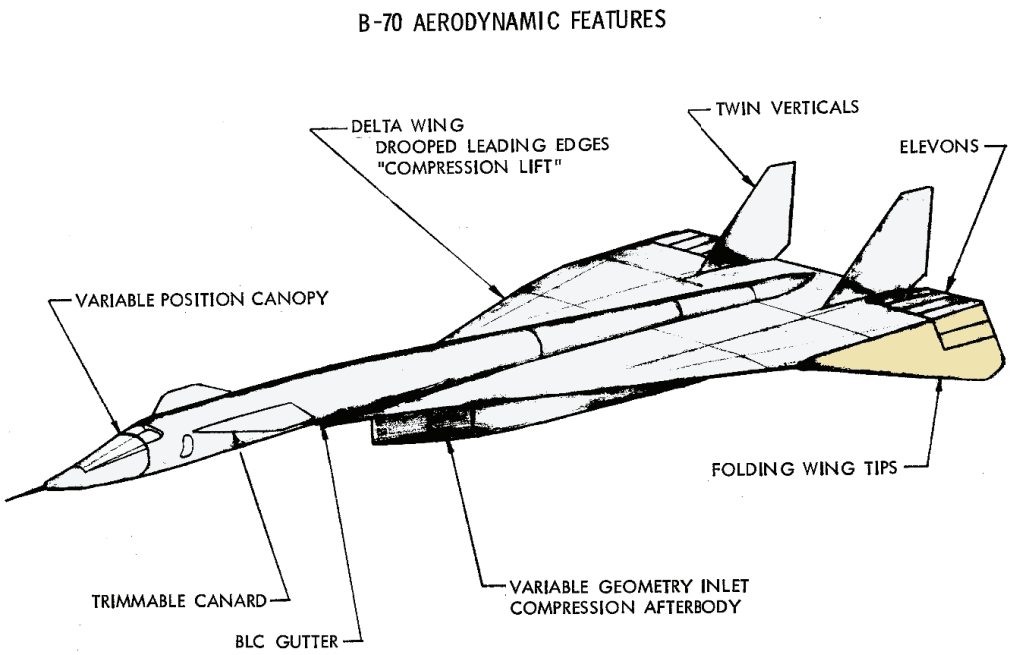

Fig. 1.5: XB-70 Valkyre - Strategic bomber featuring folding wing tips to improve directional stability during cruise.

drag [19,20]. Khosravi and Zingg performed an aerostructural optimization analysis using a high order model. Their analysis predicted a total drag reduction of 2% for a wing with a winglet down configuration [21]. This is a result of the projected wing span from the deformed structure. Then, Keisuk compared the benefits of having a planar wing tip extension versus having a non-planar section or winglet added to the main wing structure. His research indicated that a winglet can reduce parasitic drag and bending stress at the wing root [22]. Also, Elham and Van Tooren performed an analysis that focused on the aerodynamic shape and structural mass of a wing equipped with a winglet to enhance fuel efficiency [23]. Their analysis resulted in a fuel weight saving of approximately 3.8%. This indicates that a wingletted wing configuration can reshape the spanwise lift distribution and reduce the amount of

fuel needed during flight.

Other than improving fuel efficiency, folding winglets or outboard wing sections have also been studied as an alternative way to provide aircraft lateral control. A numerical study performed at The University of Texas at Arlington showed that it is possible to provide lateral control through asymmetric wing articulation, which results from the lift imbalance between both wings (See Figure 1.6) [24]. Previous work has suggested that it requires a very complex control law to maintain stability during flight due to the changes in inertial and aerodynamic characteristics. For example, Bowman, Reich, and Sanders generated a computer flight simulation using a simplified model of the MFD (See Figure 1.7) [25]. They noticed that when the vehicle started to fold its wings symmetrically, it was not able to maintain a steady altitude; instead, the aircraft started to dive. This type of response prompted the deployment of multiple control surfaces in order to retain a somewhat constant altitude. From their analysis, they observed that folding wings alone cannot provide enough control authority [26-28]. Even though this idea is interesting, it raised multiple questions about the structural stability of the vehicle and the ability to implement faster actuation systems.

To this point, it is clear that flutter was not a concern in previous works. They focused on different objectives, such as fuel efficiency, control authority, and adaptability. However, the impact of winglets on the aeroelastic characteristics of airplanes has also been investigated. For instance, the DC-10 commercial aircraft, presented in Figure 1.8, was the subject of a variety of studies involving winglets [29, 30]. One of their analyses focused on the impact of winglets on the vehicle's

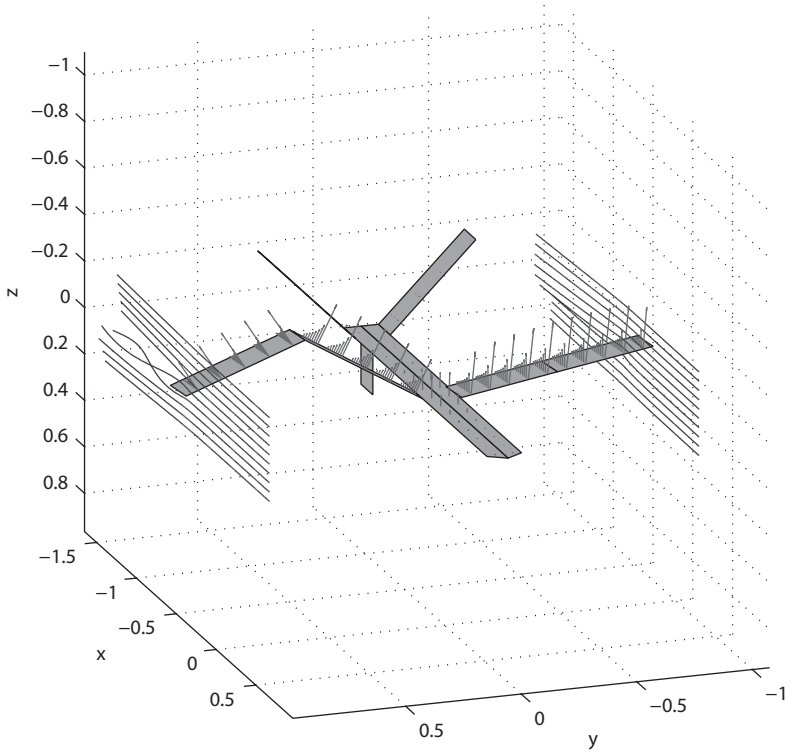

Fig. 1.6: Asymmetric wing representation employed in Obradovic and Subbarao's analysis.

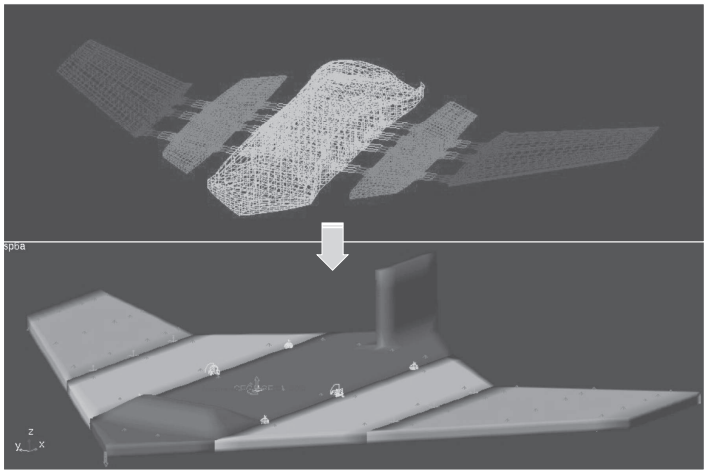

Fig. 1.7: Flat plate model representation of the Morphing Flight Demonstrator used for flight simulation.

high-speed stability characteristics. Their research showed a reduction of the flutter speed boundary, and it was attributed to coupling of higher order modes between the winglet and the wing. A mass balance was added to alleviate the problem and ensure structural stability during flight.

Fig. 1.8: Experimental McDonnell Douglas DC-10 commercial aircraft equipped with winglets performing a flight test.

Other research related to the application of winglets was the KC-135 Winglet Program Review. The Boeing KC-135 tanker served as a test platform to investigate the potential benefits of having winglets on a wing (See Figure 1.9). The results showed that adding winglets improved the fuel efficiency from 4.4% to 7.1% for a 0.78 Mach number and different payloads [31]. Furthermore, a flutter analysis was performed due to the additional mass and modifications made to the structure to accommodate winglets. A series of flight tests and wind tunnel experiments were performed to investigate the effects of angle of incidence and the angle between wing

and winglet, cant angle (γ), on the critical flutter speed [32]. The aircraft exhibited a reduction of flutter speed for some winglet configurations. This was due to the structural changes and variations in mass of the wing.

Fig. 1.9: Boeing KC-135 Stratotanker experimental aircraft modified with winglets.

Few authors have dedicated their work to understand this complex issue in wingletted wings or structures alike. Their work shed some light into this problem and provided important information. This type of wing geometry contains multiple changing variables, such as cant angle, length of the wing sections, mass distribution, and elastic properties [33, 34]. Wang and Dowell presented a generalized structural dynamics model that was based on Beam Theory to represent a folding wing [35]. The results from their work indicate that the natural frequencies are sensitive to folding angles since the inertial properties changed. The bending and

torsion frequencies become closer to each other as the cant angle increases from 0° to 90°. Afterwards, they added the aerodynamic component to their previous study to produce an aeroelastic model. In that work, they observed significant changes in the vibration modes of the system when a cant angle was applied [36].

Ruhlin, Rauch, and Waters investigated wingletted wing configurations as well. They indicated that the implementation of a winglet can decrease the critical flutter speed of the wing structure between 7% to 19% [37]. The results were mainly attributed to the aerodynamic characteristics of the winglet. On another study, Ruhlin analyzed ten different models with varying winglet type, cant angle, engine nacelle, and inertial properties. He discovered that the flutter speed can either increase or decrease based on the wing configuration [38]. Also, Tang and Dowell investigated the aeroelastic behavior of a folding structure [39]. They indicated that an increase in torsional stiffness of inboard section can improve the aeroelastic stability of the structure. Opposite results are obtained if the outboard section is stiffer.

1.2 Motivation, Goal, Objectives, and Scope of the Dissertation

As presented in the previous sections, most of the studies referenced lacked understanding of the fundamental physics of dynamic aeroelasticity for wingletted wing geometries. Additionally, instead of applying basic assumptions to simplify the problem, some used higher or full order models that did not have a closed-form solu-

tion and could only be solved through high computing programs. These programs or solvers were computationally expensive. They required substantial computational times to obtain flutter predictions for a few flight conditions. The majority of those works were performed on a case by case basis, which did not provide generalized trends to the various parameters that affect dynamic aeroelastic instability. The motivation for this work stems from the need to provide additional knowledge about the aeroelastic characteristics of a wingletted wing with a variable cant angle winglet. Thus, the present research focuses on understanding the fundamental physics of the flutter mechanism for a wingletted wing configuration. For the purposes of this aeroelastic study, a generalized wingletted wing geometry will be used to represent the structure of the system. The distributed aerodynamic loads are represented through the application of two-dimensional incompressible flow theory.

The goal of this work is the following: *Analyze and understand the fundamental physics of the flutter mechanism for a wingletted wing configuration through the application of beam and two-dimensional flow theory.*

In order to accomplish this goal, it is important to achieve the following objectives:

1. Develop numerical and analytical models that are capable of capturing the structural, inertial, and aerodynamic characteristics of a wing with a variable cant angle winglet.

2. Investigate and understand the fundamental physics and flutter mechanism of the given dynamic aeroelastic system.

3. Establish critical parameters to maximize flutter speed of articulated winglets through a generalized wingletted wing configuration.

1.3 Dissertation Outline

In order to provide a comprehensive description of this research, it is structured as follows:

Chapter 1 provides background information about aeroelasticity. It introduces some of the terms and definitions that will be used in this work. Moreover, it gives a brief narrative of the history of aeroelasticity, and how it impacted the development of aviation. The results from previous works on planar and non-planar wing configurations are discussed. This motivated the need to analyze wingletted wings. Also, Chapter 1 defines the scope of the work and lists the goals and objectives.

Chapter 2 outlines the technical approach implemented in this research. It breaks down the work carried out in this dissertation into sections. It also contains the definition of a wingletted wing, which is necessary in order to understand the problem and the analysis.

Chapter 3 details the derivation of the structural model and its respective assumptions. It describes the application of kinematics to obtain the position and velocity with respect to an inertial frame for both wing sections. Then, these formulations are used to derive the equations of motion via Hamilton's Principle. In addition, it presents and describes three different aerodynamic flow models that will be used in the analysis. These models are implemented to generate the distributed

aerodynamic forces and moments acting on the system. Then, the structural and each of the aerodynamic models are coupled to produce an aeroleastic model that represents the wingletted wing system.

Chapter 4 describes the discretization and flutter speed approximation methods used in this dissertation. For instance, the Rayleigh-Ritz Method and Finite Element Method were used to spatially discretize the continuous system. These discretized models are used for flutter speed determination, which becomes an iterative process for all wing configurations. The results from both methods are compared to determine their validity against other well-known aeroelastic model results.

Chapter 5 presents the results from the flutter analysis on various wing configurations. Wingletted wing results are compared to the ones obtained from planar wing configurations. The comparison is used to determine the flutter dependencies and understand the physics of the phenomenon. Moreover, the results from various configurations are presented in this chapter.

Finally, Chapter 6 gives the concluding remarks of this research. In addition, it summarizes the research, lists contributions to the field, and makes recommendations for future research.

Chapter 2: Aeroleastic Research Methodology

2.1 Overview

In this chapter, a detailed description of the research methodology applied in this work will be introduced. In order to accomplish the goals and objectives defined in Section 1.2, the current approach aims to investigate the aeroelastic characteristics of a wingletted wing using a build up approach. Hence, the methodology outlined in Figure 2.1 is followed.

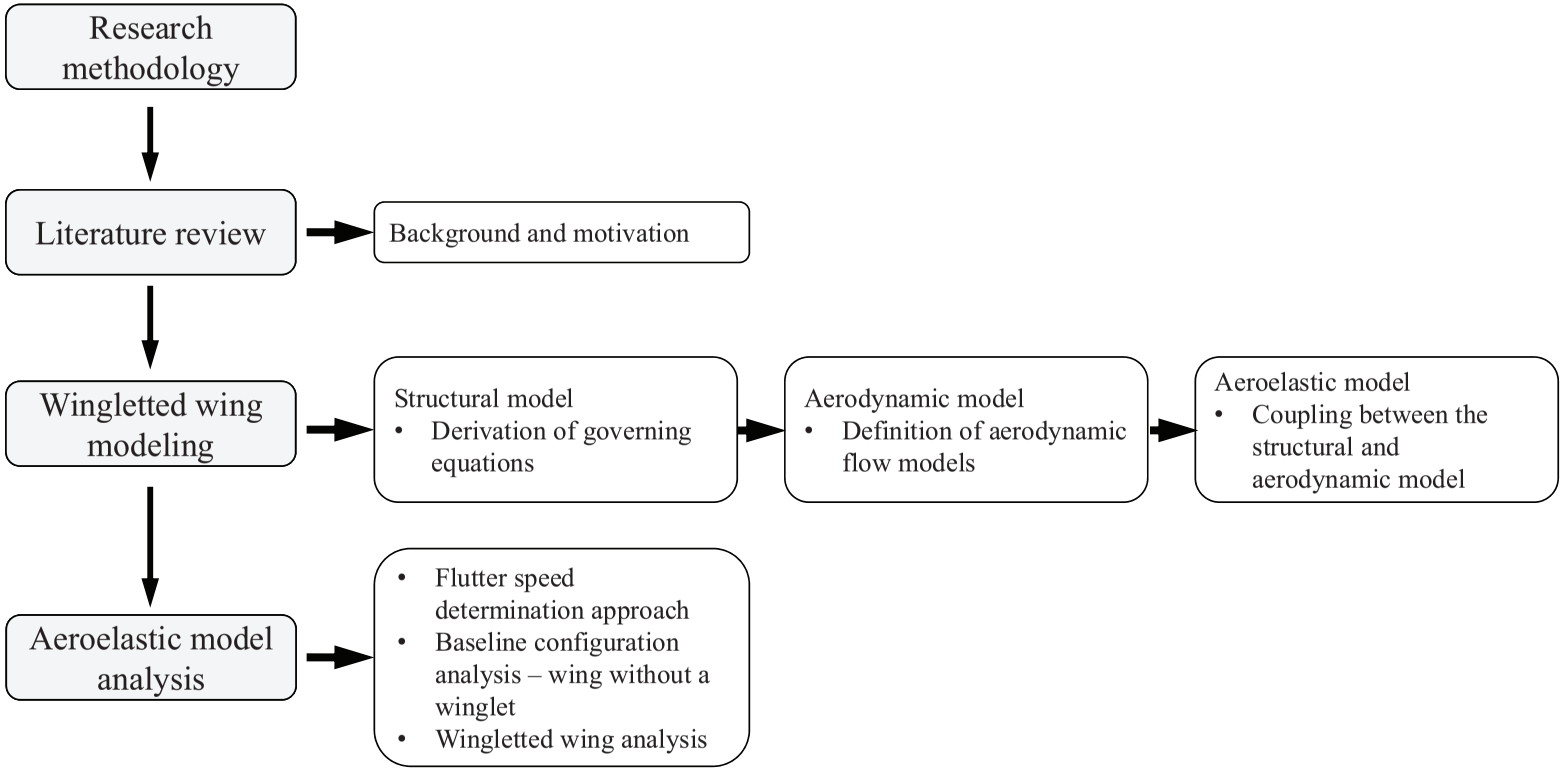

Fig. 2.1: Methodology flow chart outlining the process followed in this research.

2.2 Wingletted Wing Modeling

Prior to deriving a generalized aeroelastic model, it is important to state a definition for a wingletted wing configuration. A wingletted wing with a variable cant angle winglet can be identified as a structure that is composed primarily of two panels or segments as depicted in Figure 2.2. The first wing panel is referred to as the inner or inboard wing segment. The inboard segment is fixed to the fuselage at its root. Then, there is the outboard or outer wing panel, which is also known as the winglet. This panel is rigidly attached to the inboard wing panel at the joint, and it can vary its cant angle γ with respect to the inboard wing panel. Therefore, the entire structure can be considered as a fixed-free beam.

2.2.1 Structural Model Definition and Derivation

At the begining of any type of analysis, it is crucial to state some assumptions that enforce the fundamental physics in order to properly represent the system that is being studied. In addition, these assumptions will facilitate the modeling and understanding of the problem.

First, each section is considered to be made of an isotropic material. Both wing sections are considered to be unswept, have a uniform mass distribution, and dynamically loaded in bending and torsion along their span. In addition, one shall assume that there is a reference axis that runs along the span of each section, which is called the elastic axis x_{ea}. As it is sketched in Figure 2.3, the axis along which the sectional center of mass is located is called inertial axis, and runs parallel to the

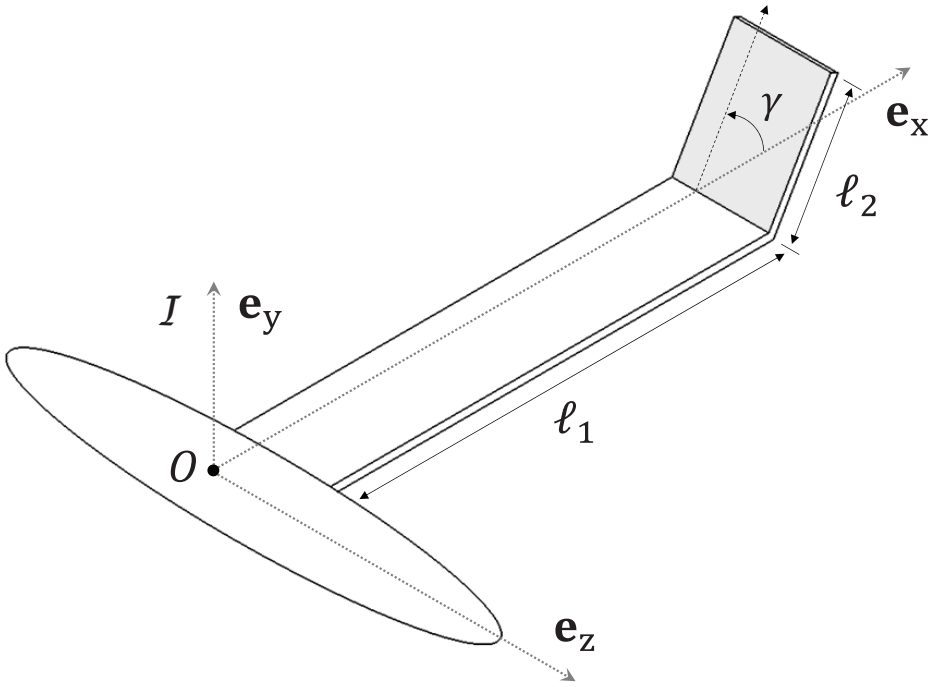

Fig. 2.2: Wingletted wing representation. It shows both wing sections rigidly attached at the wing tip. The wing section root is clamped to the fuselage.

elastic axis x_{ea}, and they are separated by a distance d_{cm}. The existence of the elastic axis allows the system to become inertially coupled, and eliminates elastic coupling. In addition, the wing and winglet roots are sufficiently stiff to be considered as if they were clamped perpendicularly to the elastic axis [5, 40].

Euler-Bernoulli Beam Theory is applied in the modeling of the system. This implies that planar sections remain planar and perpendicular to the elastic axis; and that all deformations are considered to be small [2, 41]. This indicates that each wing section has a rigid cross-section, which means that there is no elastic deformation along the chord of the wing sections. These assumptions allow each section to undergo out-of-plane deformation, which is a linear combination of the

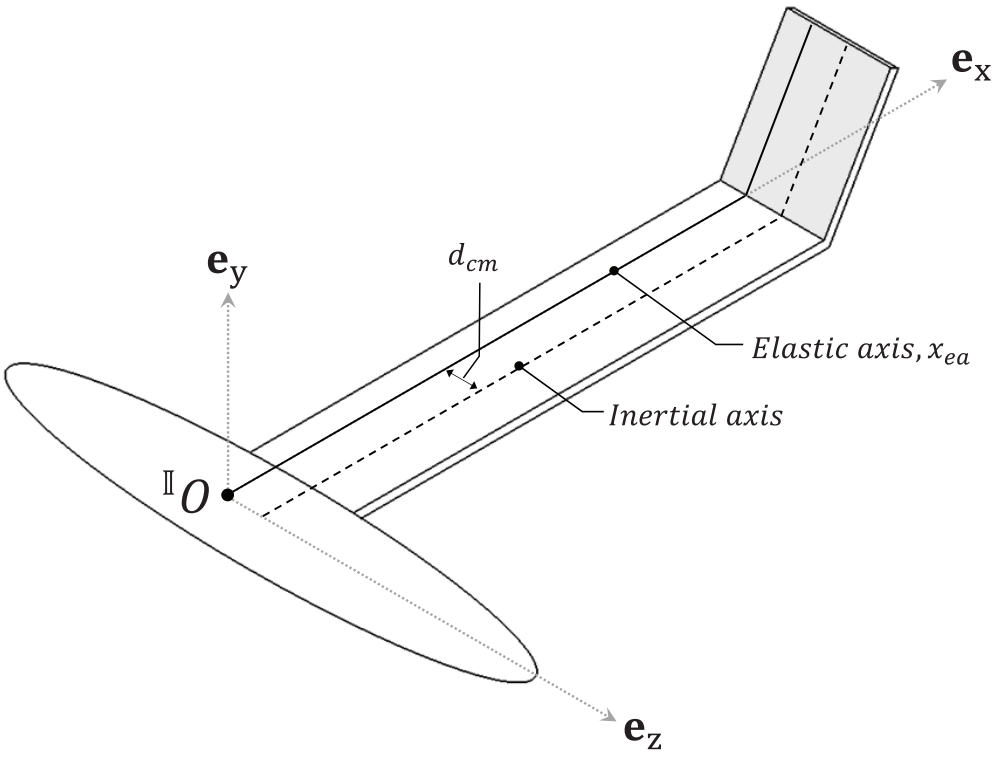

Fig. 2.3: Wingletted wing axes location. It denotes the location of the elastic and inertial axes along the span of the structure.

heave and pitch motion.

The inboard wing section out-of-plane deformation is represented by two mode displacements, bending (h) and torsion (φ), about the elastic axis x_{ea}. Consequently, the displacement of the winglet is the result of two types of motion. The out-of-plane bending and torsion displacement about x_{ea} of the winglet itself constitute the first type of motion. The second contribution to the winglet displacement is the in-plane motion, whose translation and rotation is a result from the out-of-plane motion at the end of the inboard wing section. This confirms the need to include the rotational inertia terms for the winglet deformation in order to properly represent the system

dynamics [42]. These remarks will become more clear once the kinematic equations describing the position and velocity of any point $P(x)$ along the wing and winglet are derived in Section 3.2.2.1.

2.2.2 Aerodynamic Model Formulation and Implementation

With the definitions and assumptions for the structural model of a wingletted wing already established, one can now introduce an aerodynamic model to represent the aerodynamic forces and moments. In this work, the aerodynamic flow models are formulated through the implementation of *Strip Theory*. The lifting surface is divided into a series of strips that span the length of both wing sections, thus allowing estimation of the aerodynamic loads at each section by employing two-dimensional airfoil theory [3, 43]. The local lift coefficient is given as:

$$c_l = 2\pi\alpha,$$

where 2π and α denote the theoretical lift slope per radian and local angle of attack, respectively. This formulation indicates that the lift coefficient is directly proportional to the angle of attack [44].

With the implementation of Strip Theory, one can introduce three aerodynamic models, namely Steady, Quasi-steady, and Unsteady flow. Each model has increasing levels of complexity to describe the flow around the wing. For instance, the steady flow model is the simplest of all. It states that the lift generated is directly proportional to the local geometric angle of attack α. Although, if one wants

to model quasi-steady flow, it is important to consider the effective angle of attack α_{eff}, which is presented as

$$\alpha_{eff} = \alpha - \frac{\dot{h}}{U}.$$

This equation represents a linear combination of the local angle of attack α and the heave or bending rate $\dot{h}$ of the wing with respect to the incoming flow U [5, 45]. The unsteady flow model is the most complex of all three models. Unlike the quasi-steady flow, it considers the unsteady effects of the wake around an oscillating wing cross-section. In order to do so, this model incorporates Theodorsen's function $C(k)$, which depends on the reduced frequency k [11, 46]. The reduced frequency is given by

$$k = \frac{\omega b}{U},$$

where ω, b, and U refer to the frequency of oscillation, half the chord length of the wing, and forward speed, respectively. As a result, the magnitude of the aerodynamic forces and moments are reduced compared to the Steady and Quasi-steady Flow models . Consequently, the flutter speed approximation results are affected, and they are different compared to the other two models. More details about all three aerodynamic models will be discussed in Section 3.3.

2.2.3 Dynamic Aeroelastic Modeling Formulation for a Winglet-ted wing

The dynamic aeroelastic model for a wingletted wing is the result of the combination of the aerodynamic and structural models. The aeroleastic model represents a continuous system and the interaction of the three forces depicted in the force triangle in Figure 1.1. Equation 2.1 is the mathematical representation of this interaction

$$[M]\begin{Bmatrix}\ddot{h}\\ \ddot{\varphi}\end{Bmatrix}+[C]\begin{Bmatrix}\dot{h}\\ \dot{\varphi}\end{Bmatrix}+[K_{eq}]\begin{Bmatrix}h\\ \varphi\end{Bmatrix}=\begin{Bmatrix}0\\ 0\end{Bmatrix}. \tag{2.1}$$

Where $[M]$, $[C]$, and $[K_{eq}]$ denote the mass, damping and equivalent damping matrices of the dynamic system. In addition, the governing equation contains terms that describe the vertical and angular displacement.

2.3 Aeroelastic Model Analysis

In this analysis, two methods were used to discretize the continuous system. They are: the Rayleigh-Ritz Method (RRM) and Finite Element Method (FEM). These approaches are similar to some extend, since both provide an approximate solution to the problem by converting a set of partial differential equations to a set of algebraic ordinary differential equations. This is achieved by assuming a solution

that is separable in space and time

$$\xi(x,t) = \sum_{n=1}^{n} \xi_i(x)\phi_i(t). \tag{2.2}$$

In this formulation, ξ_i and ϕ_i denote the shape functions and the generalized coordinates, respectively. The shape or basis functions ξ_i represent the displacement of the structure. However, the shape functions applied to both methods are different. For instance, FEM considers the structure to be divided into a series of n discrete segments. Thus, the deformation of the system is given by piecewise interpolated functions for each element [41]. The results from this method improve when the number of elements increases. On the other hand, the RRM considers shape functions that describe the modal deformation for the entire structure. To properly determine the shape functions, it requires prior knowledge about the deformation of the structure under similar conditions. If it is not known, multiple shape functions can be used to better approximate the solution and improve accuracy.

The application of both discretization methods lead to the canonical form of the equation of a linear dynamic system:

$$[M]\{\ddot{\phi}\} + [C_{aero}]\{\dot{\phi}\} + [K_{eq}]\{\phi\} = 0. \tag{2.3}$$

In Equation 2.3, it is observed that the aeroelastic equation of motion contains terms regarding the mass of the system, aerodynamic damping, and equivalent stiffness, given by M, C_{aero}, and K_{eq}, respectively. Note that this canonical representation

resembles a discretized damped system that shows the reciprocal interaction between the inertial, elastic, and aerodynamic forces in pitch and heave.

State-space model representation is an alternative way to express the governing equations,

$$\{\dot{\phi}\} = [A]\{\phi\}. \tag{2.4}$$

In this formulation, $[A]$ represents the state matrix, which contains the system variables such as mass, stiffness, and damping; and $\{\phi\}$ is referred to as the state vector [47]. Flutter speed can be predicted through the solution of the eigenvalue problem since the flutter condition is characterized by the dynamic or non-trivial solution of the problem. The following equations are used:

$$(A - \lambda I)\{p\} = 0, \tag{2.5}$$

where λ is the eigenvalues, I denotes the identity matrix, and p represents the corresponding eigenvectors. For a given flight condition (altitude and speed), one can obtain the eigenvalues associated to the systems and its respective frequencies. From an iterative process, it is possible to the determine the speed at which the system becomes unstable, i.e. at least ones of the poles becomes unstable.

Once the flutter speed approximation process has been established, it is possible to analyze any given wing configuration within the limitation and constrains described in Sections 2.2.1 and 2.2.2. The results from this procedure are verified using a planar wing configuration. The wing used in this study has the geomet-

ric, inertial, and structural properties from the Goland Wing [12]. In Chapter 5, a winglet section with the same inertial and elastic properties will be added to analyze the aeroelastic characteristics of the entire system.

2.4 Wingletted Wing Flutter Prediction Results

The results from planar and non-planar wing configurations are compared and verified against previous work. The verification process makes sure that the analysis captures the physics of the problems and provides a good understanding of the findings. Other wing properties or parameters are varied to observe the aeroelastic response of the system. Multiple features are noted from the analysis. For instance, for winglet sections larger than 40% of the length of the wing, the rotational inertia increases. Hence, the torsion frequency is greatly reduced. When the quasi-steady and unsteady flow models are implemented, one will be able to observe the effects of aerodynamic damping on the flutter approximation results.

Chapter 3: Wingletted Wing Modeling

3.1 Overview

The purpose of this chapter is to present a step by step process explaining the derivation of the governing equations of the wingletted wing system. The derivation process is done through the application of multi-body dynamics and Hamilton's Principle. Upon completion of the structural model derivation, three different aerodynamic flow models will be introduced. They will represent the associated aerodynamic forces and moments acting on the structure, namely the steady, quasi-steady, and unsteady flow models. These models allow to incorporate the effects of aerodynamic damping and aerodynamic loading build up during the wing oscillations. Then, the three aerodynamic flow models are integrated into the governing equations to produce a set of aeroelastic equations of motion for a distributed parameter system. From that, one will be able to study the reciprocal interaction between the inertial, elastic forces of the structure, and the associated aerodynamic loading.

3.2 Derivation of the Structural Model

3.2.1 Model Assumptions and Definitions

As it was mentioned in section 2.2.1, prior to formulating any type of model, it is important to state some simplifying assumptions to facilitate the derivation process of the governing equations. Using Figure 2.2 as a reference, the structure is assumed to be under forced vibration from the aerodynamic loads, and each section of the structure is considered to be a thin plate with flexural rigidity [48]. Additionally, the wing and winglet are defined as straight, uniform, and continuous panel sections.

Euler-Bernoulli Beam Theory is applied since each wing section is presented as a slender body. The application of this theory implies that planar cross-sections remain planar, and small angle deformations are considered. Each wing section, perpendicular to the x-axis or longitudinal axis, has a rigid cross-section, which means that there is no elastic deformation along the chord. The application of Beam Theory calls for the definition of the neutral or elastic axis, i.e. the axis that does not undergo longitudinal stress or strain. Hence, it allows twist about the x-axis. Based on these assumptions, it is appropriate to consider that each wing panel undergoes out-of-plane deformation, which considers a linear model of the uncoupled modes in bending and torsion of a beam. They are also referred to as heave and pitch modes [12, 41, 49]. In addition, the wingletted wing structure is considered to be clamped at its root.

In general, for any aeroelastic system, one needs to define multiple reference points in the chordwise direction of the wing and winglet sections as it is depicted in Figure 3.1. First, There is the aerodynamic center defined by point A. The associated aerodynamic lift L and moment M_a are expressed about this point. It is located at a distance d_{ac} from the shear locus center or elastic axis, which is denoted by point B. In addition, the origin of the inertial and non-inertial reference frames used in the derivation process will be located along this axis. Point C marks the location of the center of mass or inertial axis of system. Points B and C are separated by a distance d_{cm}. The off-set distance will become apparent in the equations of motion by showing *inertial coupling* between the heave and pitch modes. Moreover, the twist or pitch angle φ is measured from the undeflected wing centerline to the zero lift line. [2]. The points presented in Figure 3.1 can be extended to the length of each section. Figure 3.2 shows the undeformed configuration along with the three axes running in parallel throughout the span of each section.

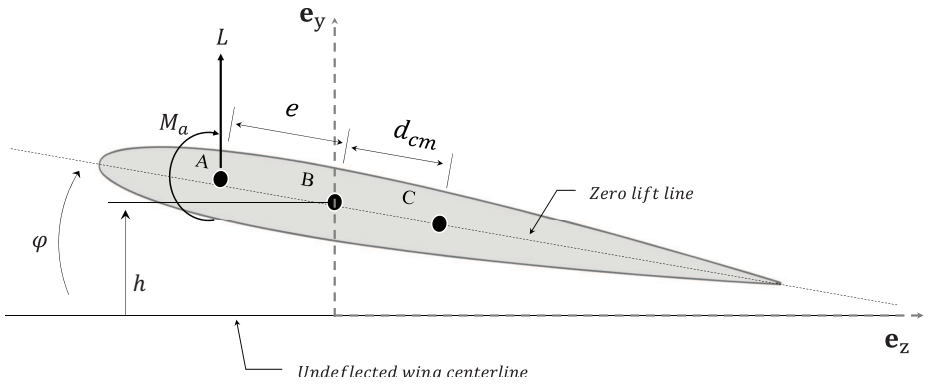

Fig. 3.1: Wing cross-section geometry showing the location of the aerodynamic center (A), elastic axis (B), and center of mass (C). It also shows the aerodynamic lift and moment about the elastic axis.

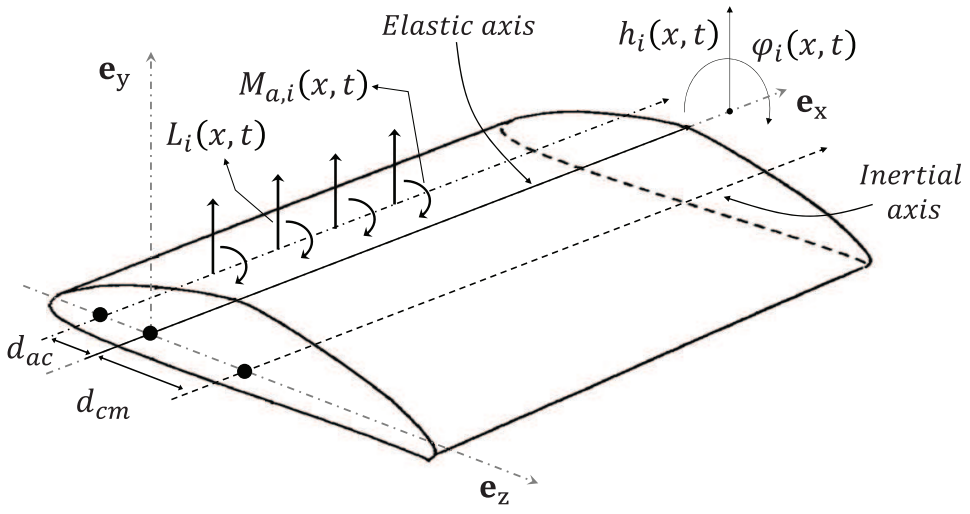

Fig. 3.2: Representation of the axes location along the span of a wing section. Also shown are pitch $\varphi_i(x,t)$, heave $h_i(x,t)$, lift $L_i(x,t)$, and aerodynamic moment $M_{a,i}(x,t)$ as distributed parameters.

3.2.2 Definition and Application of Hamilton's Principle

The governing equations for any given system can be formulated through application of Newton's Second Law. However, this can be a complicated task especially for a wingletted wing system for which approximate solutions are sought. For instance, it requires a free-body diagram for a differential element with its respective sign convention for forces and moments. Instead, it is easier to write approximations in energy terms [3, 50, 51]. Additionally, for systems with multiple degrees of freedom such as the one analyzed in this research, it is adequate to formulate the equations of motion through the application of Hamilton's Principle. This is a well-known analytical method in classical mechanics, and it is described in detail in

various textbooks. According to this principle, the motion of a system is presented as:

$$\int_{t_1}^{t_2} (\delta T - \delta V + \overline{\delta W}_{nc}) dt = 0, \delta\phi_k = 0, k = 1, 2, ..., n; t = t_1, t_2. \tag{3.1}$$

In this formulation, the terms T and V represent the total kinetic and potential energy in the system, respectively. The virtual work due to the exogenous forces or aerodynamic loading is described by $\overline{\delta W}_{nc}$. Also, $\delta[\cdot]$ denotes the virtual change of the quantity in terms of the generalized coordinates $\phi_k (k = 1, 2, ..., n)$. The time interval at which the configuration of the system is known is indicated by t_1, t_2. In addition to the governing equations, Hamilton's Principle yields a set of expressions that satisfy the natural and geometric boundary conditions associated to this system.

Being that this is a multi-body system, it is adequate to define multiple reference frames with their respective coordinate systems. In this study, a reference frame will be referred to as a collection of perpendicular axes that describe the position or displacements of a point relative to the origin in a body [52]. Figure 3.3 illustrates the main coordinate systems and frames being used in this analysis. Note that there are two coordinate systems that correspond to two different frames, one for each wing section or panel. They are referred to as the *inertial* and *non-inertial frames*. Moreover, a similar nomenclature to the one used by Kasdin and Paley is implemented in this work [53]. One can write $\mathcal{I} = (O, \mathbf{e}_\mathrm{x}, \mathbf{e}_\mathrm{y}, \mathbf{e}_\mathrm{z})$ to represent the inertial frame $\mathcal{I}$ with its origin O located at the root of the inboard wing section. Similarly, the non-inertial frame is presented as $\mathcal{W} = (O', \mathbf{w}_\mathrm{x}, \mathbf{w}_\mathrm{y}, \mathbf{w}_\mathrm{z})$. It has the

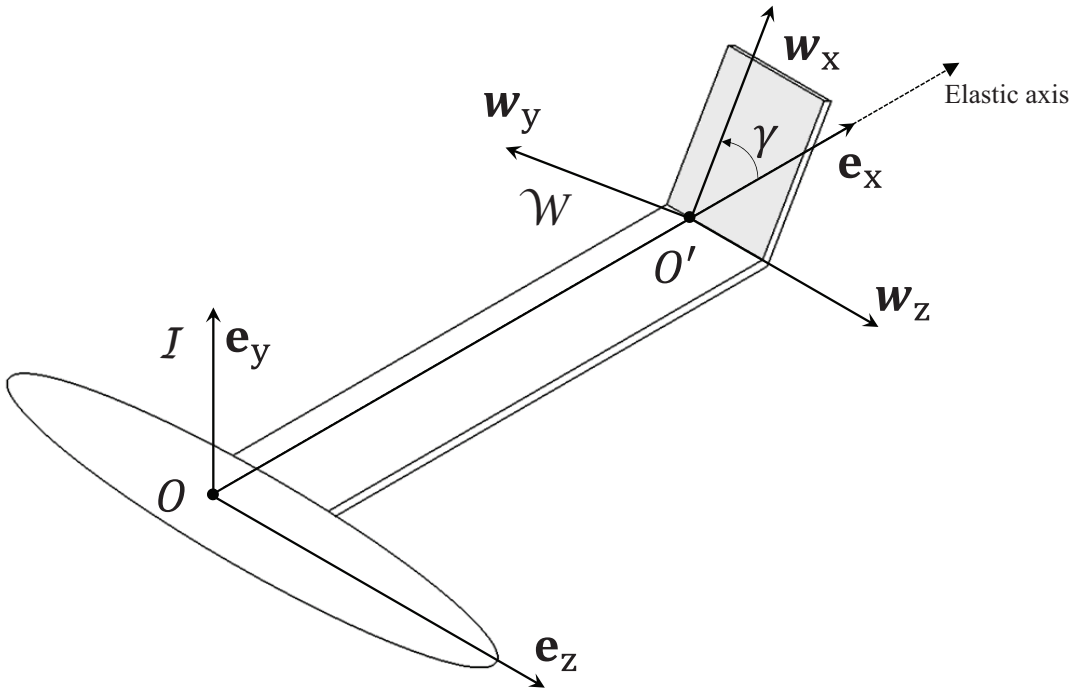

Fig. 3.3: Undeformed wingletted wing coordinate system representation. Presents both the inertial and non-inertial frames used to represent the system.

origin O' placed at the root of the winglet, which is aligned with the elastic axis. This is the point where the wing and winglet sections are rigidly attached. The orientation of the $\mathcal{W}$ frame changes with the winglet cant angle γ. However, this frame is allowed to translate vertically due to the wing tip deformation and keeps the undeformed body orientation. Additional intermediate frames will be used to express the orientation and displacement of the wing and winglet in terms of the $\mathcal{I}$ frame. Again, this analysis only takes into consideration the *out-of-plane* deformation as a result of the pitch and heave motion.

3.2.2.1 Derivation of Wingletted Wing Kinematics

To begin the derivation process, let us start with the inboard or wing section panel and temporarily ignore the winglet. It will later be incorporated when it is time to compute the kinetic energy of the system. An expression for the kinetic energy can be obtained by looking at the position of any point P_i in space with respect to the inertial frame along the span of the wing section. Now, let us look at Figure 3.4(a) and determine the position of P_1 when the wing section undergoes out-of-plane deformation. Before taking any further steps in the derivation process, it is necessary to introduce a non-inertial frame $\mathcal{B}$ to describe the position of the point P_1 in its local coordinate system, $\mathcal{B} = (O'', \mathbf{b}_1, \mathbf{b}_2, \mathbf{b}_3)$. The sketch in Figure 3.4(b) describes the relationship between the inertial and intermediate frames, where the $\mathcal{B}$ frame is centered along the elastic axis, and can translate vertically due to the out-of-plane motion of the wing.

One can use Equation 3.2 as a general form to express the location of point P_1 along the wingletted wing structure denoted by P_1 relative to the origin O in the inertial frame $\mathcal{I}$, where $\mathbf{e}_\mathrm{x}, \mathbf{e}_\mathrm{y}$, and $\mathbf{e}_\mathrm{z}$ refer to the unit vectors. Additionally, $a_i, i = 1, 2, 3$, indicates the magnitude of the components in the inertial frame. Before writing an expression for the location of point P_1, it is appropriate to determine $\mathbf{r}_{P_1/O''}$ and $\mathbf{r}_{O''/O}$ from Equation 3.3. $\mathbf{r}_{O''/O}$ is the position of O'' with respect to O,

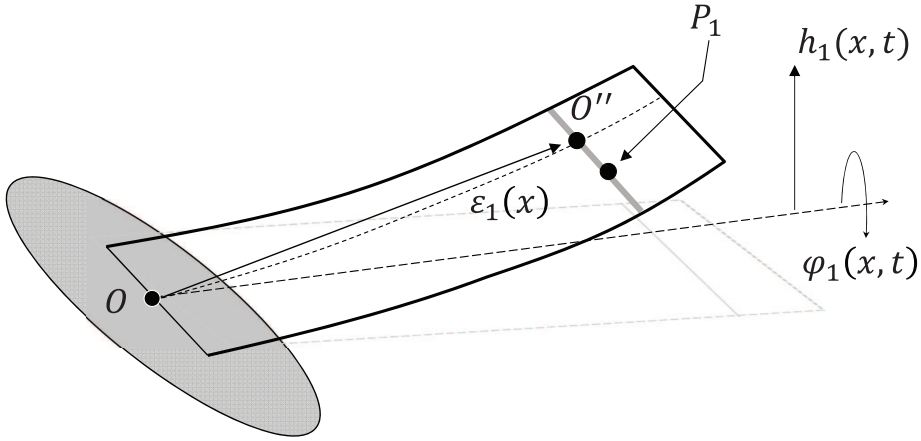

(a) Coordinates

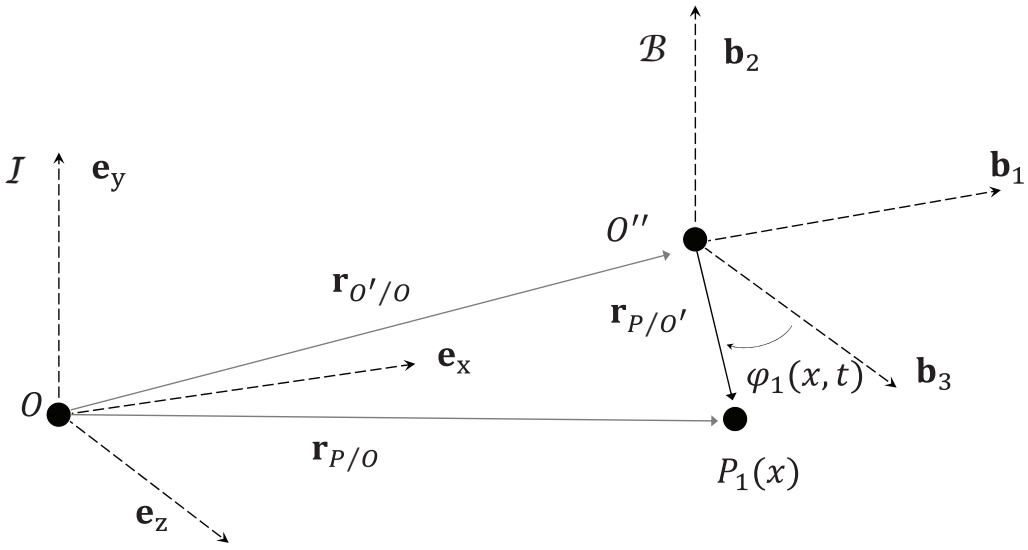

(b) Reference frames

Fig. 3.4: Location of point P_1 along the span of the wing section and representation of vector components in the inertial frame $\mathcal{I}$ and non-inertial frame $\mathcal{B}$.

and $\mathbf{r}_{P_1/O''}$ defines the location of point P_1 with respect to O''.

$$\mathbf{r}_{P_1/O} = a_1\mathbf{e}_{\mathrm{x}} + a_2\mathbf{e}_{\mathrm{y}} + a_3\mathbf{e}_{\mathrm{z}}. \tag{3.2}$$

$$\mathbf{r}_{P_1/O} = \mathbf{r}_{P_1/O''} + \mathbf{r}_{O''/O}. \tag{3.3}$$

Consider a 2D representation of the wing section – zy plane – as it is sketched in Figure 3.5. The figure shows the generalized coordinates h and φ, which represent the heave and pitch modes of the system. The center of mass is positioned along the chord of the wing, and it is coincident with point P_1. Its chordwise position is described by $\mathbf{r}_{P_1/O''}$ in Equation 3.4. It is important to bear in mind that all this is done in relation to the $\mathcal{B}$ frame, which is allowed to move vertically due to the heave motion. Now, let us write the position of O'' with respect to O in the inertial frame. Thus, the vector positions $\mathbf{r}_{P_1/O''}$ and $\mathbf{r}_{O''/O}$ are given by

$$\mathbf{r}_{P_1/O''} = 0\mathbf{b}_1 - d_{cm}\sin\big(\varphi_1(x)\big)\mathbf{b}_2 + d_{cm}\cos\big(\varphi_1(x)\big)\mathbf{b}_3, \tag{3.4}$$

$$\mathbf{r}_{O''/O} = \varepsilon_1(x)\mathbf{e}_{\mathrm{x}} + h_1(x)\mathbf{e}_{\mathrm{y}} + 0\mathbf{e}_{\mathrm{z}}, \tag{3.5}$$

where d_{cm} is defined as the distance between the elastic axis and the center of mass. The spanwise coordinate along the wing segment is denoted by $\varepsilon_1(x)$, and $h_1(x)$, and $\varphi_1(x)$ are the spanwise heave, pitch displacement, respectively. Since frame $\mathcal{B}$ is aligned with the neutral axis and the vertical displacement is measured from the equilibrium point, Equation 3.4 can be written in the inertial frame coordinate

system to obtain the following expression

$$\mathbf{r}_{P_1/O''} = 0\mathbf{e}_{\mathrm{x}} - d_{cm}\sin\big(\varphi_1(x)\big)\mathbf{e}_{\mathrm{y}} + d_{cm}\cos\big(\varphi_1(x)\big)\mathbf{e}_{\mathrm{z}}. \tag{3.6}$$

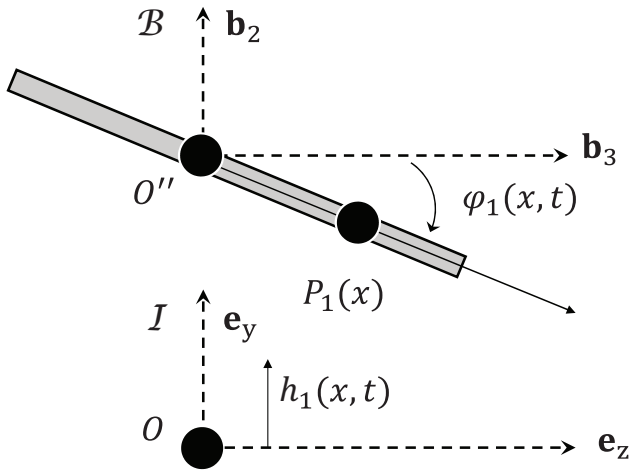

Fig. 3.5: Representation of the vertical position of point $P_1(x)$ in reference to the $\mathcal{I}$ and $\mathcal{B}$ frames.

Equations 3.5 and 3.6 can be substituted into Equation 3.3 to lead to a final expression for $\mathbf{r}_{P_1/O}$ denoted by

$$\mathbf{r}_{P_1/O} = \varepsilon_1(x)\mathbf{e}_{\mathrm{x}} + \Big[h_1(x) - d_{cm}\sin(\varphi_1(x))\Big]\mathbf{e}_{\mathrm{y}} + d_{cm}\cos(\varphi_1(x))\mathbf{e}_{\mathrm{z}}. \tag{3.7}$$

By applying a small angle approximation, it yields to the following equation that characterizes the spanwise vector position of point P_1 on the wing segment

$$\mathbf{r}_{P_1/O} = \varepsilon_1(x)\mathbf{e}_{\mathrm{x}} + \Big[h_1(x) - d_{cm}\varphi_1(x)\Big]\mathbf{e}_{\mathrm{y}} + d_{cm}\mathbf{e}_{\mathrm{z}}. \tag{3.8}$$

The position of a point P_2 located on the outboard wing segment can be obtained through a process similar to the one applied to the wing segment. However, this procedure requires additional work to obtain such expression. Hence, some considerations need to be taken into account to model the system adequately. The position of point P_2 comes as a results of two types of motions:

1. *Out-of-plane motion* – due to the winglet's own pitch and heave displacement
2. *In-plane motion* – due to the vertical and angular displacement of inboard wing tip segment motion

Let us take a close look at Figure 3.6(a) and use it as a reference to determine the position of point P_2 when the winglet segment undergoes in- and out-of-plane deformation. The location of P_2 in relation to the inertial frame is obtained by using the following formulation:

$$\mathbf{r}_{P_2/O} = \mathbf{r}_{P_2/O'''} + \mathbf{r}_{O'''/O'} + \mathbf{r}_{O'/O}. \tag{3.9}$$

This definition represents the summation of the relative position of each point in its respective frame. By examining Figure 3.6(b), it is observed that $\mathbf{r}_{P_2/O}$ describes the relationship between the $\mathcal{I}$, $\mathcal{W}$, and $\mathcal{C}$ frames. The non-inertial frame $\mathcal{C}$ describes the position of point P_2 in its local coordinate system, $\mathcal{C} = (O''', \mathbf{c}_1, \mathbf{c}_2, \mathbf{c}_3)$. Moreover, more degrees of freedom have been incorporated to represent the displacement of the winglet segment.

Additionally, it can be noted that the winglet segment rotates by cant angle

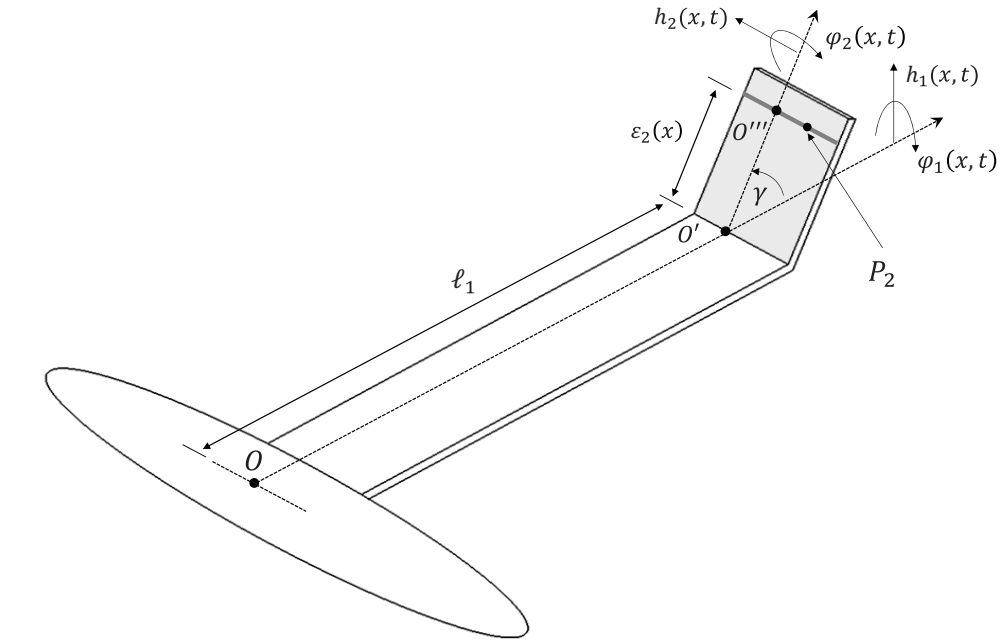

(a) Coordinates

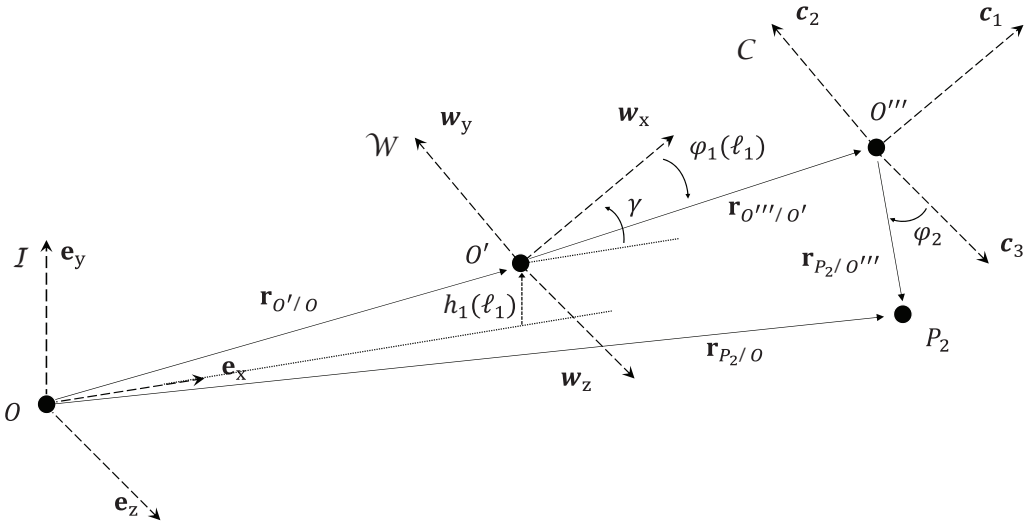

(b) Reference frames

Fig. 3.6: Location of point P_2 along the span of the wingletted wing and representation of vector components in the inertial frame $\mathcal{I}$ and non-inertial frames $\mathcal{W}$ and $\mathcal{C}$.

γ and pitch angle $\varphi_1(\ell_1)$, which is a result of the wing tip pitch motion. The non-inertial frame $\mathcal{W} = (O', \mathbf{w}_x, \mathbf{w}_y, \mathbf{w}_z)$ is defined by placing its origin a the segment joint, then rotating it around the z-axis by the cant angle γ (see Figure 3.7), such that the new axis is aligned to the undeformed winglet panel. Since both frames only differ by a simple rotation of γ, transformation Table 3.1 is used to express the vector position from frame $\mathcal{W}$ in frame $\mathcal{I}$.

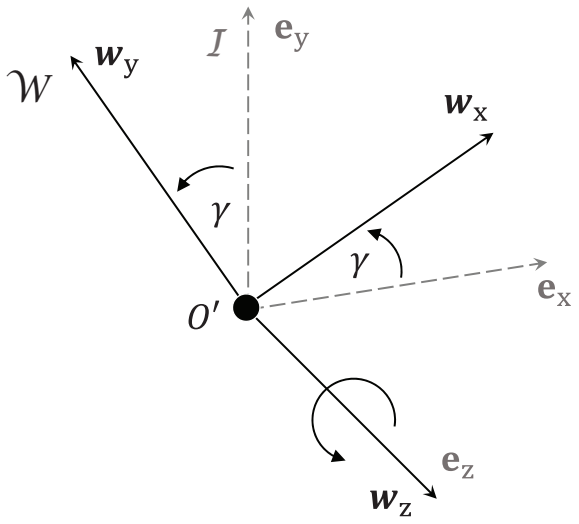

Fig. 3.7: Frame $\mathcal{I}$ rotated by cant angle γ about $\mathbf{e}_z$ to yield frame $\mathcal{W}$.

	$\mathbf{e}_x$	$\mathbf{e}_y$	$\mathbf{e}_z$
$\mathbf{w}_x$	$\cos(\gamma)$	$\sin(\gamma)$	0
$\mathbf{w}_y$	$-\sin(\gamma)$	$\cos(\gamma)$	0
$\mathbf{w}_z$	0	0	1

Tab. 3.1: Transformation table from frame $\mathcal{W}$ to frame $\mathcal{I}$.

Now, one has to account for the angular rotation of the winglet due to the wing segment tip pitch motion. As it is described in Figure 3.8, the non-inertial frame $\mathcal{W}'$ rotates around $\mathbf{e}_x$ by pitch angle $\varphi(\ell_1)$. This new intermediate frame describes

the orientation of the winglet relative to its origin O' when $\varphi_1(\ell_1)$ is applied. As a result, transformation Table 3.2 is used to account for this angle.

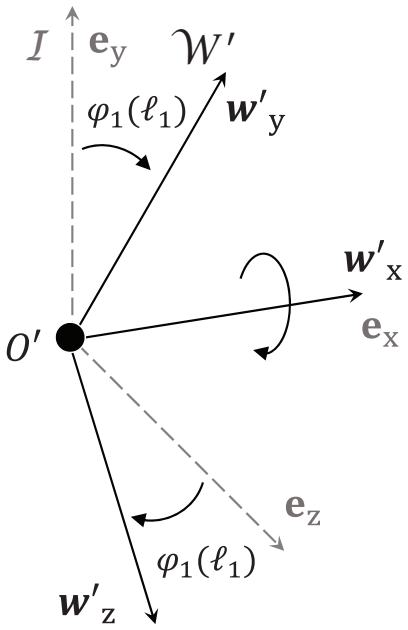

Fig. 3.8: Frames $\mathcal{W}'$ is obtained through rotation of frame $\mathcal{I}$ by pitch angle $\varphi(\ell_1)$ around $\mathbf{e}_x$.

	$\mathbf{e}_x$	$\mathbf{e}_y$	$\mathbf{e}_z$
$\mathbf{w}'_x$	1	0	0
$\mathbf{w}'_y$	0	$\cos(\varphi_1(\ell_1))$	$-\sin(\varphi_1(\ell_1))$
$\mathbf{w}'_z$	0	$\sin(\varphi_1(\ell_1))$	$\cos(\varphi_1(\ell_1))$

Tab. 3.2: Transformation table from frame $\mathcal{W}'$ to frame $\mathcal{I}$.

At this moment, it is possible to formulate an expressions that defines the chordwise position of P_2 in reference to O''' in the $\mathcal{C}$ frame, and the spanwise position

of O''' with respect to O in the $\mathcal{W}$. These expressions are described as follow

$$\mathbf{r}_{P_2/O'''} = 0\mathbf{c}_1 - d_{cm}\sin\big(\varphi_2(x)\big)\mathbf{c}_2 + d_{cm}\cos\big(\varphi_2(x)\big)\mathbf{c}_3, \tag{3.10}$$

$$\mathbf{r}_{O'''/O} = \varepsilon_2(x)\mathbf{w}_{\mathrm{x}} + h_2(x)\mathbf{w}_{\mathrm{y}} + 0\mathbf{w}_{\mathrm{z}}. \tag{3.11}$$

One can notice that frame $\mathcal{C}$ is aligned with the neutral axis and its vertical displacement is measured from the equilibrium point. As a result, Equation 3.10 is written in terms of the $\mathcal{W}$ frame coordinate system

$$\mathbf{r}_{P_2/O'''} = 0\mathbf{w}_{\mathrm{x}} - d_{cm}\sin\big(\varphi_2(x)\big)\mathbf{w}_{\mathrm{y}} + d_{cm}\cos\big(\varphi_2(x)\big)\mathbf{w}_{\mathrm{z}}. \tag{3.12}$$

The spanwise vector position of point P_2 in reference to O' on the winglet segment can be written as a liner combination of Equations 3.11 and 3.12, which leads to the following expression

$$\mathbf{r}_{P_2/O'} = \varepsilon_2(x)\mathbf{w}_{\mathrm{x}} + \Big[h_2(x) - d_{cm}\sin(\varphi_2(x))\Big]\mathbf{w}_{\mathrm{y}} + d_{cm}\cos(\varphi_2(x))\mathbf{w}_{\mathrm{z}}. \tag{3.13}$$

Notice that this formulation is very similar to the one given by Equation 3.7, which defined the position of P_1 in the inertial frame. In addition, Equation 3.13 does not include any angular rotations given by the winglet cant angle or the inboard wing tip segment pitch displacement.

One can consider Equation 3.13 and apply the rotations previously described in order to be able to write the position of point P_2 in reference the inertial frame.

First, the rotation given by the cant angle γ is applied. The application of the transformation Table 3.1 results in the following position vector of point P_2 in relation to O', which is given by

$$\begin{aligned}\mathbf{r}_{P_2/O'} &= \Big[\varepsilon_2(x)\cos(\gamma) - \big(h_2(x) - d_{cm}\sin(\varphi_2(x))\big)\sin(\gamma)\Big]\mathbf{e}_{\mathrm{x}} \\ &+\Big[\varepsilon_2(x)\sin(\gamma) + \big(h_2(x) - d_{cm}\sin(\varphi_2(x))\big)\cos(\gamma)\Big]\mathbf{e}_{\mathrm{y}} \\ &+\Big[d_{cm}\cos(\varphi_2)\Big]\mathbf{e}_{\mathrm{z}}. \end{aligned} \tag{3.14}$$

Subsequently, one can now consider the wing tip segment angular displacement $\varphi_1(\ell_1)$ and express the position of P_2 in frame $\mathcal{I}$ with its origin located at the joint. This leads to the following vector equation

$$\begin{aligned}\mathbf{r}_{P_2/O'} &= \Big[\varepsilon_2(x)\cos(\gamma) - \big(h_2(x) - d_{cm}\sin(\varphi_2(x))\big)\sin(\gamma)\Big]\mathbf{e}_{\mathrm{x}} \\ &+\Big[\Big(\varepsilon_2(x)\sin(\gamma) + \big(h_2(x) - d_{cm}\sin\big(\varphi_2(x)\big)\big)\cos(\gamma)\Big)\cos\big(\varphi_1(\ell_1)\big) \\ &-d_{cm}\cos\big(\varphi_2(x)\big)\sin\big(\varphi_1(\ell_1)\big)\Big]\mathbf{e}_{\mathrm{y}} \\ &+\Big[\Big(\varepsilon_2(x)\sin(\gamma) + \big(h_2(x) - d_{cm}\sin\big(\varphi_2(x)\big)\big)\cos(\gamma)\Big)\sin\big(\varphi_1(\ell_1)\big) \\ &+d_{cm}\cos\big(\varphi_2(x)\big)\cos\big(\varphi_1(\ell_1)\big)\Big]\mathbf{e}_{\mathrm{z}}. \end{aligned} \tag{3.15}$$

Now, one can translate the $\mathcal{I}$ frame by a distance ℓ_1, which denotes the span of the inboard wing segment, and include the heave displacement $h_1(\ell_1)$ due to the wing tip segment motion. This leads to a more complicated vector formulation that describes the spanwise location of point P_2 relative to the inertial frame $\mathcal{I}$ and it

origin O, that is written as:

$$\begin{aligned}
\mathbf{r}_{P_2/O'} &= \Big[\ell_1 + \varepsilon_2(x)\cos(\gamma) - \big(h_2(x) - d_{cm}\sin(\varphi_2(x))\big)\sin(\gamma)\Big]\mathbf{e}_{\mathrm{x}} \\
&+\Big[h_1(\ell_1) + \Big(\varepsilon_2(x)\sin(\gamma) + \big(h_2(x) - d_{cm}\sin\big(\varphi_2(x)\big)\big)\cos(\gamma)\Big)\cos\big(\varphi_1(\ell_1)\big) \\
&-d_{cm}\cos\big(\varphi_2(x)\big)\sin\big(\varphi_1(\ell_1)\big)\Big]\mathbf{e}_{\mathrm{y}} \\
&+\Big[\Big(\varepsilon_2(x)\sin(\gamma) + \big(h_2(x) - d_{cm}\sin\big(\varphi_2(x)\big)\big)\cos(\gamma)\Big)\sin\big(\varphi_1(\ell_1)\big) \\
&+d_{cm}\cos\big(\varphi_2(x)\big)\cos\big(\varphi_1(\ell_1)\big)\Big]\mathbf{e}_{\mathrm{z}}. \qquad (3.16)
\end{aligned}$$

Applying the small angle approximation leads to Equation 3.17 where it can be noticed that it retained some level of complexity representing the position of P_2 as a function of the pitch and heave motion along the span of the wing and winglet segments.

$$\begin{aligned}
\mathbf{r}_{P_2/O} &= \Big[\ell_1 + \varepsilon_2(x)\cos(\gamma) - \big(h_2(x) - d_{cm}\varphi_2(x)\big)\sin(\gamma)\Big]\mathbf{e}_{\mathrm{x}} \\
&+\Big[h_1(\ell_1) + \varepsilon_2(x)\sin(\gamma) + \big(h_2(x) - d_{cm}\varphi_2(x)\big)\cos(\gamma) - d_{cm}\varphi_1(\ell_1)\Big]\mathbf{e}_{\mathrm{y}} \\
&+\Big[\Big(\varepsilon_2(x)\sin(\gamma) + \big(h_2(x) - d_{cm}\varphi_2(x)\big)\cos(\gamma)\Big)\varphi_1(\ell_1) + d_{cm}\Big]\mathbf{e}_{\mathrm{z}}. \qquad (3.17)
\end{aligned}$$

Recall our equation for $\mathbf{r}_{P_1/O}$

$$\mathbf{r}_{P_1/O} = \varepsilon_1(x)\mathbf{e}_{\mathrm{x}} + \Big[h_1(x) - d_{cm}\varphi_1(x)\Big]\mathbf{e}_{\mathrm{y}} + d_{cm}\mathbf{e}_{\mathrm{z}}, \qquad (3.8)$$

which describes the position of point P_1 in the $\mathcal{I}$ frame. Now by using Equations 3.8 and 3.17 one can define the spanwise position of any point P_i on a wingletted

wing system.

3.2.2.2 Kinetic Energy

In order to proceed with the implementation of Hamilton's Principle, it is necessary to obtain the total kinetic energy of the system T_{total}. In general, for structural dynamic systems the kinetic energy can be expressed in terms of the first time derivative of the position. This is done by using the following definition:

$$^{\mathcal{I}}\mathbf{V}_{P_i/O} = \frac{^{\mathcal{I}}d}{dt}(\mathbf{r}_{P_i/O}). \tag{3.18}$$

It describes the changes in magnitude and direction of a point P_i as a function of time in three directions with respect to a reference frame [53, 54].

By using our definition for the vector derivative, one can proceed to take the first time derivative of Equations 3.8 and 3.17 to formulate the velocity equations for P_1 and P_2 with respect to the inertial frame $\mathcal{I}$. Consequently, they are written as:

$$^{\mathcal{I}}\mathbf{V}_{P_1/O} = 0\mathbf{e}_{\mathrm{x}} + \Big[\dot{h}_1(x) - d_{cm}\dot{\varphi}_1(x)\Big]\mathbf{e}_{\mathrm{y}} + 0\mathbf{e}_{\mathrm{z}} \tag{3.19}$$

$$\begin{aligned} ^{\mathcal{I}}\mathbf{V}_{P_2/O} = & \Big[\big(d_{cm}\dot{\varphi}_2(x) - \dot{h}_2(x)\big)\sin(\gamma)\Big]\mathbf{e}_{\mathrm{x}} \\ & + \Big[\dot{h}_1(\ell_1) + \big(\dot{h}_2(x) - d_{cm}\dot{\varphi}_2(x)\big)\cos(\gamma) - d_{cm}\dot{\varphi}_1(\ell_1)\Big]\mathbf{e}_{\mathrm{y}} \\ & + \Big[\Big(\varepsilon_2(x)\sin(\gamma) + \big(h_2(x) - d_{cm}\varphi_2(x)\big)\cos(\gamma)\Big)\dot{\varphi}_1(\ell_1) \\ & + \dot{h}_2(x)\cos(\gamma)\varphi_1(\ell_1) - d_{cm}\dot{\varphi}_2(x)\varphi_1(\ell_1)\Big]\mathbf{e}_{\mathrm{z}}. \end{aligned} \tag{3.20}$$

Notice that Equation 3.19 only denotes motion in the y-direction for the inner wing segment. This comes as a result of our assumption of rigid cross-section, which does not allow for displacement along the $x-$ and $z-$ axes. From Equation 3.20, it is observed that the winglet exhibits out-of-plane deformation due to its elastic properties. This is indicated by the $\dot{\varphi}_2(x)$ and $\dot{h}_2(x)$ terms. The $\dot{\varphi}_1(\ell_1)$ and $\dot{h}_1(\ell_1)$ terms account for the rigid body motion of the winglet due to the pitch and heave motion of the inboard wing segment. This causes the outer wing to translate vertically and to rotate about its own axis. The higher order term in Equation 3.20 are a result of elastic and rigid interaction of both wing panels. However, these terms can be neglected and Equation 3.20 becomes

$$\begin{aligned} {}^{\mathcal{I}}\mathbf{V}_{P_2/O} &= \Big[\big(d_{cm}\dot{\varphi}_2(x) - \dot{h}_2(x)\big)\sin(\gamma)\Big]\mathbf{e}_{\mathrm{x}} \\ &+\Big[\dot{h}_1(\ell_1) - d_{cm}\dot{\varphi}_1(\ell_1) + \big(\dot{h}_2(x) - d_{cm}\dot{\varphi}_2(x)\big)\cos(\gamma)\Big]\mathbf{e}_{\mathrm{y}} \\ &+\Big[\varepsilon_2(x)\sin(\gamma)\dot{\varphi}_1(\ell_1)\Big]\mathbf{e}_{\mathrm{z}}. \end{aligned} \tag{3.21}$$

The kinetic energy of the system is obtained from the integration of the square of the velocity of each wing section. Thus, the total kinetic energy of a dynamic system is given by Equation 3.23 [50]:

$$T_i = \frac{1}{2}\int_0^{\ell_i} m_i(x_i)\Big[\frac{\partial u_i}{\partial t}\Big]^2 dx_i = \frac{1}{2}\int_0^{\ell_i} m_i(x_i)\big[{}^{\mathcal{I}}\mathbf{V}_{P/O_i}\big]^2 dx_i \tag{3.22}$$

$$T_{total} = \sum_{n=1}^{n} T_i \tag{3.23}$$

3.2.2.3 Potential Energy

Now, one can derive expressions for the elastic potential energy in the system. To keep the process as clear as possible, let us first consider a beam in pure bending. Therefore, from Hook's law, it yields an expression for the bending stress of a beam in the form

$$\sigma_{xx} = E\epsilon_{xx} = -Ey\frac{\partial^2 h}{\partial x^2}. \tag{3.24}$$

Here, the ϵ_{xx} term refers to the strain-displacement, y denotes the vertical coordinate, and E is defined as the Young's Modulus of elasticity [55]. In addition, it is considered that h is changing in the spanwise direction x. An expression for the strain energy of a beam in bending is given by:

$$V_{i,bending} = \frac{1}{2}\int_0^{\ell_i} EI_i(x_i)\left[\frac{\partial^2 h_i}{\partial {x_i}^2}\right]^2 dx_i, \tag{3.25}$$

where I is the area moment of inertia of the beam cross-section, and i denotes the $i-th$ element or segment.

As a next step, one can formulate an expression that describes the strain energy of a beam undergoing torsional deformation. A process similar to the one performed for the beam in bending is applied. It is assumed that the shear stress distribution of the beam occurs across its cross-section [41]. This is shown in the following formulation:

$$\tau = \frac{\mathbb{T}r}{J}. \tag{3.26}$$

$\mathbb{T}$ defines the resisting torque in the cross-section and r is the distance from the shear center of the beam to point P. Also, J denotes the polar moment of inertia of the beam cross-section. As a result, the strain energy of a beam undergoing torsion is presented as:

$$V_{i,torsion} = \frac{1}{2}\int_0^{\ell_i} GJ_i(x_i)\left[\frac{\partial\varphi_i}{\partial x_i}\right]^2 dx_i. \tag{3.27}$$

Both expressions for the potential energy of a beam undergoing bending and twist are combined to yield the following formulation:

$$V_i = \frac{1}{2}\int_0^{\ell_i} EI_i(x_i)\left[\frac{\partial^2 h_i}{\partial {x_i}^2}\right]^2 dx_i + \frac{1}{2}\int_0^{\ell_i} GJ_i(x_i)\left[\frac{\partial\varphi_i}{\partial x_i}\right]^2 dx_i. \tag{3.28}$$

$$V_{total} = \sum_{n=1}^{n} V_i. \tag{3.29}$$

Equation 3.29 represents the total potential energy of the wingletted wing structure. Note that equation 3.28 does not show contributions to the potential energy of the outer wing due to the motion of the inner wing, and vice versa.

3.2.2.4 Non-conservative Forces

In general, for aeroelastic analysis, the non-conservative or non-potential forces acting on the system are due to the aerodynamic loading. This can be presented as the virtual work done by the aerodynamic pressure p on a plate:

$$\overline{\delta W}_{i,nc} = \int\int p\delta y dx dz. \tag{3.30}$$

Since the deflection of this system is a consequence of the linear combination

of pitch and heave motion along the span of the wing, it leads to the following function:

$$\overline{\delta W}_{i,nc} = \int_0^{\ell_i} L_i \delta h_i(x_i) dx_i + \int_0^{\ell_i} Ma_i \delta \varphi_i(x_i) dx_i \tag{3.31}$$

It describes the spanwise aerodynamic loading in each degree of freedom, where L_i is the net lift per unit span, and the distributed moment about the x-axis is defined by Ma_i. It is important to mention that the aerodynamic forces and moments take into consideration the winglet segment kinematics in the final expression. Therefore, the virtual work done by the aerodynamic loading is expressed as:

$$\begin{aligned}\overline{\delta W}_{nc} = &\int_0^{\ell_1} \Big(L_1 \delta h_1(x_1) + Ma_1 \delta \varphi_1(x_1) \Big) dx_1 \\ &+ \int_0^{\ell_2} \Big(L_2 [\delta h_1(\ell_1) \cos(\gamma) + \delta h_2(x_2)] \\ &+ Ma_2 \big[\delta \varphi_1(\ell_1) \cos(\gamma) + \delta \varphi_2(x_2) \big] \Big) dx_2. \end{aligned} \tag{3.32}$$

3.2.3 Formulation of the Equations of Motion

As of now, all the equations representing the kinetic energy, potential energy, and virtual work of the system have been defined. Let us collect those equations and recall Equation 3.1 to formulate the equations of motion that describe this distributed parameter system.

Then one can recall our definitions for kinetic energy given by Equations 3.22 and 3.23 and substitute $\mathbf{V}_{P/O_1}$ and $\mathbf{V}_{P/O_2}$. From that, it is possible to provide the

total kinetic energy as follow:

$$\begin{aligned}\delta T &= \frac{1}{2}\int_0^{\ell_1} m_1(x)\Big(\dot{h}_1(x) - d_{cm}\dot{\varphi}_1(x)\Big)^2 dx \\ &+ \frac{1}{2}\int_0^{\ell_2} m_2(x)\Bigg[\Big(-\big(\dot{h}_2(x) - d_{cm}\dot{\varphi}_2(x)\big)\sin(\gamma)\Big)^2 \\ &+ \Big(\dot{h}_1(\ell_1) - d_{cm}\dot{\varphi}_1(\ell_1) + \big(\dot{h}_2(x) - d_{cm}\dot{\varphi}_2(x)\big)\cos(\gamma)\Big)^2 + \Big(\varepsilon_2(x)\dot{\varphi}_1(\ell_1)\Big)^2\Bigg] dx. \end{aligned} \tag{3.33}$$

Note that this equation contains additional terms describing the contributions of the mass of the winglet onto the wing section.

Consequently, the application of Hamilton's Principle leads to four partial differential equations that characterize the dynamic aeroelastic system, and they are similar to the ones provided by Liska and Dowell [56]. They are presented as follows:

$$m_1\ddot{h}_1(x_1,t) - S_{\varphi 1}\ddot{\varphi}_1(x_1,t) + EI_1{h_1}^{IV}(x_1,t) = L_1(x_1,t), \tag{3.34}$$

$$-S_{\varphi 1}\ddot{h}_1(x_1,t) + I_{\varphi 1}\ddot{\varphi}_1(x_1,t) - GJ_1{\varphi_1}''(x_1,t) = Ma_1(x_1,t), \tag{3.35}$$

$$\begin{aligned} m_2\Big[\ddot{h}_1(\ell_1,t)\cos(\gamma) + \ddot{h}_2(x_2,t)\Big] &- S_{\varphi 2}\Big[\ddot{\varphi}_1(\ell_1,t)\cos(\gamma) + \ddot{\varphi}_2(x_2,t)\Big] \\ +EI_2{h_2}^{IV}(x_2,t) &= L_1(\ell_1,t)\cos(\gamma) + L_2(x_2,t), \end{aligned} \tag{3.36}$$

$$\begin{aligned} -S_{\varphi 2}\Big[\ddot{h}_1(\ell_1,t)\cos(\gamma) + \ddot{h}_2(x_2,t)\Big] &+ I_{\varphi 2}\Big[\ddot{\varphi}_1(\ell_1,t)\cos(\gamma) + \ddot{\varphi}_2(x_2,t)\Big] \\ -GJ_2{\varphi_2}''(x_2,t) &= Ma_1(\ell_1,t)\cos(\gamma) + Ma_2(x_2,t). \end{aligned} \tag{3.37}$$

where $m_i = \int \rho_b dz \rightarrow$ linear mass,

$S_{\varphi_i} = \int \rho_b d_{cm} dz \rightarrow$ static imbalance moment

$I_{\varphi_i} = \int \rho_b d_{cm}^2 dz \rightarrow$ moment of inertia,

$\rho_b \rightarrow$ mass per unit chord length.

Notice that they contain fourth and second order partial derivatives in space for bending and torsion, respectively. In addition, they are second order in time. All four equations represent the pitch and heave motion of the structure under dynamic loading due to aerodynamics. Specifically, Equations (3.34) and (3.35) characterize the wing segment, whereas the winglet motion is represented by equations (3.36) and (3.37). The governing equations denote that the system exhibits inertia coupling in pitch and heave. Another important remark is that the winglet governing equations include terms that represent the displacement contributions from the wing tip translation and rotational displacement onto the winglet or outer wing segment.

As it was previously mentioned, in addition to the governing equations, Hamilton's Principle yields the geometric and natural boundary conditions of the system, which are presented in Table 3.3. It can be observed that expressions for $y_1(\ell_1)$ and $y_2(\ell_2)$ represent the natural boundary conditions, whereas the remaining expressions ($y_1(0)$ and $y_2(0)$) are the geometric boundary conditions.

	Wing Section
$y_1(0)$	$h_1(0) = 0, \quad h_1'(0) = 0, \quad \varphi_1(0) = 0$
$y_1(\ell_1)$	$\sin^2(\gamma)\left(m_2\ell_2\ddot{h}_1(\ell_1) - S_{\varphi_2}\ell_2\ddot{\varphi}_1(\ell_1)\right) + EI_2h_2'''(\ell_1)\cos(\gamma) - EI_1h_1'''(\ell_1) = 0$ $-EI_2h_2''(\ell_1)\cos(\gamma) + EI_1h_1''(\ell_1) = 0$ $-\sin^2(\gamma)\left(S_{\varphi_2}\ddot{h}_1(\ell_1) + \left(\frac{1}{3}m\ell_2^3 + I_{\varphi_2}\ell_2\right)\ddot{\varphi}_1(\ell_1)\right) + GJ_1\varphi_1'(\ell_1) -$ $GJ_2\varphi_2'(\ell_1)\cos(\gamma) = 0$
	Winglet Section
$y_2(0)$	$h_2(0) = h_1(\ell_1)\cos(\gamma), \quad h_2'(0) = h_1'(\ell_1)\cos(\gamma), \quad \varphi_2(0) = \varphi_1(\ell_1)cos(\gamma)$
$y_2(\ell_2)$	$h_2''(\ell_2) = 0, \quad h_2'''(\ell_2) = 0, \quad \varphi_2'(\ell_2) = 0$

Tab. 3.3: Geometric and natural boundary conditions for the wingletted wing system.

3.3 Aerodynamic Flow Modeling

Thus far, the equations of motion for a system under exogenous forces and moments have been established. However, they are not complete because the aerodynamic forces and moment have not been defined. It is necessary to look at another important aspect of the aeroelastic problem, namely the determination of the aerodynamic loads, in order to associate the distributed loads to the motion of the wing. This can be done in different ways. Nevertheless, in this work, it will be done through the application of *Strip Theory*.

3.3.1 Definition and Application of Strip Theory

Strip Theory estimates the distributed aerodynamic loads by integrating two-dimensional loads along the span. A wing is divided into a series of strips of infinitesimal width dx along the span of the wing (See Figure 3.9) [3,4]. Consequently, from two-dimensional flow theory, the lift force at every strip or spanwise station is attributed to the local angle of twist (or angle of attack). However, this theory ignores the downwash induced by the trailing vortices at the wing tip and overestimates the lift. Therefore, the lift produced at any spanwise station is independent of the other stations. It also assumes a spanwise uniform lift and moment distribution on the wing panels.

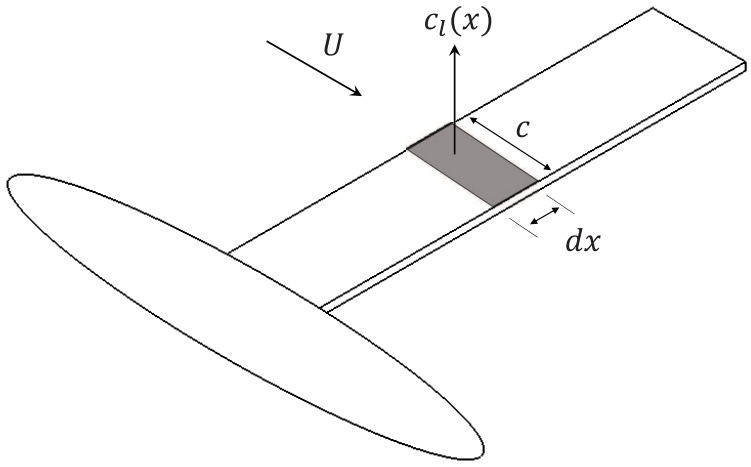

Fig. 3.9: Strip Theory representation - strip of infinitesimal width dx and local lift coefficient $c_l(x)$ along the span of a continuous wing.

The implementation of Strip Theory allows the introduction of three aerodynamic flow models, namely the Steady, Quasi-steady, and Unsteady flow. These

flow models provide increasing levels of complexity. For instance, the steady flow model is the simplest of all. It assumes that the local lift generated is directly proportional to the local angle of attack α. The quasi-steady flow model considers the effective angle of attack α_{eff}, which is due to the linear combination of the local angle of attack α and the heave or bending rate $\dot{h}$ of the wing segment [5]. The most complex of all three models is the unsteady flow model. Unlike the quasi-steady flow, it considers the effects of the wake around an oscillating wing cross-section. Moreover, this model incorporates Theodorsen's function $C(k)$, which depends on reduced frequency k [11, 46].

3.3.2 Steady Flow

The steady flow model is very simple. It considers the wing to be fixed relative to the incoming airstream, but it does not consider the effects of the vortices shed into the wake. Thus, it states that the lift generated is directly proportional to the local angle of attack α.

$$c_l(x) = c_{l_\alpha}\alpha(x), \tag{3.38}$$

where $c_{l\alpha}$ and α denote the theoretical two-dimensional lift slope and local angle of attack, respectively. Therefore, the spanwise lift distribution is defined as:

$$dL = \frac{1}{2}\rho U^2 c c_{l_\alpha}\alpha(x)dx. \tag{3.39}$$

The incoming airstream density is identified as ρ. The c term refers to the wing chord length. This is defined as $c = 2b$, where b is the half-chord length. Because the wing undergoes twist deformation, it can be assumed that the local angle of attack is equal to the local angle of twist, $\alpha = \varphi$. To compute, the aerodynamic moment the lift force is multiplied by $d_{ac} = be$, where e is a non-dimensionalized value of the semi-chord b. Hence, the distributed aerodynamic lift $L(x,t)$ and moment $M_a(x,t)$ about the elastic axis spanning the length of the wing can be expressed as:

$$L(x,t) = \frac{1}{2}\rho U^2 c c_{l_\alpha} \varphi(x,t) = 2\pi\rho U^2 b \varphi(x,t), \tag{3.40}$$

$$M_a(x,t) = 2\pi\rho U^2 b^2 e \varphi(x,t). \tag{3.41}$$

As it can be observed, the aerodynamic loads are independent of time. This means that there are not any frequency dependent effects. Thus, the aerodynamic forces and moments remain constant over time.

3.3.3 Quasi-steady Flow

This flow model considers that the wing undergoes pitch and heave motion relative to the incoming airstream U as it is shown in Figure 3.10. In addition, the quasi-steady flow model does not consider frequency dependencies, which is valid for a slow varying motion. As a result, this model neglects the temporal memory or variations over time of the aerodynamic forces and moments [4, 5]. The associated aerodynamic forces and moments are computed based on the instantaneous orientation and velocity of the wing.

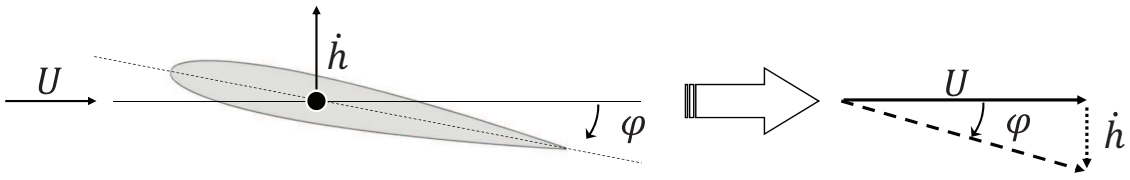

Fig. 3.10: Wing undergoing pitch and heave motion relative to the incoming flow.

In this flow model, the only time dependency is a result of the wing kinematics, which now produces a dynamic force [57]. As a results, it is appropriate to introduce a new term, the effective angle of attack α_{eff}. It can be written as:

$$\alpha_{eff} = \varphi(x) - \frac{\dot{h}(x)}{U}, \tag{3.42}$$

where $\dot{h}/U$ refers to the heave rate relative to the incoming flow U. The previous equation shows that the local angle of attack is affected by the local heave motion [45]. One can now substitute α_{eff} into Equations 3.40 and 3.41 to obtain the final expression for the Quasi-steady aerodynamic lift and moment:

$$L(x,t) = 2\pi\rho U b\big[U\varphi(x,t) - \dot{h}(x,t)\big], \tag{3.43}$$

$$Ma(x,t) = 2\pi\rho U b^2 e\big[U\varphi(x,t) - \dot{h}(x,t)\big]. \tag{3.44}$$

Note that the quasi-steady flow model does not present a dependency on the pitch rate $\dot{\varphi}$. This is generally attributed to the fact that, the aerodynamic pitching moment around the aerodynamic center, $\frac{c}{4}$, is essentially a constant with respect to

changes in angle of attack. Therefore, the effects of the pitching moment are being neglected. The only source of aerodynamic moment considered in this formulation is the one produced by the lift at a distance d_{ac} from the elastic axis (See Figure 3.1).

Equations 3.43 and 3.44 will be later substituted into the governing equations to produce a complete set of aeroelastic equations that represent the wingletted wing system.

3.3.4 Unsteady Flow

Thus far in this chapter, the effects of the changing circulation and wake around the wing have been neglected. However, these dynamic effects can significantly affect the resulting aerodynamic forces and moment, specially at higher frequencies (e.g. reduced frequency $k > 0.1$). Therefore, an unsteady flow model is required for accurate flutter speed predictions.

3.3.4.1 Theodorsen's Theory for Unsteady Flow

For flutter analysis, unsteady aerodynamic behavior is presented as a function of reduced frequency k, where

$$k = \frac{\omega b}{U}. \tag{3.45}$$

Here, b is the half-chord of the wing, ω denotes circular frequency, and U is the incoming flow velocity. This non-dimensionalized frequency parameter is presented as a measure of unsteadiness in the airstream [2]. Therefore, in unsteady flows the

magnitude of the aerodynamic lift and moment are dependent on the frequency of the oscillation of the wing. In addition, there is a phase lag between the wing motion and the unsteady forces.

To model the changes in amplitude and phase in unsteady flow, *Theodorsen's Function* will be used. In 1934, Theodorsen derived a theory of unsteady aerodynamics for a thin airfoil or flat plate. His theory was based on potential flow and the Kutta condition, which is equivalent to that definition in the steady flow case [5, 11]. From his analysis, it is observed that the aerodynamic lift and moment are divided into two parts, which are the result of two physical phenomena, namely *circulatory* and *non-circulatory effects*. The circulatory effects are due to the vorticity in the flow. They are responsible for the lift generated from circulation via Kutta-Joukowski law, $L' = \rho U \Gamma$. Typically, these terms are of major importance. On the other hand, non-circulatory or apparent mass and inertia effects are not as important, specially at low reduced frequencies. They are the result of the mass of the air that accelerates with the airfoil. Since the air has a finite mass, it generates a reactive force and moment onto the wing.

From Theodorsen's theory, the classical representation of the distributed aero-

dynamic loads is presented as:

$$
\begin{aligned}
L(x,t) &= \pi\rho b^2\Big[U\dot{\varphi}(x,t) - \ddot{h}(x,t) - ba\ddot{\varphi}(x,t)\Big] \\
&\quad + 2\pi\rho bC(k)\left[U\varphi(x,t) - \dot{h}(x,t) + b\left(\frac{1}{2}-a\right)\dot{\varphi}(x,t)\right], \qquad (3.46)\\
M_a(x,t) &= \pi\rho b^3\left[a\ddot{h}(x,t) + U\left(\frac{1}{2}-a\right)\dot{\varphi}(x,t) - b\big(\frac{1}{8}-a^2\big)\ddot{\varphi}(x,t)\right] \\
&\quad + 2\pi\rho b^2\left(a+\frac{1}{2}\right)C(k)\left[U\varphi(x,t) - \dot{h}(x,t) + b\left(\frac{1}{2}-a\right)\dot{\varphi}(x,t)\right]. \qquad (3.47)
\end{aligned}
$$

There are a couple of points worth mentioning from both equations. Notice that the definition of effective angle of attack is not as simple as in the steady and quasi-steady flow cases. The reason is that the flow direction varies in the chordwise direction as the result of the induced flow. The effective angle of attack α_{eff} is:

$$
\alpha_{eff}(x,t) = \left[\varphi(x,t) - \frac{\dot{h}(x,t)}{U} + \frac{b}{U}\left(\frac{1}{2}-a\right)\dot{\varphi}(x,t)\right]. \qquad (3.48)
$$

In other words, if motion of the airfoil is relatively slow and small, then the flow field around it remains in equilibrium. Consequently, the attributions from $\dot{\varphi}$ and $\dot{h}$ are perceived as an effective angle of attack and effective camber of the airfoil section, respectively.

Another aspect to be noted is the presence of the circulatory and non-circulatory terms. The first part of the Equations 3.46 and 3.47 represents the non-circulatory terms, and the second part denotes the circulatory terms [2,5]. The circulatory terms are dependent on Theodorsen's function $C(k)$. This is a complex valued function

dependent on reduced frequency, and it is presented in terms of Hankel functions as follows

$$C(k) = F(k) + iG(k) = \frac{H_1^{(2)}(k)}{H_1^{(2)}(k) + iH_0^{(2)}(k)}, \tag{3.49}$$

where, $F(k)$ and $G(k)$ denote the real and imaginary parts of the function, respectively. Also, $H_n^{(2)}(k)$ represents Hankel functions of the second kind. It can then be written as:

$$H_n^{(2)}(k) = J_n(k) - iY_n(k), \tag{3.50}$$

where $J_n(k)$ and $Y_n(k)$ correspond to the Bessel functions of the first and second kind, respectively [46].

Theodorsen's function is plotted in Figure 3.11. The function follows a clockwise direction for increasing k. As the value of k increases, $F(k)$ approaches 1/2. Then, $G(k) \to 0$ and $G(k) = 1/2$. This indicates that for unsteady flow the magnitude of the aerodynamic loads is reduced. Similar results are observed in the frequency response plots depicted Figure 3.12, which provides additional information. It is observed that a phase lag is introduced. Note that when k increases the phase lag also increases until $k \approx 0.3$. Beyond that point, the phase lag is reduced and the amplitude of the lift decreases to one half.

This set of aerodynamic equations will later be used to yield a more complex aeroelastic model. At the same time, one can seek the unstable condition in terms of k, which will lead to the flutter speed for the wingletted wing system.

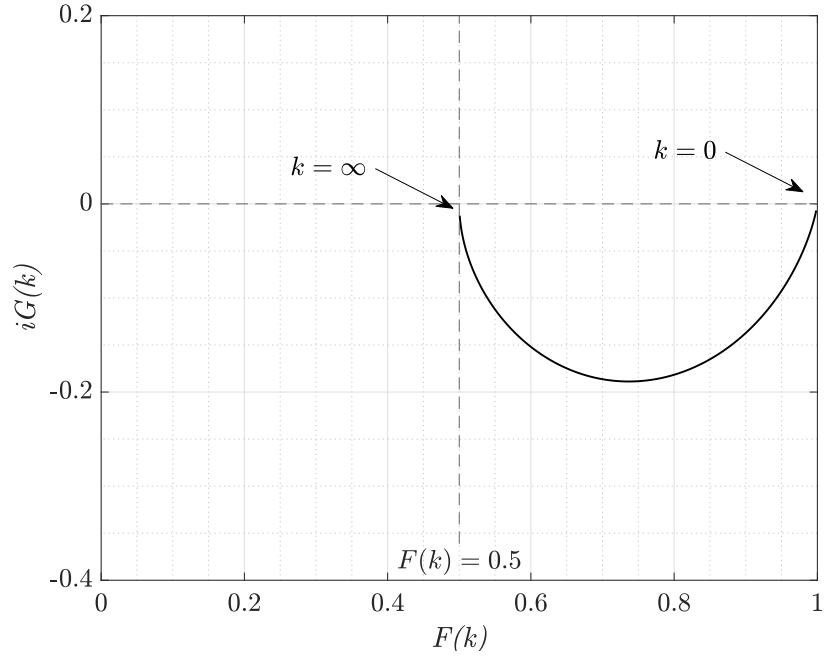

Fig. 3.11: Theodorsen's function $C(k) = F(k) + iG(k)$

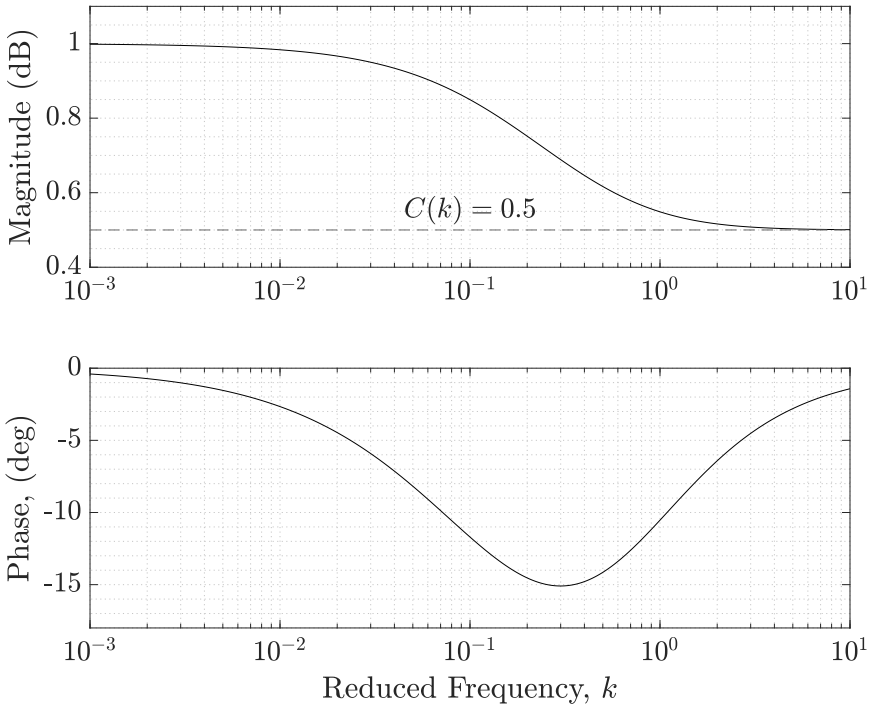

Fig. 3.12: Frequency response of Theodorsen's function $C(k)$

3.4 Aeroelastic Equations of Motion

In this section, the equations describing the aerodynamic forces are coupled with the structural equations. Hence, the equations of motion of the dynamic aeroelastic system take the following canonical form:

$$[M_s - M_{aero}]\{\ddot{\phi}\} + [C_{aero}]\{\dot{\phi}\} + [K_s - K_{aero}]\{\phi\} = 0. \tag{3.51}$$

The $[M_s]$ term represents the inertial properties of the structure, whereas $[M_{aero}]$ is the added mass of the air around the body in the case of unsteady flow. When either the steady or quasi-steady flow models are considered, $[M_{aero}]$ is equal to zero because both models neglect the effects of changing circulation around the wing. The aerodynamic damping is identified as $[C_{aero}]$, which is non-zero for the quasi-steady and unsteady flow models. The effective stiffness of the system is represented as the difference between the structural stiffness $[K_s]$ and the aerodynamic stiffness $[K_{aero}]$. Finally, the generalized coordinates are presented as ϕ. Equation 3.51 describes the fundamental interaction between the inertial, flexible, and the aerodynamic forces.

3.4.1 Dynamic Aeroelastic Models

To better understand the generalized aeroelastic model previously explained, consider the equations of motion for a planar wing. Now, one can introduce the aerodynamic models previously discussed into the governing equations, which become:

- *Aeroelastic steady flow model*

$$m\ddot{h}(x,t) - S_\varphi\ddot{\varphi}(x,t) + EIh^{IV}(x,t) = 2\pi\rho U^2 b\varphi(x,t), \tag{3.52}$$

$$-S_\varphi\ddot{h}(x,t) + I_\varphi\ddot{\varphi}(x,t) - GJ\varphi''(x,t) = 2\pi\rho U^2 b^2 e\varphi(x,t). \tag{3.53}$$

- *Aeroelastic quasi-steady flow model*

$$m\ddot{h}(x,t) - S_\varphi\ddot{\varphi}(x,t) + EIh^{IV}(x,t) = 2\pi\rho Ub\big[U\varphi(x,t) - \dot{h}(x,t)\big], \tag{3.54}$$

$$-S_\varphi\ddot{h}(x,t) + I_\varphi\ddot{\varphi}(x,t) - GJ\varphi''(x,t) = 2\pi\rho Ub^2 e\big[U\varphi(x,t) - \dot{h}(x,t)\big]. \tag{3.55}$$

- *Aeroelastic unsteady flow model*

$$\begin{aligned} m\ddot{h}(x,t) - S_\varphi\ddot{\varphi}(x,t) + EIh^{IV}(x,t) &= \pi\rho b^2\Big[U\dot{\varphi}(x,t) - \ddot{h}(x,t) - ba\ddot{\varphi}(x,t)\Big] \\ &\quad + 2\pi\rho bC(k)\left[U\varphi(x,t) - \dot{h}(x,t) + b\left(\frac{1}{2} - a\right)\dot{\varphi}(x,t)\right], \end{aligned} \tag{3.56}$$

$$\begin{aligned} -S_\varphi\ddot{h}(x,t) + I_\varphi\ddot{\varphi}(x_1,t) - GJ{\varphi_1}''(x,t) &= \\ &\pi\rho b^3\left[a\ddot{h}(x,t) + U\left(\frac{1}{2} - a\right)\dot{\varphi}(x,t) - b\big(\frac{1}{8} - a^2\big)\ddot{\varphi}(x,t)\right] \\ &\quad + 2\pi\rho b^2\left(a + \frac{1}{2}\right)C(k)\left[U\varphi(x,t) - \dot{h}(x,t) + b\left(\frac{1}{2} - a\right)\dot{\varphi}(x,t)\right]. \end{aligned} \tag{3.57}$$

One will notice that for all models the $\{\dot{h}, \dot{\varphi}\}^T$ and $\{h, \varphi\}^T$ terms are dependent on the incoming airstream velocity, from which one can develop terms regarding the aerodynamic damping and stiffness. This plays an importation role in the aeroelastic stability of the system, because the magnitude of these terms changes as the

incoming flow velocity increases. Similar remarks are observed for the equations of motion of the wingletted wing.

3.5 Chapter Summary

This chapter showed the derivation process to obtain a dynamic aeroelastic model associated with the wingletted wing system in this research. First, the structural model was developed through the implementation of beam theory and multibody kinematics. This allowed the formulation of expressions for the position and velocity of any point P_i along the span of the inboard and outboard wing segments or panels. The kinematic equations indicated that the winglet segment is rotating and translating due to pitch and heave motion of the joint section. By means of Hamilton's Principle, the expressions for the kinetic energy, potential energy and non-conservative forces lead to a set of nonhomogeneous equations of motion. Later, two-dimensional flow theory was employed to produce three aerodynamic models, namely *steady, quasi-steady, and unsteady flow*. These aerodynamic models were used describe a uniform spanwise lift and moment distribution. The aeroelastic equations of motion are the result of the coupling between the aerodynamic and structural models. From that, one can observe how the effective stiffness and damping of the system change as a function of the incoming flow velocity.

Chapter 4: System Discretization and Flutter Analysis

4.1 Overview

The previous chapter focused on the derivation of the equations of motion of the wingletted wing, which is a distributed parameter system. However, for a complex systems, it is not feasible to obtain a solution for the continuous system, and therefore a discretized approach is employed to enable a solution. This is due to the fact that discretized systems have a finite number of degrees of freedom compared to the continuous systems that have an infinite number of degrees of freedom [50]. Therefore, for complex dynamical systems, it is often convenient to employ an energy method to derive the governing equations of an n-degree-of-freedom system. This allows approximation of the dynamic behavior of a continuous system and yields a linear set of ordinary differential equations.

With the development of the discretized aeroelastic equations, our attention can be turned to investigate the stability boundaries of the system. The stability characteristics of a system with n degrees of freedom are obtained via formulation of the eigenvalue problem. At the same time, this leads to the system frequencies and damping ratios for multiple flight conditions.

4.2 System Discretization

Let us consider a solution that is separable in space and time for a continuous system given by

$$w(x,t) = \xi(x)\phi(t). \tag{4.1}$$

This formulation represents a single-degree-of-freedom continuous system where $\xi(x)$ and $\phi(t)$ denote the shape functions and generalized coordinates, respectively [50]. For an n-degree-of-freedom system, let us take Equation 4.1 and include n shape functions. This leads to a finite sum that approximates displacement of the continuous system

$$w(x,t) = \sum_{i=1}^{n} \xi_i(x)\phi_i(t). \tag{4.2}$$

In this case, $\xi_i(x)$ represents the n shape or trial functions, and ϕ_i denotes the generalized coordinates, pitch and heave. This formulation allows the implementation of two discretization methods, namely the *Rayleigh-Ritz Method* (RRM) and the *Finite Element Method* (FEM). The Rayleigh-Ritz Method is more physical in nature because it uses a finite series of functions that represent the deformation of the entire structure. However, this method is as good as the functions applied to describe the response of the system. The Finite Element Method has a more solid mathematical foundation. This approach uses elemental functions for local interpolation rather than global. Both methods lead to a linear set of ordinary differential equations and therefore both methods provide rigor.

4.2.1 Rayleigh-Ritz Method

The Rayleigh-Ritz Method is one of the most effective techniques applied to discretization of a continuous system. To obtain an approximate representation of the governing equations, the method assumes a solution of the boundary-value problem that corresponds to a distributed parameter system given by Equation 4.2 [50, 58]. In addition, Lagrange's equation are applied in the derivation process since it is desired to obtain the forced response of the structure. Thus, Lagrange's Equations for a non-conservative system have the form:

$$\frac{d}{dt}\frac{\partial T}{\partial \dot{\phi}_r} - \frac{\partial T}{\partial \phi_r} + \frac{\partial V}{\partial \phi_r} = Q_r(t), \quad r = 1, 2, ..., n. \tag{4.3}$$

Where the kinetic and potential energy can be written as:

$$T(t) = \frac{1}{2}\sum_{i=1}^{n}\sum_{j=1}^{l} m_{i,j}\dot{\phi}_i(t)\dot{\phi}_j(t), \tag{4.4}$$

$$V(t) = \frac{1}{2}\sum_{i=1}^{n}\sum_{j=1}^{l} k_{i,j}\phi_i(t)\phi_j(t), \quad i, j = 1, 2, ..., n. \tag{4.5}$$

Here, $m_{i,j}$ and $k_{i,j}$ represent the mass and stiffness coefficients depending on the distribution of the system and the shape functions $\xi_i(x)$, respectively. The stiffness coefficients $k_{i,j}$ also depend on the derivatives of $\xi_i(x)$ that correspond to half the order of the governing equations of the continuous system. For example, a system with a 4th order PDE in space, it requires up to a second derivative.

Since the structure is subjected to distributed non-conservative forces, the

generalized forces are determined through the implementation of virtual work. This becomes

$$\overline{\delta W}_{nc}(t) = \int_0^\ell f_{aero}(x,t)\delta w(x,t)dx = \int_0^\ell f_{aero}(x,t)\sum_{r=1}^{n}\xi_i(x)\delta\phi_i(t)dx, \tag{4.6}$$

which can also be written as

$$\overline{\delta W}_{nc}(t) = \sum_{r=1}^{n} Q_i(t)\delta\phi_i(t), \tag{4.7}$$

where

$$Q_i(t) = \int_0^\ell f_{aero}(x,t)\xi_r(x)dx, \tag{4.8}$$

defines the generalized non-conservative forces acting on the structure. It can also be observed that the generalized forces are dependent on the shape functions $\xi_i(x)$.

By substituting Equations 4.4, 4.5, and 4.8 into Lagrange's Equations and replacing subscript r by i, the equations of motion become

$$\sum_{j=1}^{n} m_{i,j}\ddot{\phi}_j(t) + \sum_{j=1}^{n} k_{i,j}\phi_j(t) = Q_i(t), \quad i = 1,2,...,n, \tag{4.9}$$

which can also be written in matrix form as

$$[m]\{\ddot{\phi}\} + [k]\{\phi\} = \{Q(t)\}. \tag{4.10}$$

Let us take a closer look at this final expression and notice that it resembles an undamped second order dynamic system with n degrees of freedom. This demonstrates that the Rayleigh-Ritz Method produces the discretized equations of motion from the kinetic energy, potential energy, and virtual work from the external forces.

Nevertheless, it is observed that this method relies heavily on the shape or trial functions. This is because they must fulfill the geometric boundary conditions and represent the deformation of the entire structure [59]. On the other hand, the shape functions are not required to satisfy the natural boundary conditions because they are incorporated into the energy scalar products.

4.2.1.1 Wingletted Wing Discretization

To better illustrate the procedure, consider a wingletted wing that is clamped at the wing root and free at the winglet tip, while the wing and the winglet are rigidly attached at the joint (refer to Figure 2.2). Hence, from Section 3.2.2.1, the displacement for the wing and winglet sections are given by:

$$w_1(x,t) = H_1(x,t) - d_{cm}\Phi_1(x,t), \tag{4.11}$$

$$\begin{aligned} w_2(x,t) &= \ell_1 + \varepsilon_2(x)\cos(\gamma) + \varepsilon_2(x)\sin(\gamma) + H_1(\ell_1) - d_{cm}\Phi_1(\ell_1) \\ &+ \big(H_2(x) - d_{cm}\Phi_2(x)\big)\cos(\gamma) - \big(H_2(x) - d_{cm}\Phi_2(x)\big)\sin(\gamma) \\ &+ \Big(\varepsilon_2(x)\sin(\gamma) + \big(h_2(x) - d_{cm}\varphi_2(x)\big)\cos(\gamma)\Big)\varphi_1(\ell_1) + d_{cm}. \end{aligned} \tag{4.12}$$

Note that Equation 4.11 only describes the out-of-plane deformation of the

wing section, while Equation 4.12 represents the in-plane displacement and out-of-plane deformation of the winglet panel. In addition, this equation contain the non-linear terms that describe the interaction of the wing and winglet panels. The approximate displacements in bending $H_p(x,t)$ and torsion $\Phi_p(x,t)$ of the continuous system are given as follows

$$H_p(x,t) = \sum_{i=1}^{n} \xi_{h_i}(x) h_i(t), \tag{4.13}$$

$$\Phi_p(x,t) = \sum_{j=1}^{l} \xi_{\varphi_j}(x) \varphi_j(t), \quad p = 1, 2. \tag{4.14}$$

The subscript p denotes the number of sections that the wingletted wing structure has been divided into, which in this case is two. The generalized coordinates associated to bending and torsion for the wing and winglet sections are $h_i(t)$ and $\varphi_j(t)$, respectively. Moreover, $\xi_{h_i}(x)$ and $\xi_{\varphi_j}(x)$ are the orthogonal or linearly independent mode shapes describing a cantilever beam in pure bending and torsion. In order to fulfill those conditions, the eigen-functions are used as the shape functions in this analysis, which are given by

$$\xi_{h_i}(x) = B\big(\sinh(\lambda_h \eta) - \sin(\lambda_h \eta)\big) - \cosh(\lambda_h \eta) + \cos(\lambda_h \eta), \tag{4.15}$$

$$\xi_{\varphi_i}(x) = \sin(\lambda_\varphi \eta), \tag{4.16}$$

where $B = \frac{\big(\cosh(\lambda_h)+\cos(\lambda_h)\big)}{\big(\sinh(\lambda_h)+\sin(\lambda_h)\big)}$ and $\eta = \frac{x}{\ell}$.

The substitution of Equations 4.11 and 4.12 into Equation 4.4 leads to the

total kinetic energy of the system,

$$T_{total}(t) = \frac{1}{2}\int_0^{\ell_1} m_1(x)\dot{w}_1^2(x,t)dx + \frac{1}{2}\int_0^{\ell_2} m_2(x)\dot{w}_2^2(x,t)dx, \tag{4.17}$$

$$= \frac{1}{2}\left(\sum_{i=1}^{n}\sum_{j=1}^{l} m_{1_{i,j}}\dot{\phi}_i(t)\dot{\phi}_j(t) + \sum_{i=1}^{n}\sum_{j=1}^{l} m_{2_{i,j}}\dot{\phi}_i(t)\dot{\phi}_j(t)\right), \tag{4.18}$$

so that the mass matrix coefficients are

$$m_{p_{i,j}} = \int_0^{\ell_p} m_p(x)\xi_i(x)\xi_j(x)dx \quad i,j = 1,2,...,n, \tag{4.19}$$

where ξ_h and ξ_φ are substituted accordingly.

On the other hand, the total potential energy of the system results from the elastic deformation of the inboard and outboard wing sections, such that

$$V_{total}(t) = \sum_{p=1}^{2} V_p(t), \tag{4.20}$$

where

$$V_p(t) = \frac{1}{2}\left(\int_0^{\ell_1} EI_p(x)\left[\frac{\partial^2 h_p(x,t)}{\partial x^2}\right]^2 dx + \int_0^{\ell_1} GJ_p(x)\left[\frac{\partial \varphi_p(x,t)}{\partial x}\right]^2 dx\right) \tag{4.21}$$

$$= \frac{1}{2}\left(\sum_{i=1}^{n}\sum_{j=1}^{l} EI_{p_{i,j}}(x)h_i(t)h_j(t) + \sum_{i=1}^{n}\sum_{j=1}^{l} GJ_{p_{i,j}}(x)\varphi_i(t)\varphi_j(t)\right), \quad i,j = 1,2,...,n. \tag{4.22}$$

Thus, the structural stiffness matrix coefficients of the system become

$$k_{p_{i,j}} = \int_0^{\ell_p} EI_p(x)\frac{d^2\xi_{h_i}(x)}{dx^2}\frac{d^2\xi_{h_j}(x)}{dx^2}dx + \int_0^{\ell_p} GJ_p(x)\frac{d\xi_{\varphi_i}(x)}{dx}\frac{d\xi_{\varphi_j}(x)}{dx}dx, \quad i,j = 1,2,...,n. \tag{4.23}$$

The generalized aerodynamic forces can be identified through the application of our definition of virtual work. Hence, it takes the form

$$\overline{\delta W}_{nc_{total}}(t) = \sum_{p=1}^{2} Q_{h_p}(t)\delta h_p(t) + \sum_{p=1}^{2} Q_{\varphi_p}(t)\delta\varphi_p(t), \tag{4.24}$$

where $Q_{h_p}(t)$ and $Q_{\varphi_p}(t)$ are

$$Q_{h_1}(t) = \int_0^{\ell} L_1(x,t)\xi_{h_i}(x)dx, \tag{4.25}$$

$$Q_{\varphi_1}(t) = \int_0^{\ell} M_{a_1}(x,t)\xi_{\varphi_i}(x)dx, \tag{4.26}$$

$$Q_{h_2}(t) = \int_0^{\ell} L_2(x,t)\Big(\xi_{h_i}(\ell_1)\cos(\gamma) + \xi_{h_i}(x)\Big)dx, \tag{4.27}$$

$$Q_{\varphi_2}(t) = \int_0^{\ell} M_{a_2}(x,t)\Big(\xi_{\varphi_i}(\ell_1)\cos(\gamma) + \xi_{\varphi_i}(x)\Big)dx. \tag{4.28}$$

From the previous equations, $L_p(x,t)$ and M_{a_p} are the general expressions for the aerodynamic lift and moment, which can be substituted by any of our aerodynamic flow models previously discussed. This will produce the aerodynamic stiffness, aerodynamic damping, and virtual mass matrices.

Now, let us combine Equations 4.19, 4.23, and 4.24 to obtain an algebraic set

of governing equations that can be written in the following matrix form

$$[m_s - m_{aero}]\{\ddot{\phi}\} + [c_{aero}]\{\dot{\phi}\} + [k_s - k_{aero}]\{\phi\} = 0. \tag{4.29}$$

4.2.2 Finite Element Method

This section introduces the application of the Finite Element Method (FEM), which is a powerful method for analyzing complex structures. Consider the beam presented in Figure 4.1, where it is divided into a series of elements. The deformation of each element is described by linear mapping functions that account for the rotations and displacements at each node.

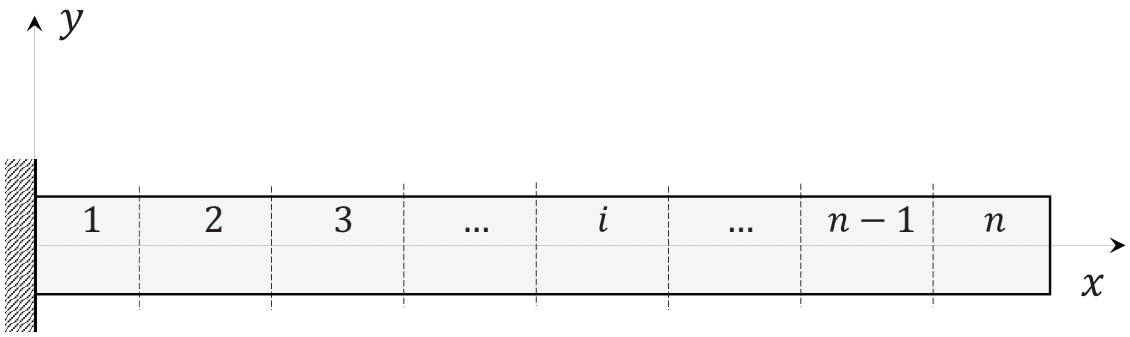

Fig. 4.1: Uniform beam discretized into n elements of equal length.

4.2.2.1 Planar Wing Element

To illustrate the discretization process via FEM, consider a straight, planar, and uniform high aspect ratio wing as depicted in Figure 4.2, where the reference axis x is assumed to be the elastic axis. Also, the inertial axis is separated by a distance d_{cm} from the elastic axis. Each beam-like element is allowed to undergo

out-of-plane deformation due to flexural translation $h(x,t)$ and torsional rotation $\varphi(x,t)$ [4, 60]. Thus, each wing element has six degrees of freedom representing the transverse displacements, angular displacements, and slopes at the ends. Let ϕ_1 and ϕ_4 represent the transverse displacement at the left and right sides of the element, ϕ_2 and ϕ_5 define the slope at either side of the element, and the angular displacement at either side of the element is given by ϕ_3 and ϕ_6.

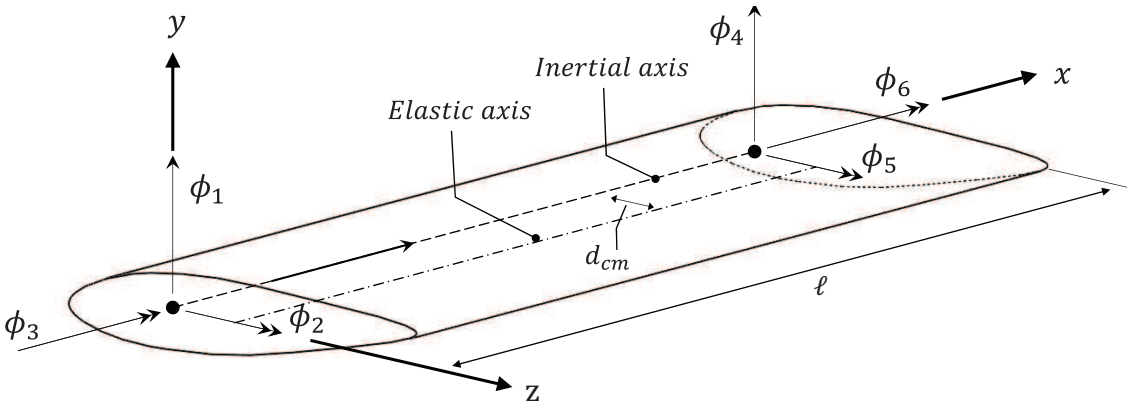

Fig. 4.2: Schematic of a two-node beam-like wing element of length ℓ. Each node shows three degrees of freedom, which are associated to bending and torsion.

From kinematics, the out-of-plane displacement of a wing element between 0 and ℓ_i is defined as:

$$\begin{aligned} w(x,t) &= h(x,t) - d_{cm}\varphi(x,t) \\ &= \sum_{b=1}^{n} H_b(x)\phi_b(t) - d_{cm}\sum_{\tau=1}^{n}\Phi_\tau(x)\phi_\tau, \\ &= \sum_{i=1}^{6}\Psi_i(x)\phi_i(t). \end{aligned} \tag{4.30}$$

From our current formulation, $\phi_i(t) = [\phi_b, \phi_\tau]^T$ is the nodal displacement at either end of each beam element. Also, $\Psi_r(x)$ denotes a set of interpolation functions for bending $H_b(x)$ and torsional $\Phi_\tau(x)$ displacement. This functions must satisfy the following boundary conditions

$$\begin{aligned}
H_1(0) = \Psi_1(0) = \phi_1, \qquad & H_4(\ell) = \Psi_4(\ell) = \phi_4, \quad \text{(transverse displacement)} \\
\frac{\partial H_2}{\partial x}(0) = \frac{\partial \Psi_2}{\partial x}(0) = \phi_2, \quad & \frac{\partial H_5}{\partial x}(\ell) = \frac{\partial \Psi_5}{\partial x}(\ell) = \phi_5, \quad \text{(slope)} \\
\Phi_3(0) = \Psi_3(0) = \phi_3, \qquad & \Phi_6(\ell) = \Psi_6(\ell) = \phi_6. \quad \text{(angular displacement)}
\end{aligned} \tag{4.31}$$

The deflection of a beam-like element under a transverse distributed load is described by a cubic function, whereas the angular deformation of an element undergoing torsion is defined by a linear function [58]. These functions are the following

$$h(x,t) = C_1 + C_2\frac{x}{\ell} + C_4\left(\frac{x}{\ell}\right)^2 + C_5\left(\frac{x}{\ell}\right)^3, \tag{4.32}$$

$$\varphi(x,t) = C_3 + C_6\frac{x}{\ell}. \tag{4.33}$$

In both equations the coordinate along the beam length is normalized by ℓ, and C_i $(i = 1, 2, ..., 6)$ are constants of integration [4]. Let us substitute Equation 4.31 into Equations 4.32 and 4.33 to define the interpolation functions for transverse and angular displacement

$$\Psi_b = \begin{cases} \Psi_1(x) = 1 - 3\Big(\frac{x}{\ell}\Big)^2 + 2\Big(\frac{x}{\ell}\Big)^3, \\ \Psi_2(x) = x - 2\ell\Big(\frac{x}{\ell}\Big)^2 + \ell\Big(\frac{x}{\ell}\Big)^3, \\ \Psi_4(x) = 3\Big(\frac{x}{\ell}\Big)^2 - 2\Big(\frac{x}{\ell}\Big)^3, \\ \Psi_5(x) = -\ell\Big(\frac{x}{\ell}\Big)^2 + \ell\Big(\frac{x}{\ell}\Big)^3, \end{cases} \tag{4.34}$$

$$\Psi_\tau = \begin{cases} \Psi_3(x) = 1 - \dfrac{x}{\ell}, \\ \Psi_6(x) = \dfrac{x}{\ell}. \end{cases} \tag{4.35}$$

The formulation of the element mass and stiffness matrices requires an expression for the kinetic and potential energy. From reference [60], for a beam element undergoing out-of-plane deformation, the kinetic and potential energy equations are given by

$$\begin{aligned} T &= \frac{1}{2}\Big[\int_0^\ell m(\dot{\mathrm{w}}_b^T\dot{\mathrm{w}}_b)dx - \int_0^\ell S_\varphi(\dot{\mathrm{w}}_b^T\dot{\mathrm{w}}_\varphi + \dot{\mathrm{w}}_\varphi^T\dot{\mathrm{w}}_b)dx + \int_0^\ell I_\varphi(\dot{\mathrm{w}}_\varphi^T\dot{\mathrm{w}}_\varphi)dx\Big], \\ &= \frac{1}{2}\dot{\phi}^T[\bar{m}_e]\dot{\phi}, \end{aligned} \tag{4.36}$$

$$\begin{aligned} V &= \frac{1}{2}\Big[\int_0^\ell EI(\mathrm{w}''^T_b\mathrm{w}''_b)dx + \int_0^\ell GJ(\mathrm{w}'^T_\tau\mathrm{w}'_\tau)dx\Big], \\ &= \frac{1}{2}\phi^T[\bar{k}_e]\phi \end{aligned} \tag{4.37}$$

where $\mathrm{w}_b = \Psi_b^T\{\hat{\phi}_b\}$, $\mathrm{w}_\tau = \Psi_\tau^T\{\hat{\phi}_\tau\}$, and $\phi = [\phi_1, \phi_2, \phi_3, \phi_4, \phi_5, \phi_6]^T$; and the local

element mass $[\bar{m}_e]$ and stiffness $[\bar{k}_e]$ matrices become

$$\bar{m}_e = \begin{bmatrix} 156a & 22\ell a & -7b/2 & 54a & -13\ell a & -3b/2 \\ 22\ell a & 4\ell^2 a & -\ell b/2 & 13\ell a & -3\ell^2 a & \ell b/3 \\ -7b/2 & -\ell b/2 & 2c & -3b/2 & \ell b/3 & c \\ 54a & 13\ell a & -3b/2 & 156a & -22\ell a & -7b/2 \\ -13\ell a & -3\ell^2 a & \ell b/3 & -22\ell a & 4\ell^2 a & \ell b/2 \\ -3b/2 & \ell b/3 & c & -7b/2 & \ell b/2 & 2c \end{bmatrix}, \tag{4.38}$$

$$\bar{k}_e = \frac{EI}{\ell^3} \begin{bmatrix} 12 & 6\ell & 0 & -12 & 6\ell & 0 \\ 6\ell & 4\ell^2 & 0 & -6\ell & 2\ell^2 & 0 \\ 0 & 0 & (GJ/EI)\ell^2 & 0 & 0 & -(GJ/EI)\ell^2 \\ -12 & -6\ell & 0 & 12 & -6\ell & 0 \\ 6\ell & 2\ell^2 & 0 & -6\ell & 4\ell^2 & 0 \\ 0 & 0 & -(GJ/EI)\ell^2 & 0 & 0 & (GJ/EI)\ell^2 \end{bmatrix} \tag{4.39}$$

where

$$a = \frac{m\ell}{420}, \quad b = \frac{S_\varphi}{10}, \text{ and } c = \frac{I_\varphi \ell}{6}.$$

Finally, one can include the external aerodynamic forces and moments acting on the system by expressing the aerodynamic models in terms of the heave and pitch displacement of the structure. To do this, let us consider potential flow over a 2D wing that is assumed to contain a single vortex component as it is sketched in

Figure 4.3. This vortex is located at a 1/4 chord of the wing, which is superimposed upon a uniform flow. Moreover, the zero normal flow boundary condition is enforced through a control point placed at 3/4 chord. The application of these constraints upholds the Kutta condition and allows us to model the 2D wing as a single element [4, 44]. As a result, these considerations allow us to express the lift per unit span as a function of the vortex strength Γ

$$L = \rho U \Gamma. \tag{4.40}$$

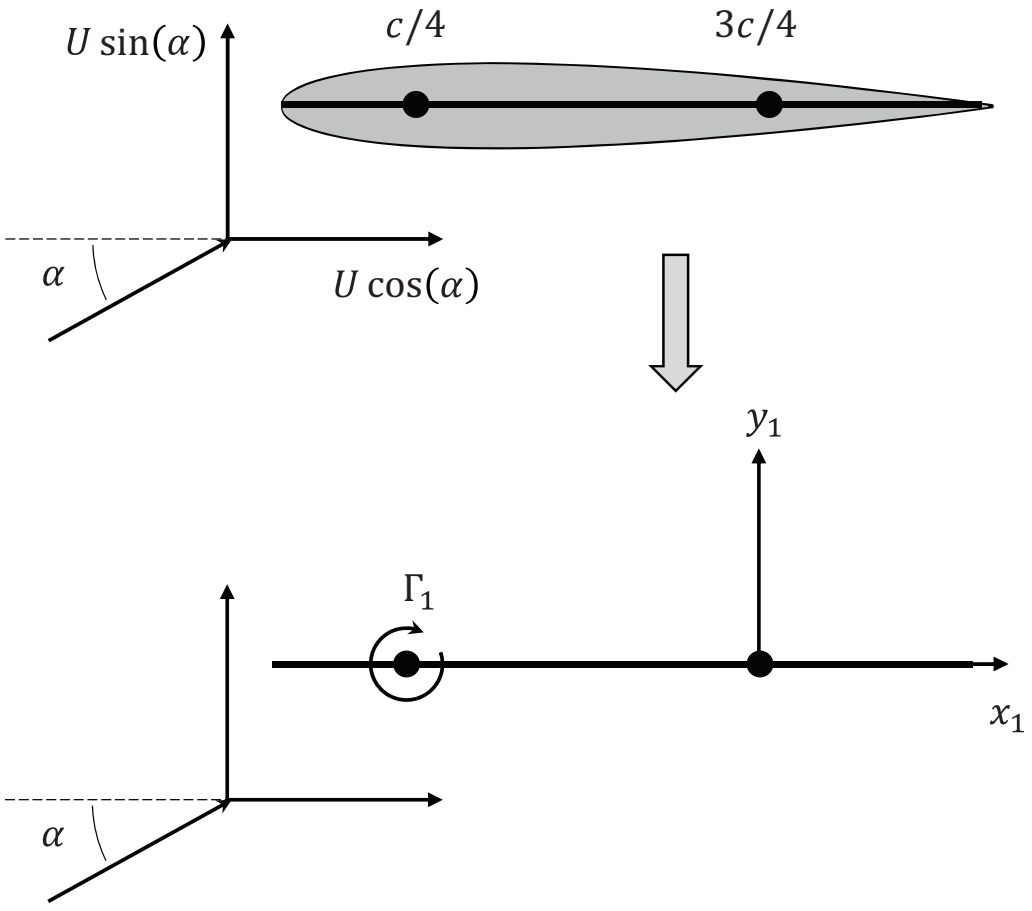

Fig. 4.3: Single vortex representation on a 2D airfoil.

Now, with the vertical component of the flow at the control point being zero, the downwash contributions from the vortex must be equal magnitude and opposite sign to that of the freestream. It can be shown that the unknown vortex strength can be expressed as

$$\Gamma = U\alpha c\pi, \tag{4.41}$$

and Equation 4.40 can be reformulated as

$$L = \rho U\Gamma = \rho U \times U\alpha c\pi = \frac{1}{2}U^2 2\pi c\alpha, \tag{4.42}$$

which agrees with our definition for the lift force obtained from Strip Theory for the steady flow model (see Equation 3.40).

By considering a finite wing that is divided into multiple spanwise stations, Equation 4.40 can be rewritten to express the force vector as follows

$$F_{aero_e} = \rho U \boldsymbol{S}\Gamma \tag{4.43}$$

$$= -\rho U^2 \boldsymbol{\mathcal{T}}_2 \boldsymbol{S}\boldsymbol{\Xi}^{-1}\boldsymbol{\mathcal{T}}_1(r + r_0). \tag{4.44}$$

More details about this equation can be found in Reference [4]. In this equation, $\boldsymbol{S}$ represents a diagonal matrix that contains the span of each panel or element; $\boldsymbol{\mathcal{T}}_1$ is a transformation matrix that associates the angle of attack of each panel to the structural degrees of freedom. Then, $\boldsymbol{\mathcal{T}}_2$ is another transformation matrix that maps the distribution of the aerodynamic forces and moments into the structural model. Both transformation matrices ensure proper distribution of the aerodynamic loads

on the structure. The influence coefficient that define the normal flow at the control point from the vortex strength are contained in the $\boldsymbol{\Xi}$ matrix, while $(r + r_o)$ are the deformed and undeformed position vectors for the bending and torsion modes. However, r_o is ignored since the focus of this work is the flutter solution. Thus, for a wing element the aerodynamic forces and moments are:

$$F_{aero_e} = \pi\rho U^2 sb \begin{bmatrix} 0 & 0 & 1/2 & 0 & 0 & 1/2 \\ 0 & 0 & \ell/12 & 0 & 0 & \ell/12 \\ 0 & 0 & e/2 & 0 & 0 & e/2 \\ 0 & 0 & 1/2 & 0 & 0 & 1/2 \\ 0 & 0 & -\ell/12 & 0 & 0 & -\ell/12 \\ 0 & 0 & e/2 & 0 & 0 & e/2 \end{bmatrix} \begin{Bmatrix} \phi_1 \\ \phi_2 \\ \phi_3 \\ \phi_4 \\ \phi_5 \\ \phi_6 \end{Bmatrix} \tag{4.45}$$

One can note that Equation 4.45 constitutes the aerodynamic stiffness, and it is dependent on the forward speed. Then, one can invoke the quasi-steady and unsteady flow models and follow the same procedure to formulate the remaining aerodynamic matrices.

4.2.2.2 Three-Dimensional Wing Element

Thus far, the element mass, stiffness, and external force matrices represent those of a planar wing. However, for a wingletted wing with a variable cant angle winglet, one needs to divide the structure into a series of three-dimensional frame elements in order to model transverse shear forces, moments, and axial forces. This

representation produces an element that has twelve degrees of freedom, which are associated to displacements along the x, y, and z axes and rotations about those axes [59]. From Figure 4.4, let us define ϕ_1 and ϕ_7 as the axial displacement due to elongation at both ends of the frame element. The degrees of freedom associated to bending in the $x-y$ plane are ϕ_2, ϕ_6, ϕ_8, and ϕ_{12}, while ϕ_3, ϕ_5, ϕ_9, and ϕ_{11} represent the degrees of freedom for bending in the $x-z$ plane. Finally, the angular displacement in torsion at either side of the element is given by ϕ_4 and ϕ_10.

The frame element mass and stiffness matrices associated to the 12-degree-of-freedom frame element presented in Figure 4.4 are formulated in the same fashion as the ones for a wing without a winglet. Thus, using the formulation for potential and kinetic energy leads to Equations 4.46 and 4.47, which define the stiffness and mass coefficients of the three-dimensional element that is coupled in bending and torsion. In addition, the process of mapping the aerodynamic forces and moments onto the structural model is similar to the one for a planar element, which leads to Equation 4.48. As one can see, the difference is the additional degrees of freedom associated to the three-dimensional wing element.

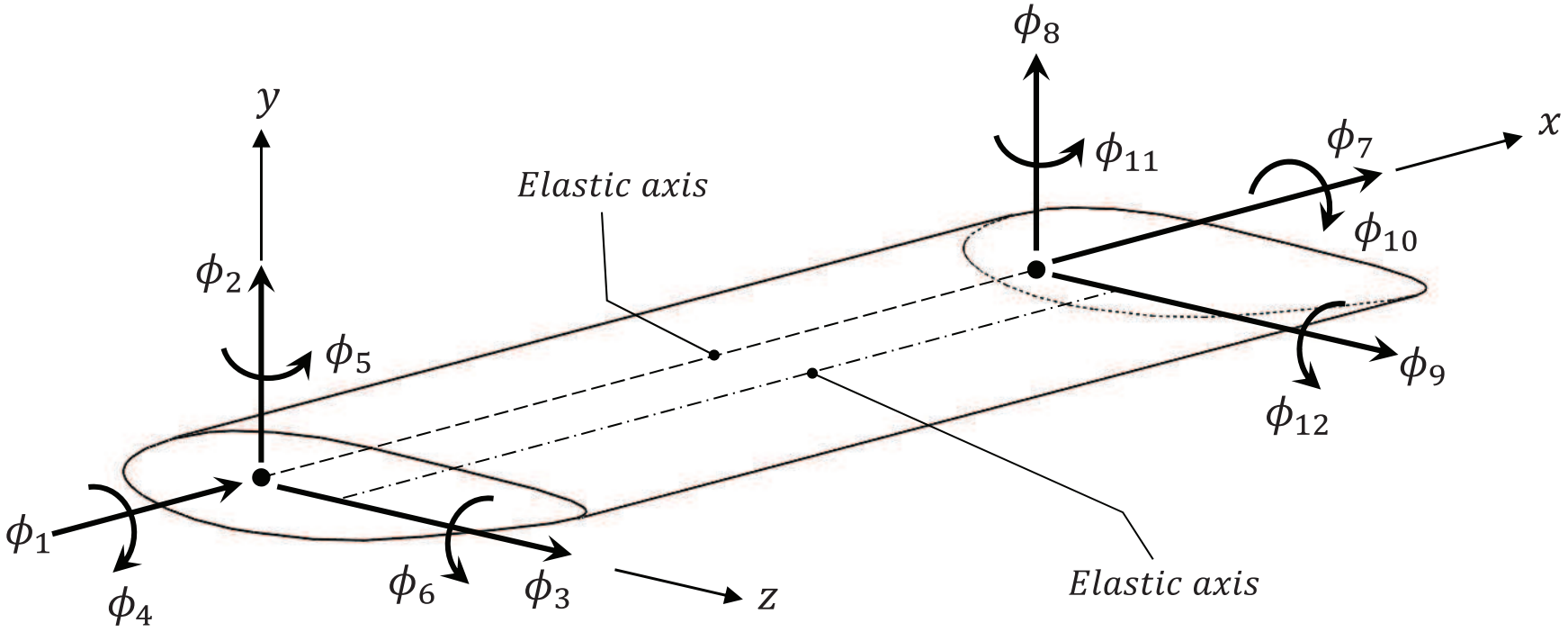

Fig. 4.4: Schematic of a two-node beam-like wing frame element of length ℓ in the global frame. Each node presents six degrees of freedom, which are associated to bending, torsion, and elongation. They describe three displacements and three rotations at each node.

$$\bar{m}_e = \begin{bmatrix} 2d & 0 & 0 & 0 & 0 & 0 & d & 0 & 0 & 0 & 0 & 0 \\ 0 & 156a & 0 & -7b/2 & 0 & 22\ell a & 0 & 54a & 0 & -3b/2 & 0 & -13\ell a \\ 0 & 0 & 156a & 0 & 22\ell a & 0 & 0 & 0 & 54a & 0 & -13\ell a & 0 \\ 0 & -7b/2 & 0 & 2c & 0 & -\ell b/2 & 0 & -3b/2 & 0 & c & 0 & \ell b/3 \\ 0 & 0 & -22\ell a & 0 & 4\ell^2 a & 0 & 0 & 0 & -13\ell a & 0 & -3\ell^2 a & 0 \\ 0 & 22\ell a & 0 & -\ell b/2 & 0 & 4\ell^2 a & 0 & 13\ell a & 0 & \ell b/3 & 0 & -3\ell^2 a \\ d & 0 & 0 & 0 & 0 & 0 & 2d & 0 & 0 & 0 & 0 & 0 \\ 0 & 54a & 0 & -3b/2 & 0 & 13\ell a & 0 & 156a & 0 & -7b/2 & 0 & 22\ell a \\ 0 & 0 & 54a & 0 & -13\ell a & 0 & 0 & 0 & 156a & 0 & 22\ell a & 0 \\ 0 & -3b/2 & 0 & c & 0 & \ell b/3 & 0 & -7b/2 & 0 & 2c & 0 & \ell b/2 \\ 0 & 0 & 13\ell a & 0 & -3\ell^2 a & 0 & 0 & 0 & 22\ell a & 0 & 4\ell^2 a & 0 \\ 0 & -13\ell a & 0 & \ell b/3 & 0 & -3\ell^2 a & 0 & -22\ell a & 0 & \ell b/2 & 0 & 4\ell^2 a \end{bmatrix}, \tag{4.46}$$

$$\bar{k}_e = \begin{bmatrix} \frac{EA}{\ell} & 0 & 0 & 0 & 0 & 0 & \frac{-EA}{\ell} & 0 & 0 & 0 & 0 & 0 \\ 0 & \frac{12EI_z}{\ell^3} & 0 & 0 & 0 & \frac{6EI_z}{\ell^2} & 0 & \frac{-12EI_z}{\ell^3} & 0 & 0 & 0 & \frac{6EI_z}{\ell^2} \\ 0 & 0 & \frac{12EI_y}{\ell^3} & 0 & \frac{-6EI_y}{\ell^2} & 0 & 0 & 0 & \frac{-12EI_y}{\ell^3} & 0 & \frac{-6EI_y}{\ell^2} & 0 \\ 0 & 0 & 0 & \frac{GJ}{\ell} & 0 & 0 & 0 & 0 & 0 & \frac{-GJ}{\ell} & 0 & 0 \\ 0 & 0 & \frac{-6EI_y}{\ell^2} & 0 & \frac{4EI_y}{\ell} & 0 & 0 & 0 & \frac{6EI_y}{\ell^2} & 0 & \frac{2EI_y}{\ell} & 0 \\ 0 & \frac{6EI_z}{\ell^2} & 0 & 0 & 0 & \frac{4EI_z}{\ell} & 0 & \frac{-6EI_z}{\ell^2} & 0 & 0 & 0 & \frac{2EI_z}{\ell} \\ \frac{-EA}{\ell} & 0 & 0 & 0 & 0 & 0 & \frac{EA}{\ell} & 0 & 0 & 0 & 0 & 0 \\ 0 & \frac{-12EI_z}{\ell^3} & 0 & 0 & 0 & \frac{-6EI_z}{\ell^2} & 0 & \frac{12EI_z}{\ell^3} & 0 & 0 & 0 & \frac{-6EI_z}{\ell^2} \\ 0 & 0 & \frac{-12EI_y}{\ell^3} & 0 & \frac{6EI_y}{\ell^2} & 0 & 0 & 0 & \frac{12EI_y}{\ell^3} & 0 & \frac{6EI_y}{\ell^2} & 0 \\ 0 & 0 & 0 & \frac{-GJ}{\ell} & 0 & 0 & 0 & 0 & 0 & \frac{GJ}{\ell} & 0 & 0 \\ 0 & 0 & \frac{-6EI_y}{\ell^2} & 0 & \frac{2EI_y}{\ell} & 0 & 0 & 0 & \frac{6EI_y}{\ell^2} & 0 & \frac{4EI_y}{\ell} & 0 \\ 0 & \frac{6EI_z}{\ell^2} & 0 & 0 & 0 & \frac{2EI_y}{\ell} & 0 & \frac{-6EI_z}{\ell^2} & 0 & 0 & 0 & \frac{4EI_z}{\ell} \end{bmatrix}, \tag{4.47}$$

where

$$a = \frac{m\ell}{420}, \quad b = \frac{S_\varphi}{10}, \quad c = \frac{I_\varphi \ell}{6}, \text{ and } d = \frac{m\ell}{6}.$$

$$\bar{F}_{aero_e} = \pi\rho U^2 sb \begin{bmatrix} 0 & 0 & 0 & 0 & 0 & 0 & 0 & 0 & 0 & 0 & 0 \\ 0 & 0 & 0 & 1/2 & 0 & 0 & 0 & 0 & 1/2 & 0 & 0 \\ 0 & 0 & 0 & 0 & 0 & 0 & 0 & 0 & 0 & 0 & 0 \\ 0 & 0 & 0 & e/2 & 0 & 0 & 0 & 0 & e/2 & 0 & 0 \\ 0 & 0 & 0 & 0 & 0 & 0 & 0 & 0 & 0 & 0 & 0 \\ 0 & 0 & 0 & \ell/12 & 0 & 0 & 0 & 0 & \ell/12 & 0 & 0 \\ 0 & 0 & 0 & 0 & 0 & 0 & 0 & 0 & 0 & 0 & 0 \\ 0 & 0 & 0 & 1/2 & 0 & 0 & 0 & 0 & 1/2 & 0 & 0 \\ 0 & 0 & 0 & 0 & 0 & 0 & 0 & 0 & 0 & 0 & 0 \\ 0 & 0 & 0 & e/2 & 0 & 0 & 0 & 0 & e/2 & 0 & 0 \\ 0 & 0 & 0 & 0 & 0 & 0 & 0 & 0 & 0 & 0 & 0 \\ 0 & 0 & 0 & -\ell/12 & 0 & 0 & 0 & 0 & -\ell/12 & 0 & 0 \end{bmatrix} \begin{Bmatrix} \phi_1 \\ \phi_2 \\ \phi_3 \\ \phi_4 \\ \phi_5 \\ \phi_6 \\ \phi_7 \\ \phi_8 \\ \phi_9 \\ \phi_{10} \\ \phi_{11} \\ \phi_{12} \end{Bmatrix} \tag{4.48}$$

Now, to account for the cant angle, let us refer Figure 4.5 and consider a frame element located in the winglet panel that is rotated by some angle γ, which represents the orientation of the element's local reference frame. From kinematics, one can apply a transformation matrix to express the deformation of this element with respect to the global reference frame [59]. Therefore, the displacement trans-

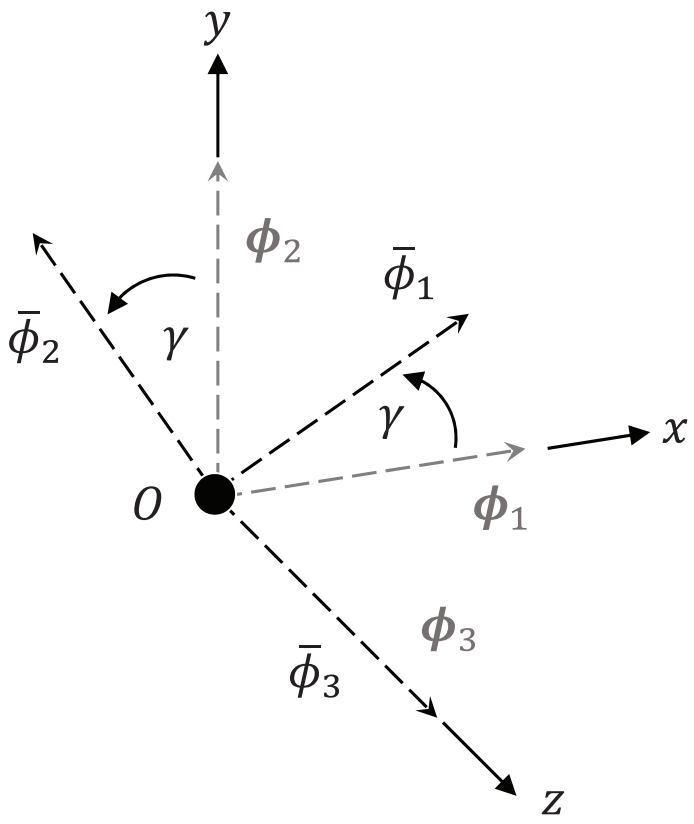

Fig. 4.5: Local frame rotation by angle γ.

formation matrix at each end of the element is given by

$$\mathcal{T} = \begin{bmatrix} \cos(\gamma) & \sin(\gamma) & 0 & 0 & 0 & 0 \\ -\sin(\gamma) & \cos(\gamma) & 0 & 0 & 0 & 0 \\ 0 & 0 & 1 & 0 & 0 & 0 \\ 0 & 0 & 0 & \cos(\gamma) & \sin(\gamma) & 0 \\ 0 & 0 & 0 & -\sin(\gamma) & \cos(\gamma) & 0 \\ 0 & 0 & 0 & 0 & 0 & 1 \end{bmatrix} \tag{4.49}$$

With the transformation matrix $\mathcal{T}$ already defined, the transformation process

to the global coordinate system is fairly simple. To obtain the transformation equations, one can recall the equations that define the kinetic and potential energy of the wing elements (Eqs. 4.36 and 4.37), where one can substitute the transformation equation as follows

$$T = \frac{1}{2}\dot{\phi}^T[\bar{m}_e]\dot{\phi} = \frac{1}{2}\dot{\tilde{\phi}}^T[\tilde{m}_e]\dot{\tilde{\phi}} \tag{4.50}$$

$$V = \frac{1}{2}\phi^T[\bar{k}_e]\phi = \frac{1}{2}\tilde{\phi}^T[\tilde{k}_e]\tilde{\phi} \tag{4.51}$$

In both equations, $\tilde{\phi}$ denotes the nodal displacement in the local coordinate system. One can write the frame element mass $[\tilde{m}_e]$ and stiffness $[\tilde{k}_e]$ matrices in the global frame as follow

$$\tilde{m}_e = \mathcal{T}[\bar{m}_e]\mathcal{T} \tag{4.52}$$

$$\tilde{k}_e = \mathcal{T}[\bar{k}_e]\mathcal{T} \tag{4.53}$$

where $[\bar{m}_e]$ and $[\bar{k}_e]$ are the mass and stiffness matrices of the three-dimensional element in the local frame. Similarly, the aerodynamic forces can be written as

$$\tilde{F}_{aero_e} = \mathcal{T}[\bar{F}_{aero_e}]\mathcal{T} \tag{4.54}$$

Finally, after defining $[\bar{m}_e]$, $[\bar{k}_e]$, and $[\bar{F}_{aero_e}]$, one can begin the assembly process of the individual frame elements to formulate the *mass, stiffness,* and *aerodynamic force global matrices* for the dynamic system. This yields the following

equations

$$[M_s - M_{aero}]\{\ddot{\phi}\} + [C_{aero}]\{\dot{\phi}\} + [K_s - K_{aero}]\{\phi\} = \{0\}, \quad (4.55)$$

$$[M_{eq}]\{\ddot{\phi}\} + [C_{aero}]\{\dot{\phi}\} + [K_{eq}]\{\phi\} = \{0\}, \quad (4.56)$$

where $[M_s]$ and $[M_{aero}]$ are the structural and virtual mass matrices, respectively. The aerodynamic damping terms are represented by the $[C_{aero}]$ matrix. The structural and aerodynamic stiffness matrices are denoted by $[K_s]$ and $[K_{aero}]$, respectively. The entries for the aerodynamic damping and virtual mass matrices will change based on the aerodynamic model applied, but the generalized form of these equations will not change. The difference between the structural and virtual mass is referred to as the equivalent mass matrix $[M_{eq}]$. Similarly, the equivalent stiffness matrix is given by $[K_{eq}]$.

4.3 Flutter Speed Prediction Approach

Thus far, each discretization method has lead to a set of second order ordinary differential equations that can be used to approximate the flutter speed. To accomplish this, one can follow the standard procedure for a free vibration system analysis that leads to the eigenvalue problem.

$$\lambda\{p\} = [A]\{p\}, \quad (4.57)$$

where λ denotes the system's eigenvalues, $\{p\}$ represents the corresponding eigenvectors, and $[A]$ is the state matrix defined as

$$A = \begin{bmatrix} 0 & I \\ -[K_{eq}]/[M_{eq}] & -[C_{aero}]/[M_{eq}] \end{bmatrix}. \tag{4.58}$$

From Equation 4.58, one can observe that matrix A is dependent on the flight speed U. Consequently, it is possible to use this expression to obtain the stability boundaries of the system and determine the flutter speed U_f. The solution process is outlined in Figure 4.6. The process begins by defining the wing configuration. This is done by selecting the wing geometry (wing span and chord length), cant angle, and inertial and elastic properties. Then, one needs to select the flight condition at which the system will be analyzed, altitude and air density. Once the flight condition is defined, it is necessary to provide the incoming flow speed U. With all the parameters that constitute the A matrix already defined, it is time to compute the non-trivial solution that leads to the eigenvalues $\lambda_j = \sigma_j \pm i\omega_j$. One can now associate the eigenvalues to the incoming flow speed and observe the aeroelastic response of the system. Also, one can determine the instability point checked if $Re(\lambda)$ becomes positive. If the instability point is not found at the given speed, it is required to increase the incoming flow speed and compute the eigenvalues again until a flutter speed is found.

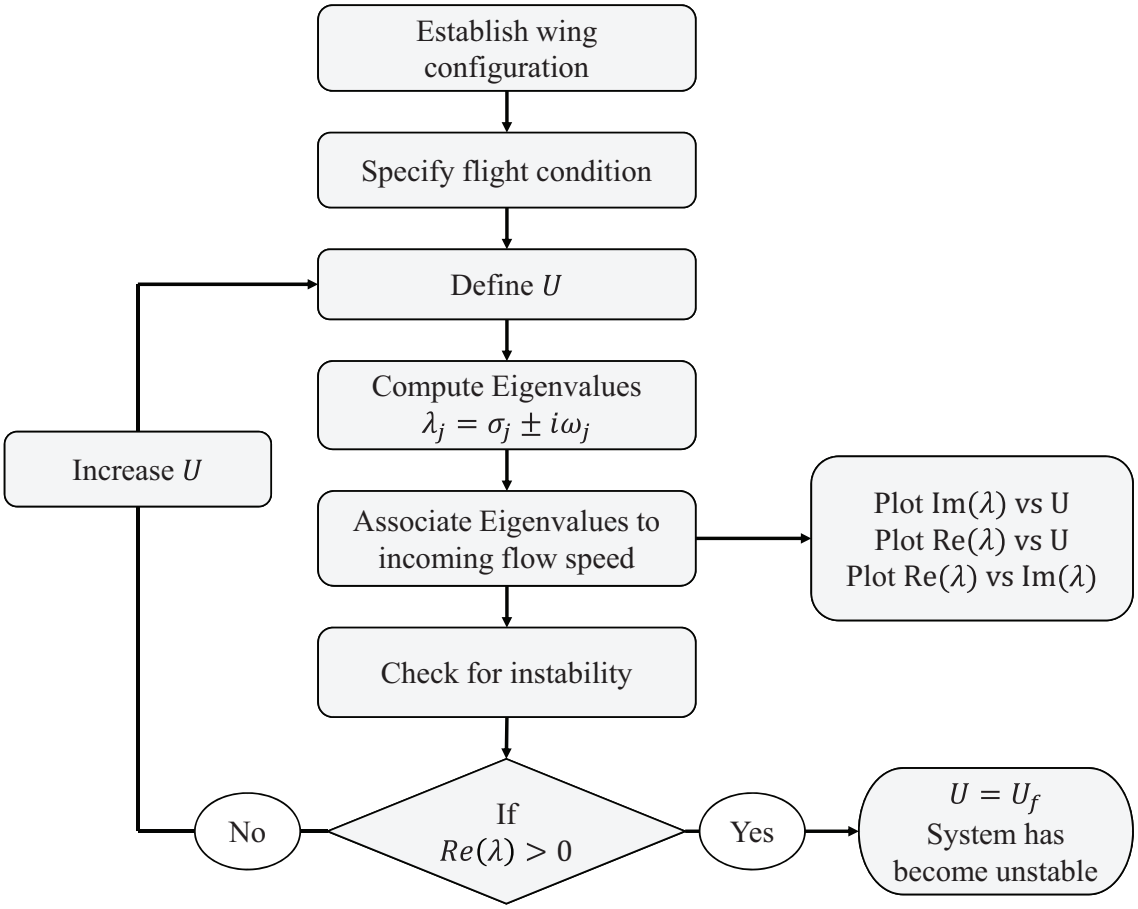

Fig. 4.6: Iteration process to determine flutter boundaries via eigenvalue solution.

4.4 Chapter Summary

This chapter described the application of the Rayleigh-Ritz Method and Finite Element Method to derive the governing equations of the wingletted wing, which is an n-degree-of-freedom system. These methods allowed an approximation of the dynamic behavior of the system through the application of energy principles.

The discretized equations of motion were manipulated to formulate the eigen-

value problem. Once formulated, it was possible to establish a mathematical process to estimate the flutter speed. This iterative procedure will be used in the following chapter to determine the flutter condition and understand the aeroelastic response of the system before and after the flutter condition has been determined.

Chapter 5: Flutter Analysis Results

5.1 Overview

Until this point, the discussion has focused on the derivation of the continuous and discrete equations of motion for the wingletted wing system and the iterative process to determine the flutter speed via eigenvalue problem solution. Now, we present the results from the aeroelastic analysis of various wing configurations. The wing geometries employed in this analysis contain the same properties that Martin Goland used in his study from 1945 [12]. The length of the outer wing panel was varied with respect to the length of the inboard wing panel, ℓ_2/ℓ_1. The aeroelastic results from both structural discretization methods along with all three aerodynamic models were compared to a reference planar wing, i.e. wing without a winglet. This was done to compare the results from each method. After that, the models were used to provide a detailed explanation of the flutter mechanism for a wingletted wing configuration.

5.2 Analytical and Numerical Model Definitions

Using the discrete models derived from the Rayleigh-Ritz Method (RRM) and Finite Element Method (FEM), one can now proceed with the aeroelastic analysis of any given wing configuration. Both numerical methods were applied in order to evaluate their computational requirements and accuracy. For instance, the first technique applied to the analysis was the Rayleigh-Ritz Method, where the shape functions describing the first mode of vibration for bending and torsion were employed (See Figure 5.1).The results from aeroelastic analysis agreed with the ones found in the literature for a planar wing [2, 4]. However, limitations were found when a winglet was added to the structure. This model failed to capture the response of the wingletted system because it was constrained to represent the first mode of vibration.

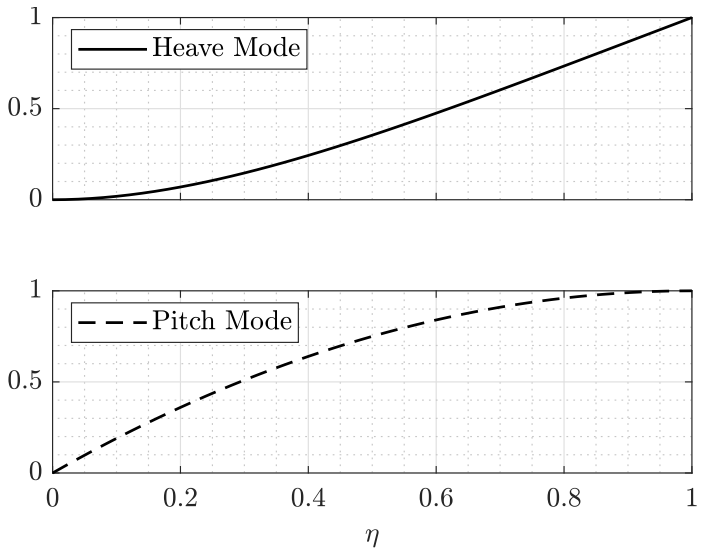

Fig. 5.1: Non-dimentionalized shape functions describing first mode in bending and torsion of a fixed-free beam

Chapter 4 introduced the Finite Element Method as the second technique applied in this analysis. The implementation of this technique required a discretization process where the structure was divided into multiple elements. In order to determine the number of elements needed for the analysis, it was necessary to perform a convergence analysis. This process allow us to investigate the relative error of the solution versus the number of elements in which the wing segments were divided. The graphs presented in Figure 5.2 indicate that the relative error of the natural frequencies for the pitch and heave modes rapidly decrease as the number of elements increases. The rate at which the relative error decreases for each mode is different. This comes as a result of the cubic and linear interpolation functions used to describe the bending and angular displacement of a beam, respectively (see Equations 4.34 and 4.35). From those results, it was determined to use ten elements since this quantity allowed the relative error to drop more than three orders of magnitude. This allowed us to refine the solution and improve the results.

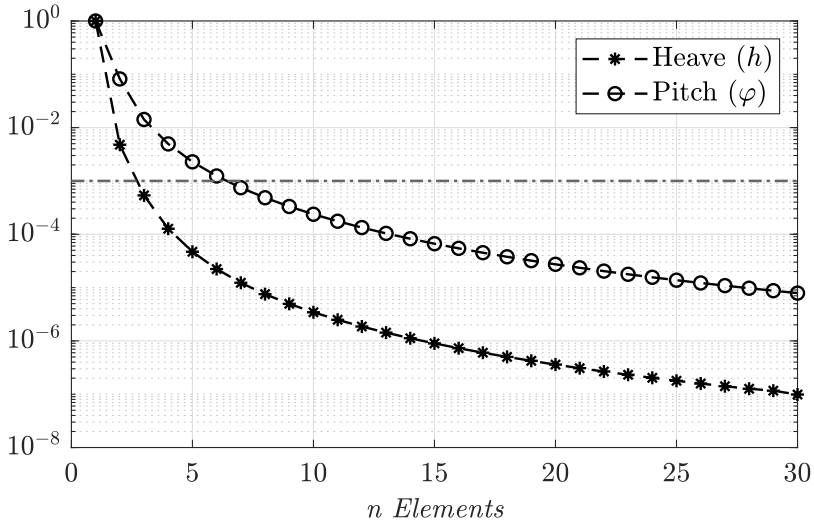

Fig. 5.2: Convergence analysis results for the pitching and bending modes

5.3 Aeroelastic Analysis Results of a Planar Wing

This section presents and describes the findings obtained from the aeroelastic analysis performed on a planar wing using the aerodynamic models presented in Section 3.3. These aeroelastic models yield different results, which are observed in the charts from Figure 5.3.

As a first step, an undamped aeroelastic model that employs a Steady Flow Model and ignores the effects of aerodynamic damping is considered. As it is presented in Figure 5.3(a), this aeroelastic model shows that, as the incoming flow speed U increases, the bending and torsion frequencies approach each other until they *coalesce* at 333 ft/s. At the same time, one can look at the real part of the eigenvalue and notice that the system remains marginally stable until both frequencies coalesce. After that point, the real part of the eigenvalue associated to the pitch mode becomes positive, and the real part of the eigenvalue associated to the heave mode turns negative. This indicates that *flutter* has occurred, and the system has become unstable.

Aerodynamic damping becomes part of the aeroelastic analysis when a Quasi-steady Flow Model is implemented. One can observe different results compared to the ones depicted in Figure 5.3(a), which ignores damping. This analysis shows that both frequencies approach one another, but they do not coalesce. Nevertheless, the flutter speed U_f can be identified by taking a closer look at the $Re(\lambda)$ versus U plots presented in Figure 5.3 (b). From the figure, it is observed that the real part of the eigenvalues for the pitch and heave modes are stable until the flutter

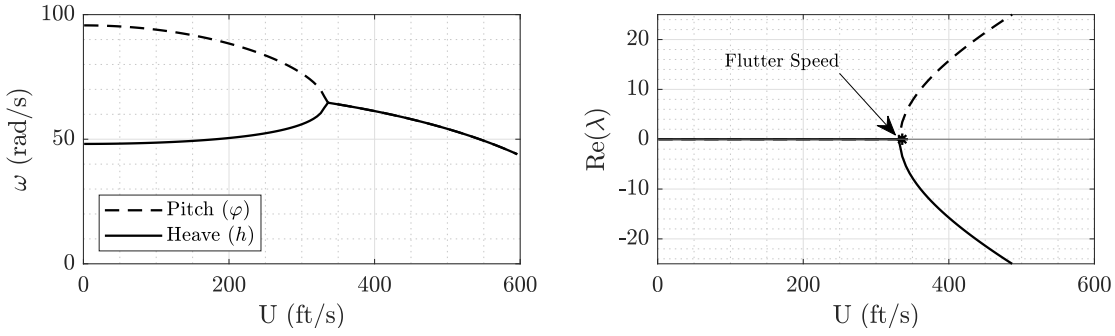

(a) Steady Flow Model

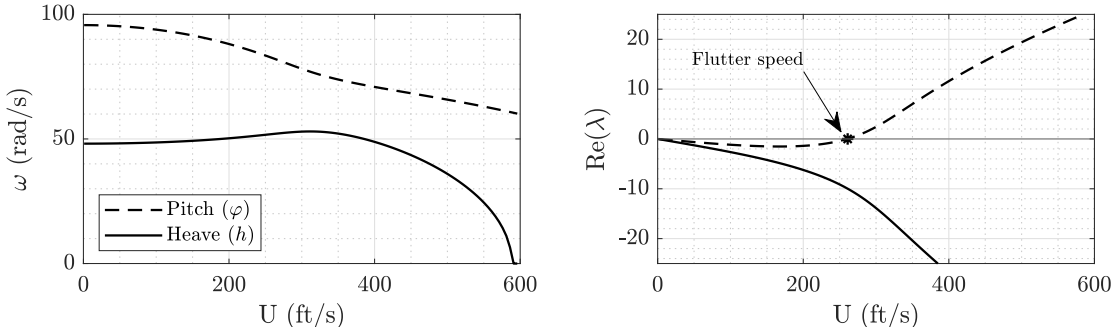

(b) Quasi-steady Flow Model

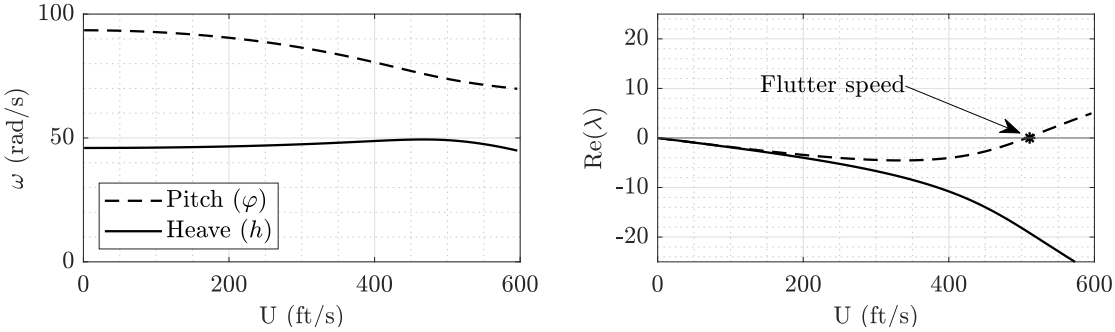

(c) Unsteady Flow Model

Fig. 5.3: Flutter speed approximation results for a wing without a winglet.

condition is reached. In that situation, the real part of the pitch mode becomes unstable, $Re(\lambda) > 0$, while the heave mode remains stable. This indicates that the damping coefficient associated to the pitch mode has become negative and can no longer remove energy from the system. Thus, the aeroelastic system becomes

unstable at 261 ft/s. This is a lower airspeed compared to the one obtained for the Steady Flow Model. The difference in the results is due to the fact that this model considers the effects of the heave rate $\dot{h}$. This leads to a larger effective angle of attack; hence, it increases the magnitude of the aerodynamic forces and moments generated and exacerbates the deformation of the structure.

Additional complexity is added to the analysis when the Unsteady Flow Model is applied. The numerical results from Figure 5.3(c) exhibit a similar trend to the ones obtained from the Quasi-steady Flow Model. The main difference between the results is that flutter occurs at 506 ft/s, which is the highest flutter speed compared to the other models. This is due to Theodorsen's complex valued function that considers the effects of an oscillating wing. Since the magnitude and phase change as a function of the reduced frequency k, this approach adds additional terms to the aerodynamic damping matrix $[C_{aero}]$. Once again, it can be observed that the pitch mode has become unstable when the damping becomes negative, i.e. $Re(\lambda) > 0$.

Similar results can be observed when the FEM approach is taken. However, the difference in the results comes as a consequence of the shape or trial functions implemented. Also, FEM describes the deformation of the structure at multiple discrete points while the RRM describes the deformation of the entire structure as one element.

5.4 Aeroelastic Analysis Results of a Wignletted Wing

The same procedure outlined in Section 4.3 is followed to estimate the flutter speed for a system that includes a winglet. Consider a structure where the winglet length is half the length of the wing panel or segment ($\ell_2 = \ell_1/2$) and has a cant angle of 90°. In addition, each section of this configuration has the same inertial and elastic properties of the Goland Wing. Figure 5.4 shows the results from the undamped wingletted wing system, and these were obtained through the implementation of the Rayleigh-Ritz Method in combination with the eigen-functions as shape functions. These results are also compared to those presented in Figure 5.3(a), which will be referred to as the reference wing results.

From the undamped aeroelastic system, it can be observed that there are two points where the heave and pitch frequencies coalesce. These correspond to the first and second instability points or flutter boundaries, $Re > 0$. The first flutter boundary indicates that the system reaches unstable conditions at 260 ft/s, while the second boundary is defined at a higher flight speed of 710 ft/s. Therefore, the instability of the system is dominated by the first flutter boundary. This is attributed to the added mass of the winglet. Moreover, these results agree with the analysis performed by Snyder and Weisshaar [34]. In addition, when compared to the reference wing, the data shows that this configuration outperforms the wingletted wing structure. The reference wing reaches flutter conditions at 340 ft/s, which means that this configuration has a larger flight envelope.

In order to verify the aeroelastic analysis, the FEM approach is implemented

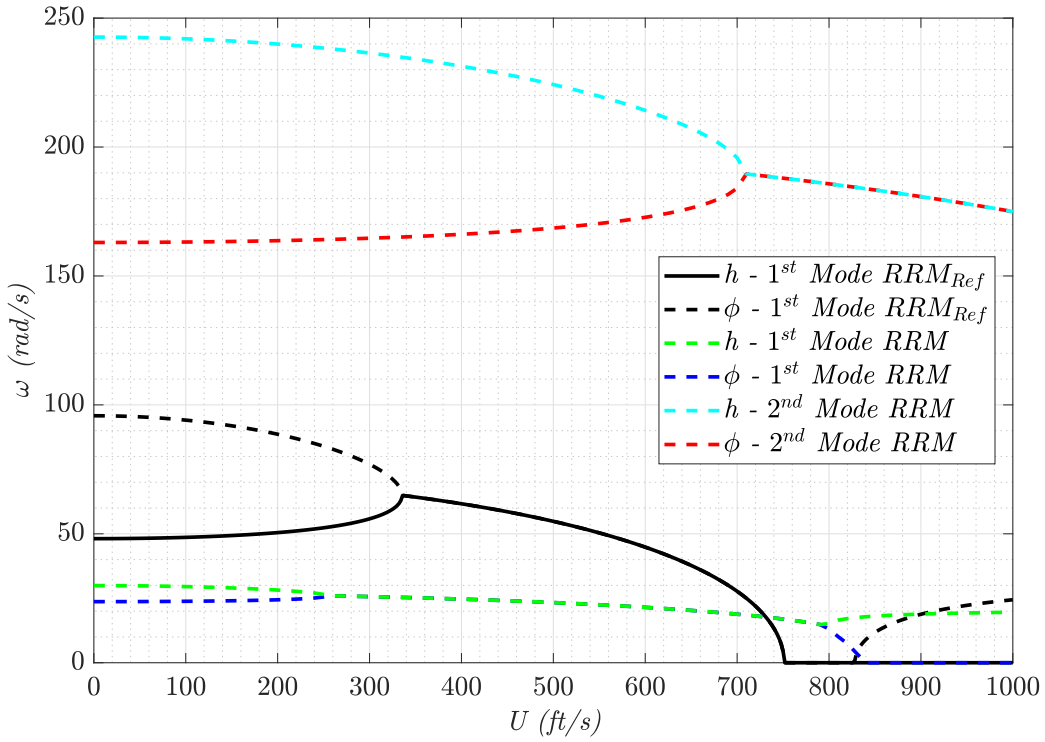

Fig. 5.4: Aeroelastic analysis results of a wing with and without a winglet via application of the Rayleigh-Ritz Method.

and compared to the data previously generated through the Rayleigh-Ritz Method. These results are presented in Figure 5.5. The figure shows that there are two sets of results that represent the first and second modes of vibration for pitch and heave of the aeroelastic system for each approach. In addition, one can notice some differences between both methods. In the FEM solution, the second modal frequencies for pitch and heave coalesce at 640 ft/s, whereas the first pair of modal frequencies did not coalesce. By comparing to the results obtained through the RRM approach, the second pair of modes reached flutter conditions because the real part of the eigenvalues becomes unstable. Moreover, it is noted that the second flutter boundary obtained through RRM is higher than the one provided by the FEM solution.

These differences are a result of the different approximate solution techniques used. However, the FEM approach can capture higher modes of vibration, and this allows the method to provide some level of refinement in the solution.

To further understand the results depicted in Figure 5.5, it is necessary to examine the eigenvalues in the complex plane. In Figure 5.6, it can be pointed out that for all cases the pitch mode becomes unstable, except for the first mode in pitch given by the FEM solution. In that case, the eigenvalues associated to the first mode in pitch and heave remain marginally stable, $Re(\lambda_{\varphi,1}) = 0$, for all flight speeds. Nevertheless, the flutter condition of the system is determined by the second pitch mode of vibration when $Re(\lambda_{\varphi,2}) > 0$. In this case, the situations in which the first heave and pitch mode remain marginally stable, while second pitch mode becomes unstable is defined as *Mode Switching*.

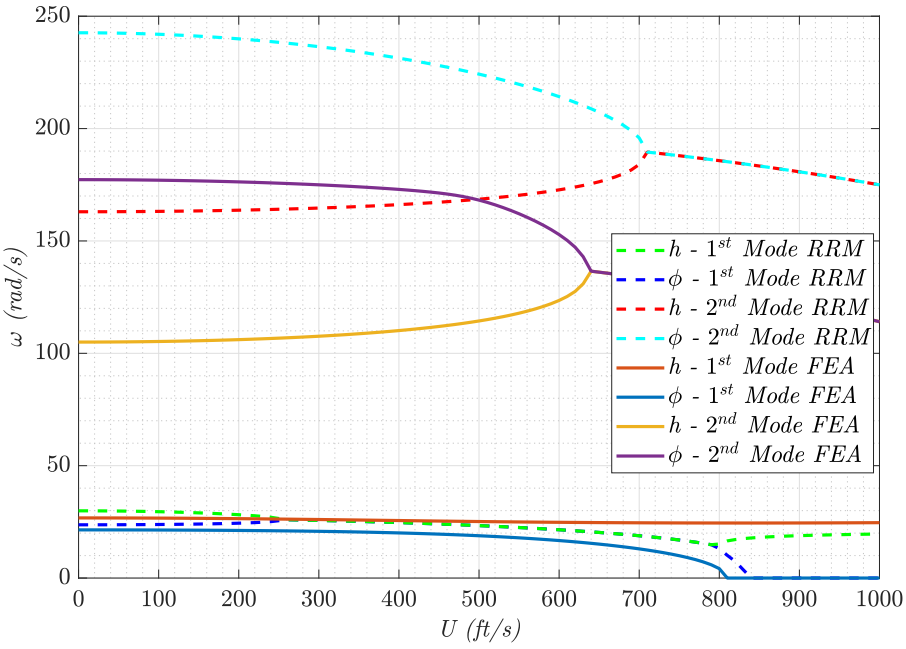

Fig. 5.5: Comparison of dynamic aeroelastic results between the FEM and RRM.

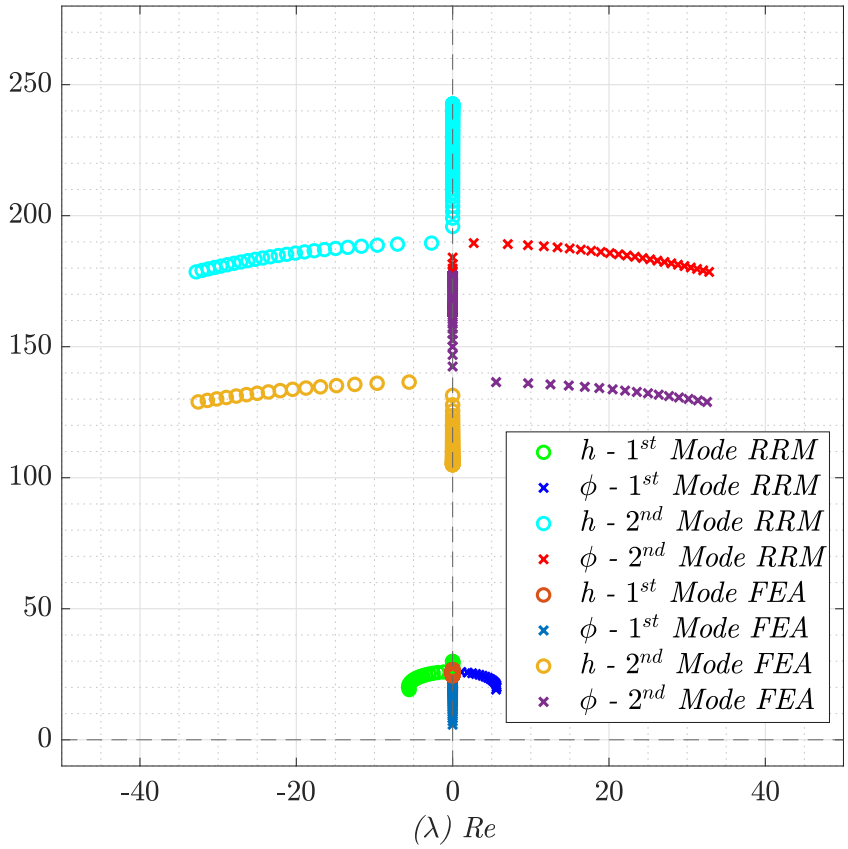

Fig. 5.6: Complex eigenvalues representing the first and second modes for pitch and heave obtained from using FEM and RRM.

The previous results have indicated that having a winglet to wing length ratio of 0.5 is beneficial to aeroelastic stability. Now, let us investigate the effects of increasing the length of the winglet segment and using the same sectional inertial and structural properties as the Goland Wing. This study yielded the results presented in Figure 5.7 that have been normalized by the flutter speed of a wing without a winglet, $U_{f_{Ref}} = 333 ft/s$. The resulting charts indicate that Mode Switching is triggered when the winglet length is greater than 48% of the length of the inboard wing section. It should also be noted that having a winglet that is between 1% and

20% of the length of the wing segment can be favorable because it increases the critical flutter speed. It indicates that the first mode in torsion will reach dynamic instability at a higher speed. In that situation, the winglet acts as a mass damper by reducing the amplitude of displacement or deformation in bending and torsion for the entire structure. As a result, it reduces the magnitude of the distributed aerodynamic lift and moment produced by the lifting surface.

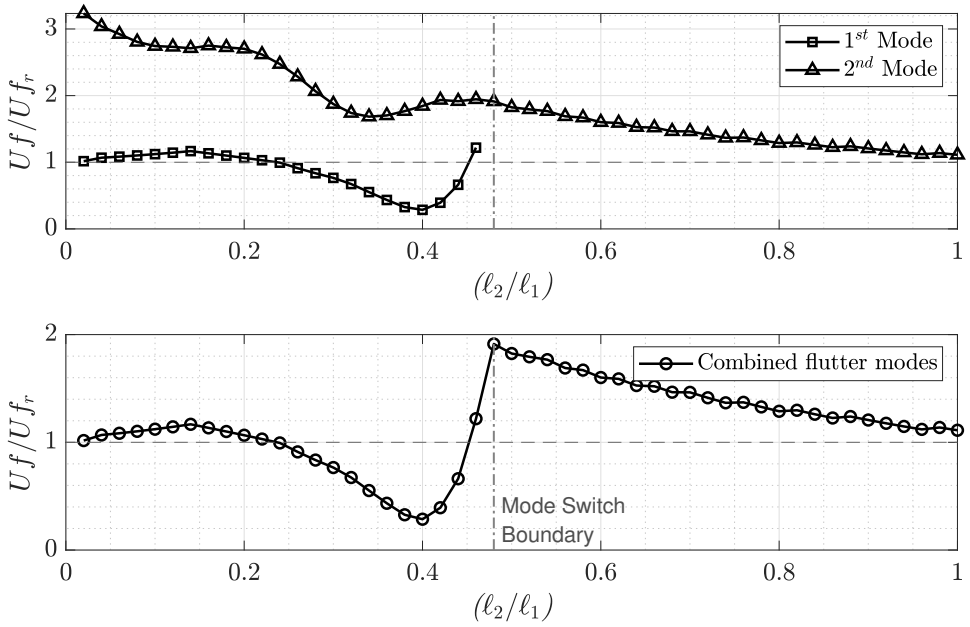

Fig. 5.7: Mode switching boundary determination between the first and second flutter modes through variations of winglet length variation with respect to inner wing segment length.

From the numerical results, it is also noticeable that a flutter condition is achieved at a lower speed when the length of the outboard wing ranges from 20% to 45% of that of the inboard wing panel. This occurs because the winglet panel is large enough to produce a significant amount of aerodynamic lift and moment. As

a result, it exacerbates the deformation of the entire structure. Once the length of the winglet is greater than half the length of the inner wing, the second torsional mode becomes unstable. In the meantime, for all flight conditions provided, the first torsional mode remains marginally stable. In other words, the second torsional mode of vibration defines the stability boundary of the system, which is an indicative of Mode Switching.

Thus far in this section, only an undamped aeroelastic systems has been the subject of our analysis. However, it is important to consider the effects of having the quasi-steady and unsteady flow models applied to the wingletted wing configurations previously studied. Comparable results can be observed when both aerodynamic models are applied to the same configuration that yielded the results in Figure 5.4. These results are shown in Appendix A.

The aeroleastic analysis yields to the graphs presented in Figure 5.8, which are similar to the ones generated by using a steady flow model. The analytical data shows that the mode switching phenomenon is still present for both solutions when the length of the winglet panel is varied. The most noticeable difference between the models is that mode switching occurs for different winglet panel lengths. When the quasi-steady flow model is applied to the analysis, it indicates that mode switching occurs for a winglet that is 60% the span with respect to the inboard section. On the other hand, the application of unsteady aerodynamics yields a different result. Mode switching takes place when the length of the winglet is 52% the length of the wing section.

In addition to the previous remarks, it can be observed that the aeroelastic

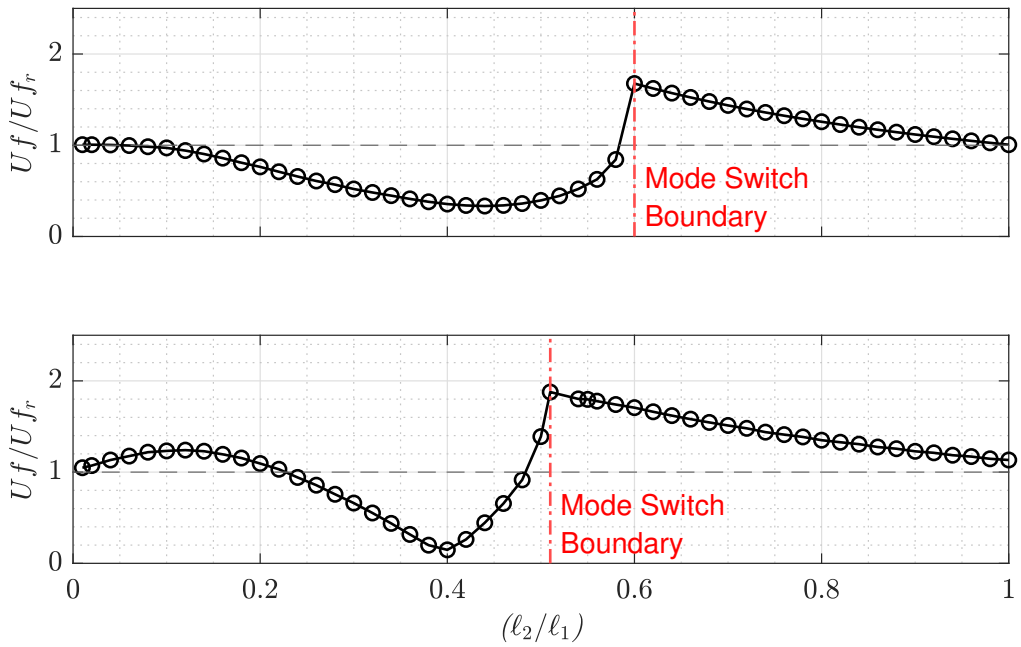

Fig. 5.8: Mode switching boundary determination between the first and second flutter modes for quasi-stead and unsteady flow models.

model featuring the quasi-steady flow model did not exhibit a major increase of the flutter speed compared to the Unsteady Flow Model. This is a result of the larger effective angle of attack, α_{eff}, which is due to the combination of $\dot{h}$ and φ, as described in Section 3.3.3. The results from the application of the unsteady flow model indicate that there is an improvement on the flutter speed for configurations where ℓ_2/ℓ_1 is less than 0.22. However, for configurations where ℓ_2/ℓ_1 is between 0.22 and 0.5, the flutter speed severely decreases.

Another aspect that requires investigation is the effect of changing the winglet cant angle γ. The variation of this geometric parameter can enable mission adaptability and the implementation of winglets as control surfaces. This could possibly allow the designers to reduce the size of the vertical stabilizer or remove it. Now,

consider a wingletted wing where $\ell_2 = \ell_1/2$ with a variable cant angle γ between $-90°$ and $90°$. By applying the iterative process outlined in Figure 4.6 and the FEM approach, one can predict the speed that satisfies the flutter condition and produce results given in Figure 5.9.

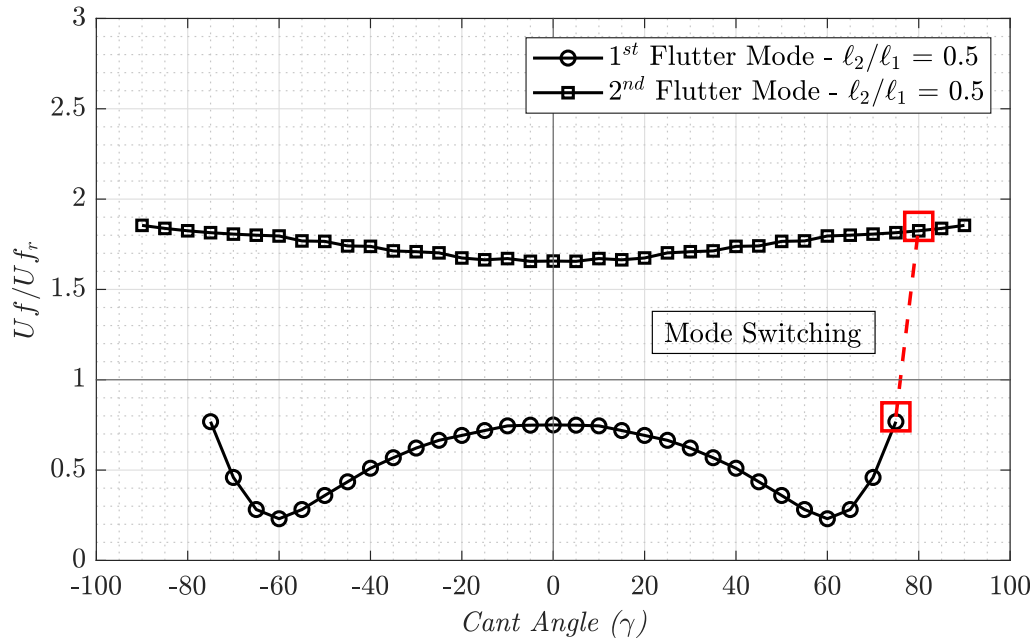

Fig. 5.9: Normalized flutter speed variation as a function of cant angle γ from -90^o to 90^o for a $\ell_2/\ell_1 = 0.5$ configuration using a steady flow model.

The data presented in Figure 5.9 shows that the flutter speed is affected by the cant angle. Once again, it is observed that there are two flutter boundaries, which correspond to the first and second pair of modes in heave and pitch. For cant angles greater than 75°, it is also noticeable that the mode switching phenomenon arises. This shows that mode switching is susceptible to changes in cant angle.

In a similar manner, two winglet to wing length ratios were analyzed, $\ell_2/\ell_1 = 0.15$ and $\ell_2/\ell_1 = 0.85$. The data presented in Figure 5.10 shows that for a config-

uration where $\ell_2/\ell_1 = 0.15$ mode switching does not occur because the stability of the system is dominated by the first flutter mode. In addition, the flutter speed increases for cant angles greater than $\pm 45°$ because the magnitude of the lift generated in the y-axis decreases, and the smaller winglet works as a mass damper. This shows that smaller winglets can help improve aeroelastic characteristics. It is important to mention that the results presented in Figures 5.9 and 5.10 are symmetric with respect to the y-axis, meaning that the plots exhibit identical values for the normalized flutter speed when the cant angle becomes negative. This is caused by the uniform spanwise lift distribution on the wing and winglet panels.

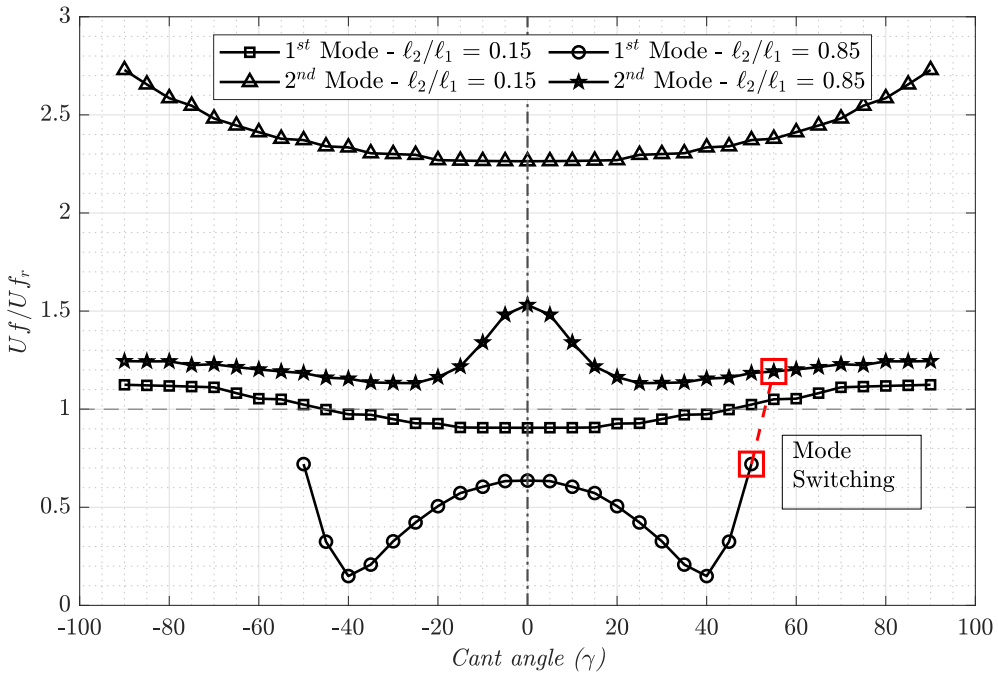

Fig. 5.10: Normalized flutter speed variation of winglet cant angle γ from -90^o to 90^o, $\ell_2/\ell_1 = 0.15$ and $\ell_2/\ell_1 = 0.85$

On the other hand, different results are observed for the $\ell_2/\ell_1 = 0.85$ winglet-ted wing configuration. It is noted that the first and second flutter modes are closer

to each other if compared to the ones obtained from the $\ell_2/\ell_1 = 0.15$ configuration. This shows that the flutter speeds obtained for this configuration are lower, and the flight envelope has been reduced. In addition, mode switching arises when the cant angle is greater than $\pm 50°$, and once again the second flutter mode drives the system unstable.

In a similar manner, the quasi-steady and unsteady flow models were evaluated for a $\ell_2/\ell_1 = 0.50$ wingletted wing configuration. In Figure 5.11, it can be observed that the first flutter mode is heavily affected by the addition of a winglet panel at zero degree cant angle. As the cant angle varies from $0°$ to $\pm 60°$, it is noted that the speed at which the first flutter mode occurs decreases, and it gradually increases after that point. The second flutter mode exhibits a very small variation with the changes in cant angle γ, but these results are not as noticeable as before when compared to the $\ell_2/\ell_1 = 0.50$ configuration with the steady flow model.

The implementation of unsteady aerodynamics produced the data in Figure 5.12. These results show that both flutter modes are greatly affected by the variations in cant angle. Again, it is noticeable that the flutter speed decreases from $0°$ to $\pm 60°$. However, when the flutter speed increases, it outperforms the wing without the winglet panel or reference wing. The second flutter mode shows a rapid increase in flutter speed when the cant angle is greater than $\pm 50°$. These differences in flutter speed are attributed to the variation in rotational inertia of the winglet panel, which makes difficult the rotation of the winglet. This causes the torsional frequency to decrease and the bending frequency to increase, which changes the aeroelastic response of the system.

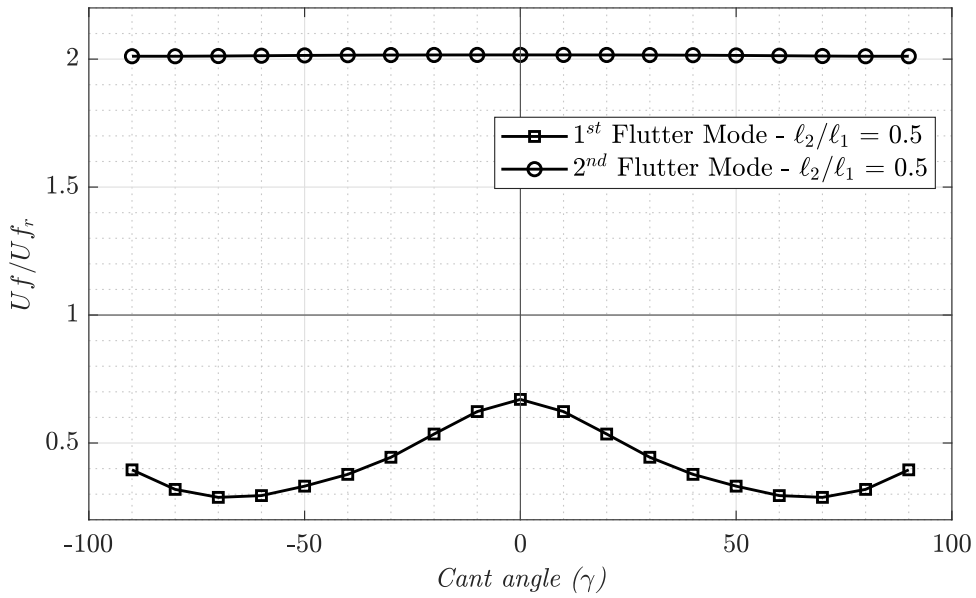

Fig. 5.11: Normalized flutter speed variation as a function of cant angle γ from -90^o to 90^o using a quasi-steady flow model

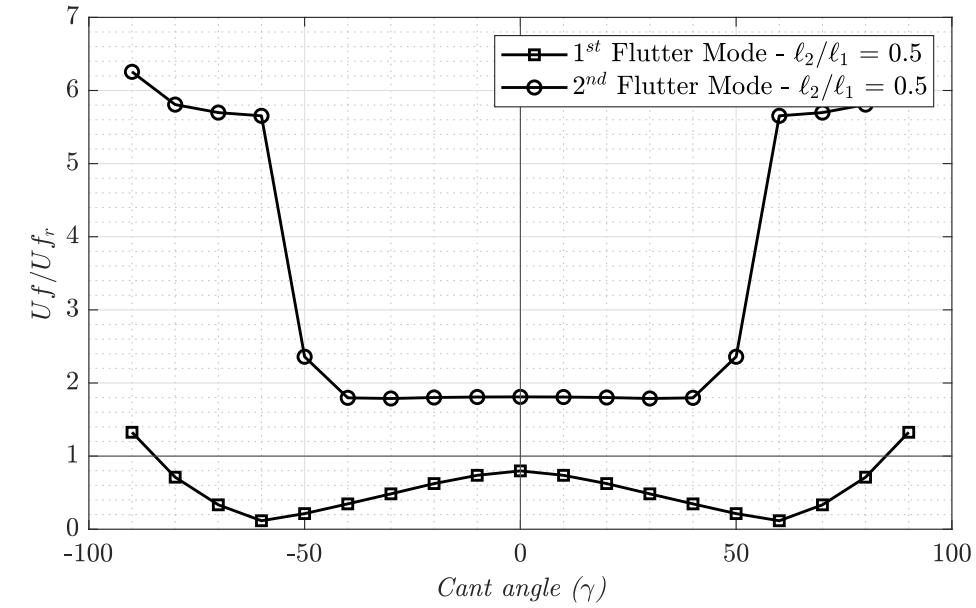

Fig. 5.12: Variation of winglet cant angle γ from -90^o to 90^o using an unsteady flow model, $\ell_2/\ell_1 = 0.50$

For completeness, both aerodynamic models have been applied to two winglet to wing length ratios, $\ell_2/\ell_1 = 0.15$ and $\ell_2/\ell_1 = 0.85$. First, the results from the quais-steady flow model are presented in Figure 5.13. It is observed that mode switching does not occur for the $\ell_2/\ell_1 = 0.15$ configuration. Note that the variations in flutter speed for each mode in this configuration do not present a major change as a function of cant angle, and instability of the system is driven by the first flutter mode. For the second configuration, $\ell_2/\ell_1 = 0.85$, the results show larger variations in the flutter speed for both modes, and it includes the presence of mode switching. Moreover, this configuration does not present an improvement in aeroelastic performance in comparison with the reference wing.

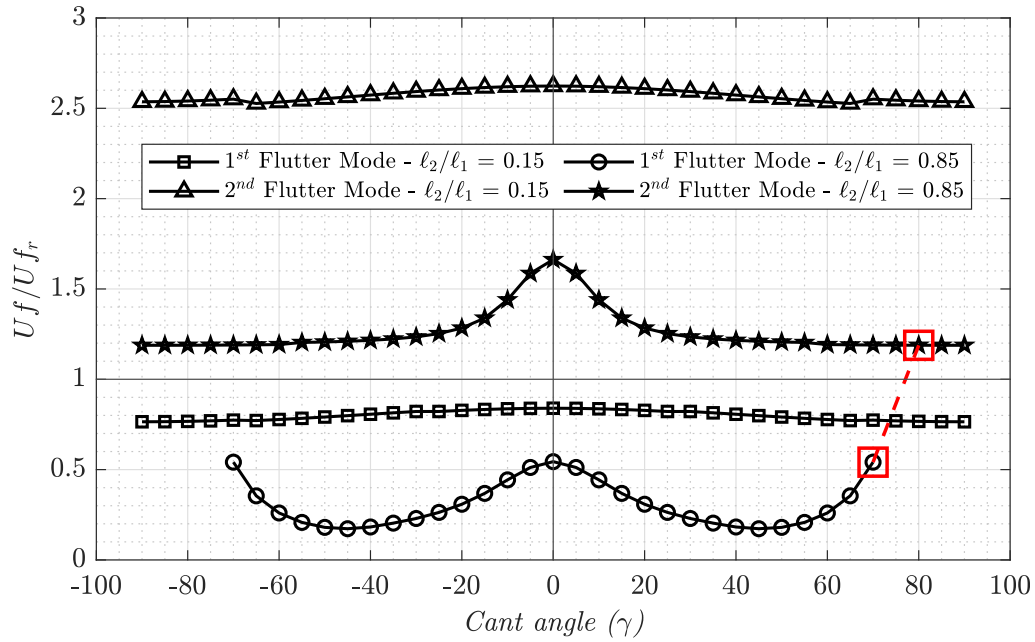

Fig. 5.13: Normalized flutter speed variations as function of cant angel γ from -90^o to 90^o for $\ell_2/\ell_1 = 0.15$ and $\ell_2/\ell_1 = 0.85$ configurations using a quasi-steady flow model.

The data presented in Figure 5.14 is the result of employing a unsteady flow model. By looking at the first flutter mode from the $\ell_2/\ell_1 = 0.15$ configuration, the data shows that for cant angles greater than $\pm 25°$ it can achieve higher flutter speeds compared to the reference wing. This is because the effects of the oscillating wing reduce the amplitude on the aerodynamic loads and lead to smaller deformation of the structure. It is important to mention that first flutter mode sets the instability boundary of the system. At the same time, it can be observed that the flutter speed is greatly reduced for the larger winglet configuration ($\ell_2/\ell_1 = 0.85$) as a result of the added inertia. One can also observe that mode switching occurs for cant angles larger than $\pm 60°$, and once again the aeroelastic instability of the system is dominated by the second flutter mode.

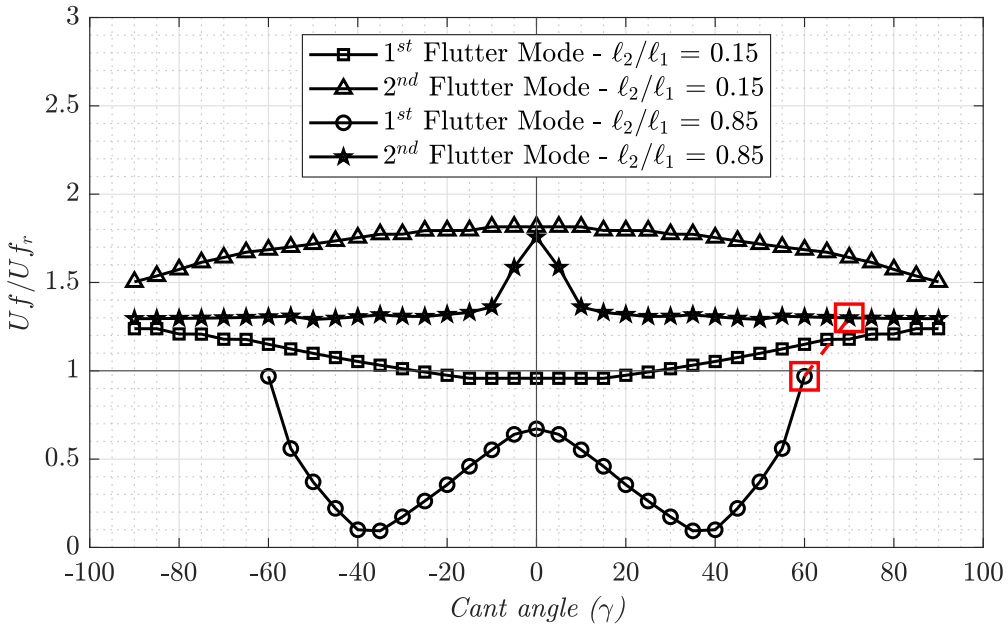

Fig. 5.14: Normalized flutter speed variations as function of cant angel γ from -90^o to 90^o for $\ell_2/\ell_1 = 0.15$ and $\ell_2/\ell_1 = 0.85$ configurations using an unsteady flow model.

The results from the three aeroelastic models show similar trends for the behavior of the flutter modes as a function of cant angle. This indicates that this simplified model approach captures the physics of the problem. It has been observed that the $\ell_2/\ell_1 = 0.15$ configuration shows improvements in the aeroelastic performance of the models employing steady and unsteady flow aerodynamics. In addition, all models exhibited mode switching for the $\ell_2/\ell_1 = 0.85$ wingletted wing configuration. That showed that the second flutter mode defined a new stability boundary for the aeroelastic systems evaluated. These observations were easily identified looking at the governing equations outlined in Section 3.2.3, which also facilitated the understanding of the results.

Chapter 6: Conclusions

6.1 Summary of Work

Aeroelasticity is an important field that has shaped the way aircraft are designed. As a result, it is important to further understand its fundamental physics in order to develop new technology that can enable mission adaptability and improved performance over multiple missions. As a result, this research contributes to the understanding of dynamic aeroleasticity of wingletted wings with a variable cant angle and the Mode Switching phenomenon.

Chapters 3 and 4 focused on the derivation of the equations of motion for a continuous and discrete wingletted wing system. This was done through the application of multibody kinematics, energy methods, Euler-Bernoulli beam formulation, and two-dimensional flow theory. For the continuous system, the derivation process led to four partial differential equations that represent the pitch and heave motion of the structure along with its geometric and natural boundary conditions. Ordinary differential equations were obtained when the discretization methods were employed. These were necessary in order to develop a closed form solution to approximate the flutter speed of the wingletted wing structure. The equations representing the discrete and continuous system provided important information by showing the

interaction between forces and the wing-winglet motion. They also exhibited terms that describe the influence of the rigid body dynamics from the wing tip acting on the winglet in addition to its flexible body dynamics.

The results from the aeroleastic analysis presented in Chapter 5 indicate that having a vehicle equipped with an articulated outer wing section can be beneficial. Flutter speed increases for configurations where the winglet length with respect to the wing section length ranges from 1% to 20% and with a cant angle greater than 45°. Thus, it can allow for expansion of the flight envelope of an aircraft. However, this was only observable when the Steady and Unsteady Flow Models were applied. In addition to changes in flutter speed, another important result from the analysis was the *Mode Switching* phenomenon. This phenomenon, which was defined as the condition when the second mode in torsion became unstable while the first torsional mode remained marginally stable. For all three aerodynamic models used in the analysis, it was noted that Mode switching occurs for winglets to wing length ratios greater than 0.5 and cant angles larger than 50°. These findings suggest that flutter is sensitive to the winglet length and cant angle. This is a result of the rotational inertia of the winglet, which changes with length and cant angle. In addition, these results can be used as a reference for wingletted wing design and implementation for adaptive wing aircraft.

6.2 Novel Contributions from this Research

The original contributions presented here consist of a better understanding of the fundamental physics of the mode switching phenomenon. This was accomplished by verifying, validating, and expanding upon relevant previous work. Moreover, the current work presented the implementation of multibody kinematics that lead to the derivation of the equations of motion, which describe the aeroelastic response of the system as the winglet length and cant angle are changed. In addition to the governing equations, the geometric and natural boundary conditions of the system were obtained.

Furthermore, it has been observed that the changes in cant angle have an impact on the calculations of the flutter speed. At the same, this analysis has shown that the application of small winglets can expand the flight envelope of an aircraft. These findings are important to keep in mind in order to develop new multi-role aircraft that could perform various mission profiles.

Another novel contribution of this work includes the development of three linear aeroelastic models to analyze this type of structures. These models have lower computational requirements compared to their higher order counterparts. This enables the production of charts and establish trends describing the aeroelastic characteristics for various wingletted wing configurations. The charts produced can be used as a first approach to design and optimize new aircraft design parameters. It can also allow to establish a preliminary flight envelope for new air vehicle concepts.

6.3 Future Research Work

Future research suggested by this work wind tunnel testing and a high order model solution through a fluid-structure-interaction study. Dynamic and static wind tunnel testing is necessary to verify the analysis presented in this research and to create an aerodynamic data base to study other configurations. A static wind tunnel test program will generate the aerodynamic data necessary to accurately represent the spanwise lift and moment loading distribution. An aeroelastic experiment will allow observation and analysis of the dynamic response of the system under oscillatory motion.

A high order model solution will further verify the data produced in this work. In addition, it can incorporate the analysis of other parameters that affect flutter or Mode Switching, such as the location of the elastic axis, variations of inertial properties, and others. Overall, a fluid-structure-interaction study and/ or wind tunnel testing will add more information about the aeroelastic characteristics of the system and improve upon the results presented in this work.

APPENDIX

Appendix A: Additional Aeroelastic Analysis Results for a Wingletted Wing

This appendix shows additional results obtained from the aeroelastic analysis of the wingletted wing system, namely the results including the quasi-steady and unsteady flow models. Consider a structure where the winglet length is half the length of the wing panel or segment ($\ell_2 = \ell_1/2$) and has a cant angle of 90°. One can observe that there are two data sets representing the first and second modes of vibration for pitch and heave of the system. These results presented in Figure A.1 are similar to the ones obtained for a planar wing with a quasi-steady flow model (see Figure 5.3 (b)). In this situation, the frequencies approach one another, but they do not merge or coalesce. However, it is possible to identify the flutter speed by looking at Figure A.2. One can observe that the real part of the eigenvalues for the pitch mode becomes positive. In addition, the system reaches an unstable condition at a lower speed when compared to the reference wing results.

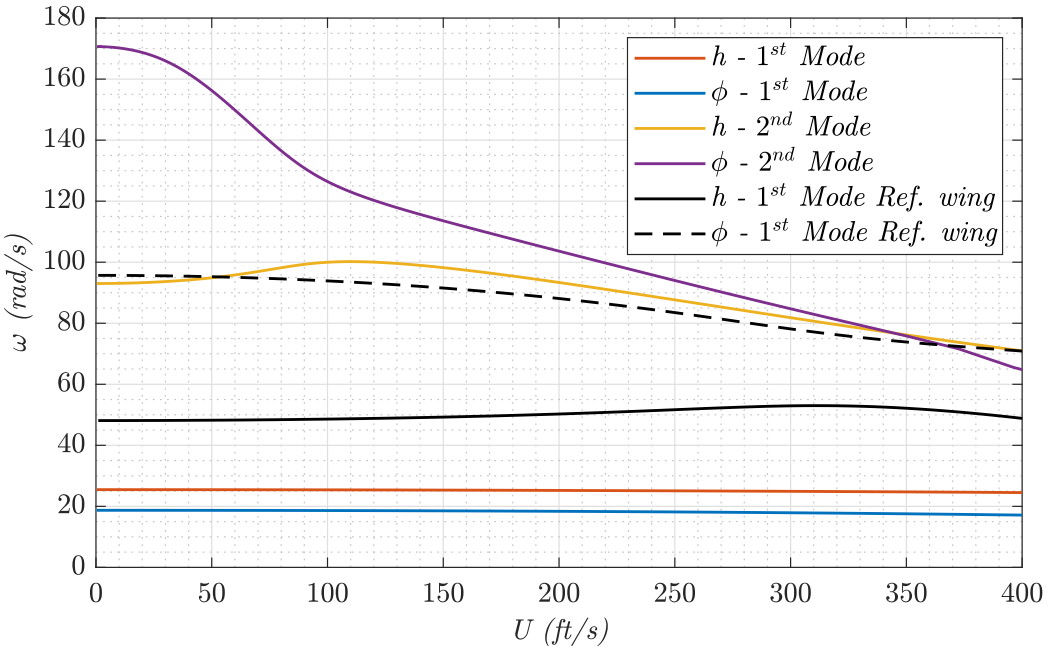

Fig. A.1: Aeroelastic analysis results of a wing with and without a winglet via FEM using a quasi-steady flow model, $\ell_2/\ell_1 = 0.50$.

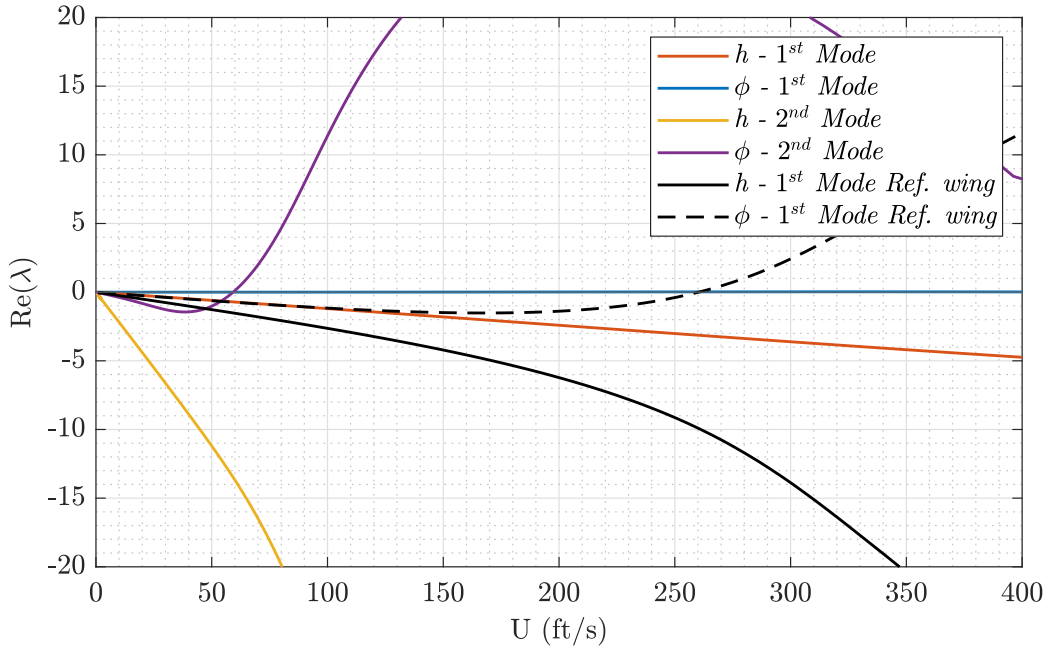

Fig. A.2: Real part of the eigenvalues as function of the airspeed for a $\ell_2/\ell_1 = 0.50$ wingletted wing configuration using a quasi-steady flow model.

Similar trends are observed in the data presented in Figures A.3 and A.4, which correspond to the aeroelastic model employing unsteady aerodynamics. In Figure A.4, it is noted that the first pitching mode of the $\ell_2/\ell_1 = 0.5$ wingletted wing configuration becomes unstable at a higher speed if compared to the reference wing. It can also be seen the aeroelastic instability of the system is dominated by the first pitching mode, whereas the second mode becomes unstable at a much higher airspeed.

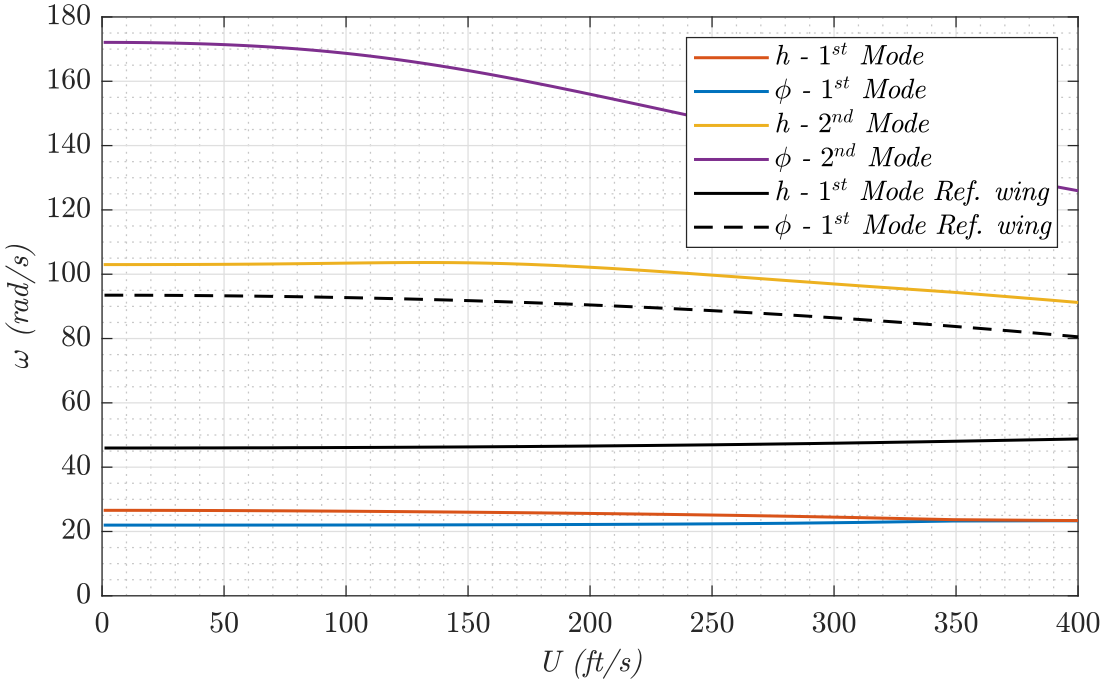

Fig. A.3: Aeroelastic analysis results of a wing with and without a winglet via FEM using an unsteady flow model, $\ell_2/\ell_1 = 0.50$.

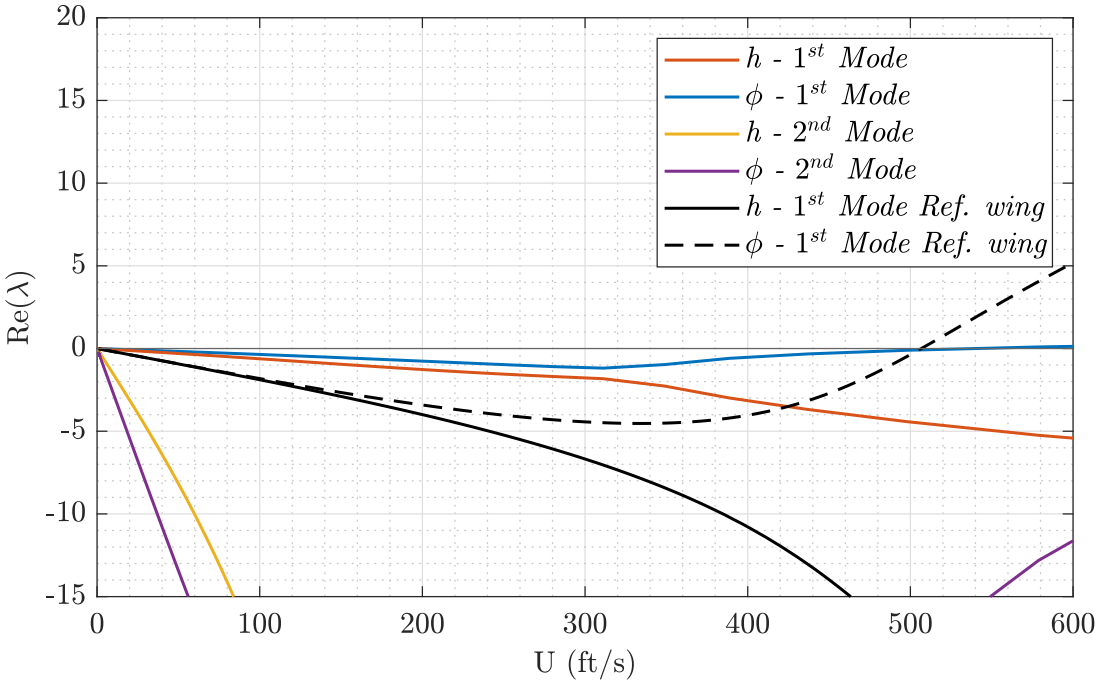

Fig. A.4: Real part of the eigenvalues as function of the airspeed for a $\ell_2/\ell_1 = 0.50$ wingletted wing configuration using an unsteady flow model.

On the other hand, when $\ell_2/\ell_1 = 0.85$ and $\gamma = 90°$, one can observe mode switching for both models. The application of quasi-steady aerodynamics leads to the results presented in Figures A.5 and A.6, where it is determine that mode switching has occurred. In Figure A.6, it is seen that real part of the eigenvalues corresponding to the pitch mode has become unstable. The first pitch mode remains marginally stable. Comparable results are observed in Figures A.7 and A.8 when an unsteady aerodynamic flow model is incorporated.

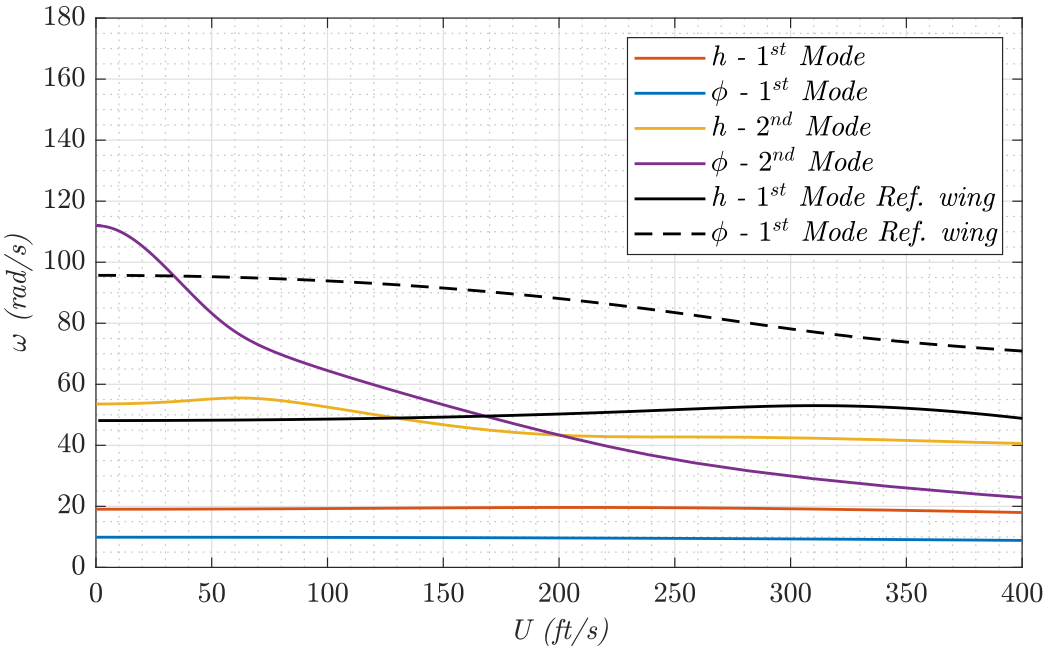

Fig. A.5: Aeroelastic analysis results of a wing with and without a winglet via FEM using a quasi-steady flow model, $\ell_2/\ell_1 = 0.85$.

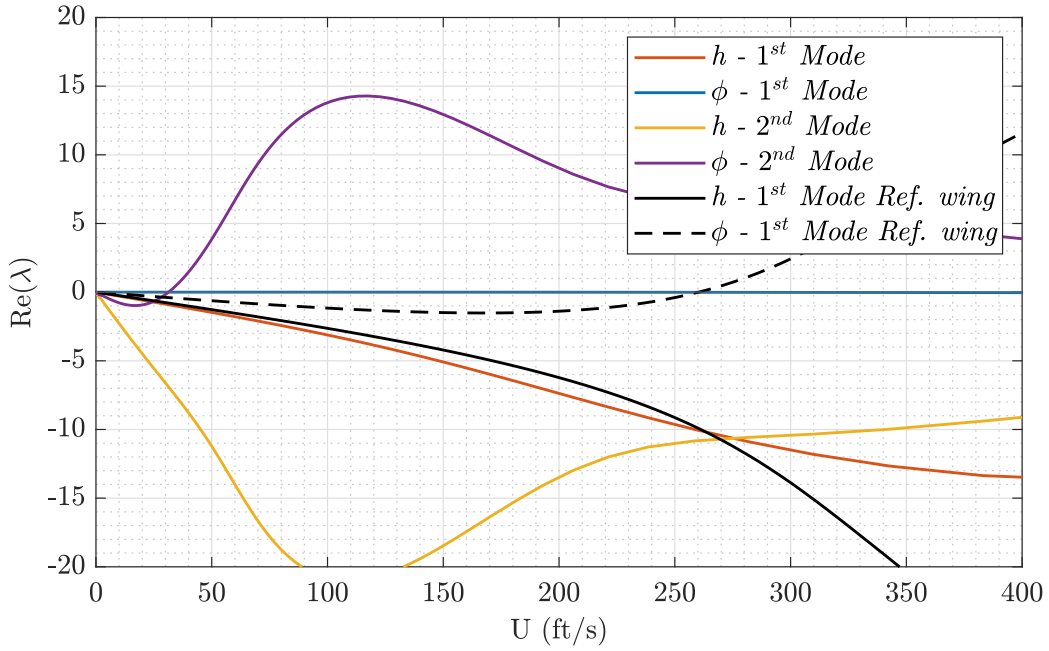

Fig. A.6: Real part of the eigenvalues as function of the airspeed for a $\ell_2/\ell_1 = 0.85$ wingletted wing configuration using a quasi-steady flow model.

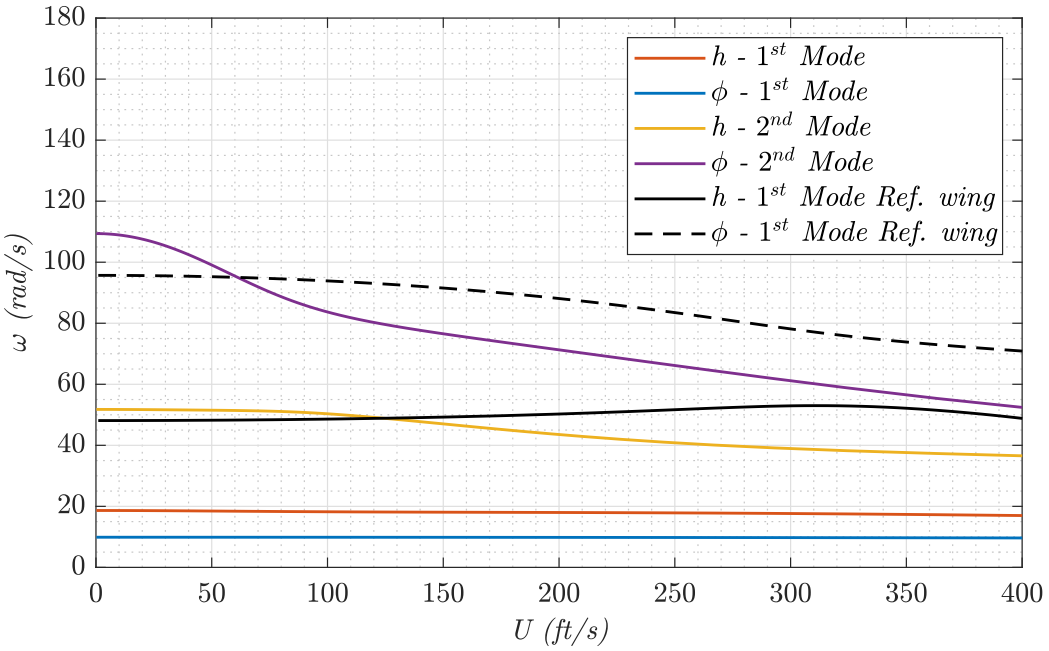

Fig. A.7: Aeroelastic analysis results of a wing with and without a winglet via FEM using an unsteady flow model, $\ell_2/\ell_1 = 0.85$.

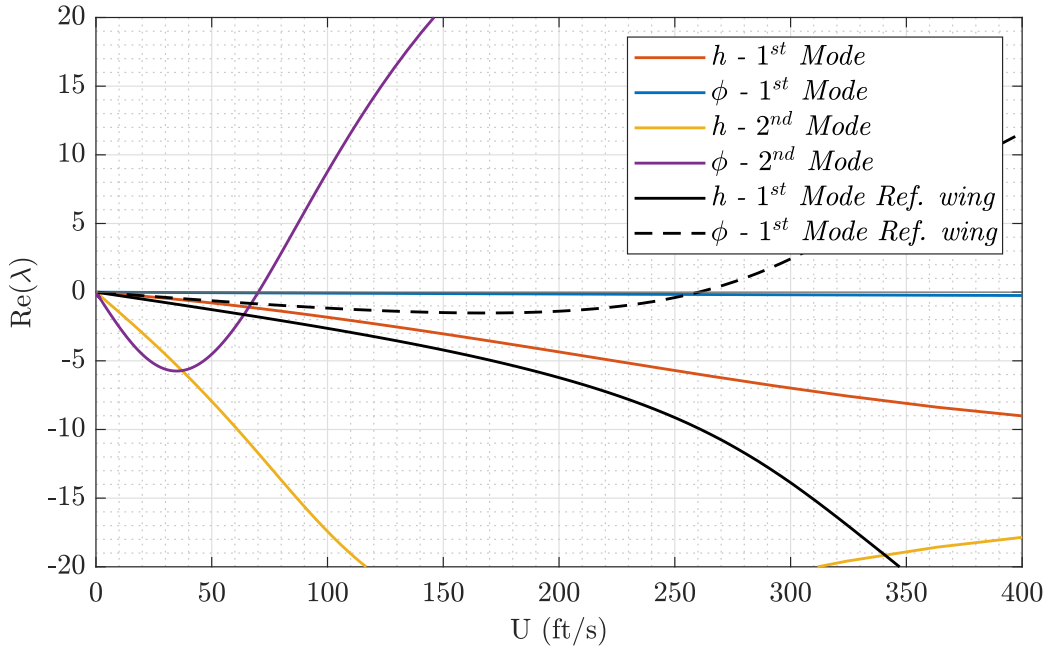

Fig. A.8: Real part of the eigenvalues as function of the airspeed for a $\ell_2/\ell_1 = 0.85$ wingletted wing configuration using an unsteady flow model.

Bibliography

[1] A. R. Collar, "The first fifty years of aeroelasticity," *Aerospace*, vol. 5, pp. 12 –20, 02 1978.

[2] D. H. Hodges and G. A. Pierce, *Introduction to Structural Dynamics and Aeroelasticity*, vol. 15. cambridge university press, 2 ed., 2011.

[3] E. Dowell, R. Clark, D. Cox, H. Curtiss, J. Edwards, K. Hall, D. Peters, R. Scanlan, E. Simiu, F. Sisto, and S. T.W., *A Modern Course in Aeroelasticity*, vol. 116. Springer Science+ Business Media, Inc., 2005.

[4] J. Wright and J. Cooper, *Introduction to Aircraft Aeroelasticity and Loads*, vol. 20. John Wiley & Sons, 2008.

[5] L. Bisplinghoff, H. Ashley, and R. Halfman, *Aeroelasticity*. Dover Publications, Mineola, NEW YORK, 1996.

[6] I. Garrick and W. Reed III, "Historical development of aircraft flutter," *Journal of Aircraft*, vol. 18, no. 11, pp. 897–912, 1981.

[7] F. Lanchester, "Torsional vibrations of the tail of an aeroplane," *Aeronaut. Research Com. R & M*, vol. 276, 1916.

[8] M. Kehoe, "A historical overview of flight flutter testing," *NASA Technical Memorandum*, no. 4720, 1995.

[9] N. S. on Vibration and Flutter, "A survey and evaluation of flutter research and engineering," Tech. Rep. RM–56I12, National Advisory Committee for Aeronautics, October 1956.

[10] R. Frazer and W. Duncan, "The flutter of aeroplane wings," *The Aeronautical Journal*, vol. 33, no. 222, pp. 407–454, 1929.

[11] T. Theodorsen, "General theory of aerodynamic instability and the mechanism of flutter," Tech. Rep. NACA - 496, National Advisory Committee for Aeronautics, 1935.

[12] M. Goland, "The flutter of a uniform cantilever wing," *Journal of Applied Mechanics-Transactions of the ASME*, vol. 12, no. 4, pp. A197–A208, 1945.

[13] A. Rodriguez, "Morphing aircraft technology survey," in *45th AIAA aerospace sciences meeting and exhibit*, p. 1258, 2007.

[14] T. A. Weisshaar, "Morphing aircraft systems: historical perspectives and future challenges," *Journal of Aircraft*, vol. 50, no. 2, pp. 337–353, 2013.

[15] T. A. Weisshaar, "Morphing aircraft technology-new shapes for aircraft design," tech. rep., PURDUE UNIV LAFAYETTE IN, 2006.

[16] D. Bye and P. McClure, "Design of a morphing vehicle," in *48th AIAA/ASME/ASCE/AHS/ASC structures, structural dynamics, and materials conference*, p. 1728, 2007.

[17] Y. Gibbs, "NASA tests new alloy to fold wings in flight." Available at `https://www.nasa.gov/centers/armstrong/feature/nasa-tests-new-alloy-to-fold-wings-in-flight.html`, January 2018 (accessed June 09, 2019).

[18] J. Ross and D. Rogerson, "Xb-70 technology advancements," in *Aircraft Prototype and Technology Demonstrator Symposium*, p. 1048, 1983.

[19] R. T. Whitcomb, "A design approach and selected wind tunnel results at high subsonic speeds for wing-tip mounted winglets," Tech. Rep. NASA-TN-D-8260, National Aeronautics and Space Administration, 1976.

[20] J. G. Verstraeten and R. Slingerland, "Drag characteristics for optimally span-loaded planar, wingletted, and c wings," *Journal of aircraft*, vol. 46, no. 3, pp. 962–971, 2009.

[21] S. Khosravi and D. W. Zingg, "Aerostructural perspective on winglets," *Journal of Aircraft*, vol. 54, no. 3, pp. 1121–1138, 2017.

[22] K. Asai, "Theoretical considerations in the aerodynamic effectiveness of winglets," *Journal of Aircraft*, vol. 22, no. 7, pp. 635–637, 1985.

[23] A. Elham and M. J. van Tooren, "Winglet multi-objective shape optimization," *Aerospace Science and Technology*, vol. 37, pp. 93–109, 2014.

[24] B. Obradovic and K. Subbarao, "Modeling of dynamic loading of morphing-wing aircraft," *Journal of Aircraft*, vol. 48, no. 2, pp. 424–435, 2011.

[25] J. Bowman, G. Reich, B. Sanders, and G. Frank, "Simulation tool for analyzing complex shape-changing mechanisms in aircraft," in *AIAA Modeling and Simulation Technologies Conference and Exhibit*, 2006.

[26] C. S. Beaverstock, J. Fincham, M. I. Friswell, R. M. Ajaj, R. De Breuker, and N. Werter, "Effect of symmetric & asymmetric span morphing on flight dynamics," in *AIAA Atmospheric Flight Mechanics Conference*, 2014.

[27] D. Grant and R. Lind, "Effects of time-varying inertias on flight dynamics of an asymmetric variable-sweep morphing aircraft," in *AIAA Atmospheric Flight Mechanics Conference and Exhibit*, 2007.

[28] P. Bourdin, A. Gatto, and M. Friswell, "Aircraft control via variable cant-angle winglets," *Journal of Aircraft*, vol. 45, no. 2, pp. 414–423, 2008.

[29] A. Taylor, "DC-10 winglet flight evaluation: Summary report," Tech. Rep. NASA-CR-3748, National Aeronautics and Space Administration, 1983.

[30] C. A. Shollenberger, J. W. Humphreys, F. S. Heiberger, and R. M. Pearson, "Results of winglet development studies for DC-10 derivatives," Tech. Rep. NASA-CR-3677, National Aeronautics and Space Administration, 1983.

[31] G. E. Temanson, "KC-135 winglet program review: Measuraments of the fuel mileage of a KC-135 aircraft with and without winglets," Tech. Rep. NASA-CP-2211, National Aeronautics and Space Administration, September 1981.

[32] M. W. Kehoe, "KC-135 winglet program review: KC-135 winglet flight flutter program," Tech. Rep. NASA-CP-2211, National Aeronautics and Space Administration, September 1981.

[33] M. P. Snyder, B. Sanders, F. E. Eastep, and G. J. Frank, "Vibration and flutter characteristics of a folding wing," *Journal of Aircraft*, vol. 46, no. 3, pp. 791–799, 2009.

[34] M. P. Snyder and T. A. Weisshaar, "Flutter and directional stability of aircraft with wing-tip fins: Conflicts and compromises," *Journal of Aircraft*, vol. 50, no. 2, pp. 615–625, 2013.

[35] I. Wang and E. H. Dowell, "Structural dynamics model of multisegmented folding wings: theory and experiment," *Journal of Aircraft*, vol. 48, no. 6, pp. 2149–2160, 2011.

[36] I. Wang, S. C. Gibbs IV, and E. Dowell, "Aeroelastic analysis of a folding wing: Comparison of simple and higher fidelity models for a wide range of fold angles," in *54th AIAA/ASME/ASCE/AHS/ASC Structures, Structural Dynamics, and Materials Conference*, p. 1635, 2013.

[37] C. L. Ruhlin, F. Rauch, and C. Waters, "Transonic flutter model study of a supercritical wing and winglet," *Journal of aircraft*, vol. 20, no. 8, pp. 711–716, 1983.

[38] C. L. Ruhlin, K. G. Bhatia, and K. Nagaraja, "Effects of winglet on transonic flutter characteristics of a cantilevered twin-engine-transport wing model," 1986.

[39] D. Tang and E. H. Dowell, "Theoretical and experimental aeroelastic study for folding wing structures," *Journal of Aircraft*, vol. 45, no. 4, pp. 1136–1147, 2008.

[40] J. G. Barmby, H. J. Cunningham, and I. Garrick, "Study of effects of sweep on the flutter of cantilever wings," Tech. Rep. NACA - 1014, National Advisory Committee for Aeronautics, 1951.

[41] S. G. Kelly, *Fundamentals of Mechanical Vibrations*. McGraw Hill, Year, 2 ed., 2000.

[42] F. Georgiades, J. Warminski, and M. P. Cartmell, "Towards linear modal analysis for an l-shaped beam: Equations of motion," *Mechanics Research Communications*, vol. 47, pp. 50–60, 2013.

[43] W. L. Shelton Jr, "Flutter prediction in forward-swept wings by assumed modes and strip theory.," tech. rep., Air Froce Institute of Technology, Wright-Patterson Air Force Base, OH School of Engineering, 1982.

[44] J. D. Anderson Jr, *Fundamentals of aerodynamics*. McGraw-Hill Education, 2010.

[45] P. C. Wheeler, "An explication of airfoil section bending-torsion flutter," Master's thesis, University of Maryland, College Park, Maryland, United States, 2004.

[46] S. L. Brunton and C. W. Rowley, "Empirical state-space representations for theodorsen's lift model," *Journal of Fluids and Structures*, vol. 38, pp. 174–186, 2013.

[47] N. S. Nise, *Control Systems Engineerging*. John Wiley & Sons, 6 ed., 2010.

[48] A. Balasubramnian, "Plate analaysis with different geometries and arbitrary boundary conditions," Master's thesis, The University of Texas at Arlington, Texas, United States, 2011.

[49] R. A. Rajapakse, *Pile design and construction rules of thumb*. Butterworth-Heinemann, 2016.

[50] L. Meirovitch, *Fundamentals of vibrations*. Waveland Press Inc, IL, 2001.

[51] S. S. Rao, *The finite element method in engineering*. Butterworth-heinemann, 2017.

[52] The Editors of Encyclopaedia Britannica, "Reference frame." Available at `https://www.britannica.com/science/reference-frame`, April 2016 (accessed September 25, 2019).

[53] N. J. Kasdin and D. A. Paley, *Engineering dynamics: a comprehensive introduction*. Princeton University Press, 2011.

[54] H. D. Young, R. A. Freedman, and L. Ford, *University Physics*. Pearson education, 12 ed., 2006.

[55] R. L. Bisplinghoff, J. W. Mar, and T. H. Pian, *Statics of deformable solids*. Courier Corporation, 2014.

[56] S. Liska and E. H. Dowell, "Continuum aeroelastic model for a folding-wing configuration," *AIAA Journal*, vol. 47, no. 10, pp. 2350–2358, 2009.

[57] J. L. Salmon, J. E. Bluman, and C.-K. Kang, "Quasi-steady versus navier-stokes solutions of flapping wing aerodynamics," in *55th AIAA Aerospace Sciences Meeting*, 2017.

[58] L. Meirovitch, *Elements of vibration analysis*. McGraw-Hill Science, Engineering & Mathematics, 1975.

[59] R. R. Craig and A. J. Kurdila, *Fundamentals of structural dynamics*. John Wiley & Sons, 2 ed., 2006.

[60] W. Hallauer Jr and R. Liu, "Beam bending-torsion dynamic stiffness method for calculation of exact vibration modes," *Journal of Sound and Vibration*, vol. 85, no. 1, pp. 105–113, 1982.